INTERPHASE AND PARTICLE DISPERSION CORRELATIONS IN POLYMER NANOCOMPOSITES

by

Erkan Senses

A DISSERTATION

Submitted to the Faculty of the Stevens Institute of Technology
in partial fulfillment of the requirements of the degree of

DOCTOR OF PHILOSOPHY

_____
Erkan Senses, Candidate

ADVISORY COMMITTEE

_____
Dr. Pinar Akcora, Chairman Date

_____
Dr. Svetlana Sukhishvili Date

_____
Dr. Matthew Libera Date

_____
Dr. Henry Du Date

STEVENS INSTITUTE OF TECHNOLOGY
Castle Point on Hudson
Hoboken, NJ 07030

INTERPHASE AND PARTICLE DISPERSION CORRELATIONS IN POLYMER NANOCOMPOSITES

Abstract

Particle dispersion in polymer matrices is a major parameter governing the mechanical performance of polymer nanocomposites. Controlling particle dispersion and understanding aging of composites under large shear and temperature variations determine the processing conditions and lifetime of composites which are very important for diverse applications in biomedicine, highly reinforced materials and more importantly for the polymer composites with adaptive mechanical responses. This thesis investigates the role of interphase layers between particles and polymer matrices in two bulk systems where particle dispersion is altered upon deformation in repulsive composites, and good-dispersion of particles is retained after multiple oscillatory shearing and aging cycles in attractive composites. We demonstrate that chain desorption and re-adsorption processes in attractive composites under shear can effectively enhance the bulk microscopic mechanical properties, and long chains of adsorbed layers lead to a denser entangled interphase layer. We further designed experiments where particles are physically adsorbed with bimodal lengths of homopolymer chains to underpin the entanglement effect in interphases. Bimodal adsorbed chains are shown to improve the interfacial strength and used to modulate the elastic properties of composites without changing the particle loading, dispersion state or polymer conformation. Finally, the role of dynamic asymmetry (different mobilities in polymer blends) and chemical heterogeneity in the

interphase layer are explored in systems of poly(methyl methacrylate) adsorbed silica nanoparticles dispersed in poly(ethylene oxide) matrix. Such nanocomposites are shown to exhibit unique thermal-stiffening behavior at temperatures above glass transitions of both polymers. These interesting findings suggest that the mobility of the surface-bound polymer is essential for reinforcement in polymer nanocomposites, contrary to existing glassy layer theories for polymers on attractive particle surfaces. The shown thermally-induced stiffening behavior is reversible and makes this interfacial mechanism highly attractive in developing new active, remotely controllable engineered materials from non-responsive components.

Author: Erkan Senses

Advisor: Dr. Pinar Akcora

Date: May 4, 2015

Department: Chemical Engineering and Materials Science

Degree: Doctor of Philosophy

Acknowledgements

This work would not have been possible without help from many great people.

First and foremost, I would like to express my deepest gratitude to my thesis advisor, Professor Pinar Akcora, for all the effort and time she put on me, her encouragement, advice and financial support during my Ph.D. work. I appreciate the freedom she gave to me to explore my own and learn from mistakes while being always available to give suggestions whenever I needed. Her enthusiasm and ambition towards research has been a great source of motivation throughout my study.

I would also like to thank my committee members, Professors Svetlana Sukhishvili, Matthew Libera and Henry Du, for their time and valuable feedback on my work. I am thankful to Prof. Libera for his constructive criticism which helped me to expand my view and see a bigger picture. I am also thankful to Prof. Du for being always positive and encouraging from the very first week of my PhD years at Stevens. I am indebted to Prof. Sukhishvili for very helpful discussions during our collaborative work and for being always optimistic.

I would like to thank my current and past colleagues in Soft Materials Lab: Kristen, Dr. Jiao, Haoyu, Siqi and Chongfeng. Dr. Yang Jiao and I started our PhD at Stevens in the same year. She was the person who I shared the lab and office most and I appreciate her knowledge, collaboration and support. I also had chance to work with and mentor masters

and undergraduate students on this journey. Thank you to Dali, Matt, Desi, Andrew, Tom, and Armen; your help is much appreciated.

Thanks to all faculty, students and staff of Chemical Engineering and Materials Science Department for making our workplace enjoyable. Special thanks to Nancy Webb, Frances Flanigan and Gabriela Guzman for their help in administrative work and their patience. I am very grateful to Prof. Bernard Gallois for giving me the opportunity to participate in teaching thermodynamics and being a great teaching mentor. Thanks to Prof. Dilhan Kalyon for teaching transport and rheology that greatly helped me to understand the concepts and again thanks to his group for DSC and TGA. I appreciate Alex Chou's willingness to help and training for electron microscopy in LMSI. I also acknowledge Prof. Sukhishvili's Lab for DLS and contact angle measurements.

I thank Dr. Lixia Rong for helping me with SAXS experiments, performed at the National Synchrotron Light Source (NSLS), Brookhaven National Laboratory. I also thank Dr. Changwoo Do's help for SANS experiments at the Oak-Ridge National Laboratory. I appreciate Dr. Suresh Narayanan's help for the XPCS experiments in Advanced Photon Source of Argonne National Laboratory. I also thank to Dr. Antonio Faraone help for NSE experiments. I gratefully acknowledge financial support from NSF-DMR CAREER grant (#1048865), Stevens's start-up funds and ACS Petroleum Research Funds.

Finally, I would like to thank my parents, sisters, grandparents and each member of my extended family for their unconditional love, encouragement and support. I am especially

grateful to my grandparents for their constant faith in my success. And above all, I am grateful to my mom who made the greatest sacrifice by letting me pursue my career in the Americas!

Thank you all!

Erkan Senses

April 24, 2015

Dedication

To my parents and grandparents…

Table of Contents

List of Tables

List of Figures

List of Symbols

A	Speckle contrast
α	Chain expansion ratio
β	Stretching exponent
d	Particle diameter
$\not{D}$	Dispersity
D_{rep}	Reptation time
E	Stored elastic energy
e_n	Coefficient of the n^{th} basis of Chebyshev polymonials of the 1^{st} kind
g_2	Intensity-intensity auto-correlation function
G'_n	n^{th} harmonic elastic modulus
G_{Ne}	Plateau modulus of an entangled polymer
G'_L	Elastic modulus at large strain
Gr	Greasley number

$G_S^{'}\,(G_M^{'})$	Elastic modulus in the zero-strain limit
γ	Strain
γ_o	Strain amplitude
h	Hydrodynamic size
$I\,(q)$	Intensity of scattering
I_n	Amplitude of the n^{th} order harmonics in Fourier Transform
k	Boltzmann constant
m	Dynamic fragility index
M_n	Number-average molecular weight
M_w	Weight-average molecular weight
M_e	Entanglement molecular weight
N	Number of repeating unit in a chain
N_A	Avogadro constant
N_e	Number of repeating unit between two entanglement sites

N_L	Number of repeating unit in a long chain
N_S	Number of repeating unit in a short chain
η^*	Complex viscosity
η_o	Zero-shear viscosity
ϕ_{max}	Maximum packing fraction
ϕ	Fraction by volume
Φ	Volume fraction of one type of chains in a blend
q	Scattering vector
Q	Cooling rate
Q_{std}	Standard cooling rate
ρ	Density
R	Radius of a nanoparticle
R_o	End-to-end distance of a chain

R_g	Radius of gyration
$S(q,t)$	Dynamic structure factor
σ	Stress
T	Temperature
T_g	Glass transition temperature
T_n	n^{th} basis of Chebyshev polymonials of the 1^{st} kind
T_f	Fictive temperature
τ	Relaxation time
τ_{rep}	Reptation time
$\tan\delta$	Loss tangent
x	Diffusion distance
ω	Angular frequency

List of Abbreviations

ATRP	Atom transfer radical polymerization
$CuBr/CuBr_2$	Copper (I) bromide/ Copper (II) Bromide
DSC	Differential Scanning Calorimeter
DLS	Dynamic Light Scattering
d-PMMA	Deuterated poly (methyl methacrylate)
FTIR	Fourier transorm infrared spectroscopy
FTR	Fourier Transform Rheology
h-PMMA	Protonated poly (methyl methacrylate)
ISF	Intermediate scattering factor
LAOS	Large amplitude oscillatory shear
LCST	Lower critical solution temperature
MEK	Methyl ethyl ketone
NMR	Nuclear magnetic resonance
NSE	Neutron spin-echo

PEO	Poly (ethylene oxide)
PMMA	Poly (methyl methacrylate)
PNC	Polymer nanocomposite
PS	Polystyrene
PVAc	Poly(vinyl acetate)
SANS	Small-angle neutron scattering
SAXS	Small-angle X-ray scattering
SEM	Scanning electron microscope
SiO_2	Silica
SLD	Scattering length density
TEM	Transmission electron microscope
TG	Trans-gauche
TGA	Thermogravimetric Analysis
TGA	Thermogravimetric Analysis
THF	Tetrahydrofuran

TsCl	Toluene sulfonyl chloride
TT	Trans-trans
XPCS	X-ray photon correlation spectroscopy

CHAPTER 1

OVERVIEW

Addition of nanoparticles into polymeric matrices improves mechanical[1-4], optical[5], and electrical properties[6,7] of polymer nanocomposites. These properties are essential in diverse applications of implants[8], drug delivery[9], batteries[10] and membranes[11]. Dispersion of nanoparticles is a critical parameter determining performance of nanocomposites, which can be achieved by the competing enthalpic and entropic attractions between particle-particle and particle-polymer. Organization of particles and resultant mechanical properties of nanocomposites are generally investigated in their equilibrium state. This thesis explores the evolution of mechanical behavior of polymer bulk nanocomposites near and out-of- equilibrium states. The hypothesis is that with oscillatory shearing and aging protocols interfacial interactions between particles and polymers can be modulated.

Polymer bulk dynamics in the presence of particles is an interesting topic in polymer physics as our knowledge on the polymer dynamics is limited with the glassy layer theories on attractive surfaces and in thin films. Dynamics of long entangled adsorbed chains on particle interfaces and within nanoparticle-polymer interphases remain still unknown. Attractive interactions between particles and polymers slow down chain mobility and form a thin (~1-4 nm) bound layer around fillers[12,13,14]. Dynamics within the interphase region of polymer matrix and fillers has attracted much attention in recent years because entanglement density and glass-transition temperature may change at high particle loadings due to confinement of chains[15,16,17,18,19,20]. In attractive polymer

nanocomposites with well-dispersed nanoparticles, it is commonly believed that the percolation of this glassy bound layer is responsible for reinforcement in filled elastomers. Contrary to this common hypothesis, recent dynamic measurements showed that the interphase is highly mobile and the confinement of chains near particles can translate into the bulk phase through strong topological interactions (entanglements)[16]. Therefore, interphase has direct consequences on macroscopic bulk properties, which are probed by rheometry.

This thesis aims to understand the role of interphase layers between particles and polymer matrices in two bulk systems. The first system is a repulsive polymer nanocomposite where particle dispersion is altered upon deformation, and the second nanocomposite system is an attractive composite in which good dispersion of particles is retained after multiple oscillatory shearing and aging cycles. Flow-induced tunable interphases result in stiffening behavior of composites which can resist deformation after long time aging. The role of entanglements on the interphase strength is underpinned by using bimodal chains of very short (unentangling) and long (entangling) chains. Furthermore, the effect of dynamic asymmetry and chemical heterogeneity in the interphase region is studied via a miscible polymer blend. Four cases of interphases as schematically illustrated in Figure 1.1 are discussed in the following chapters.

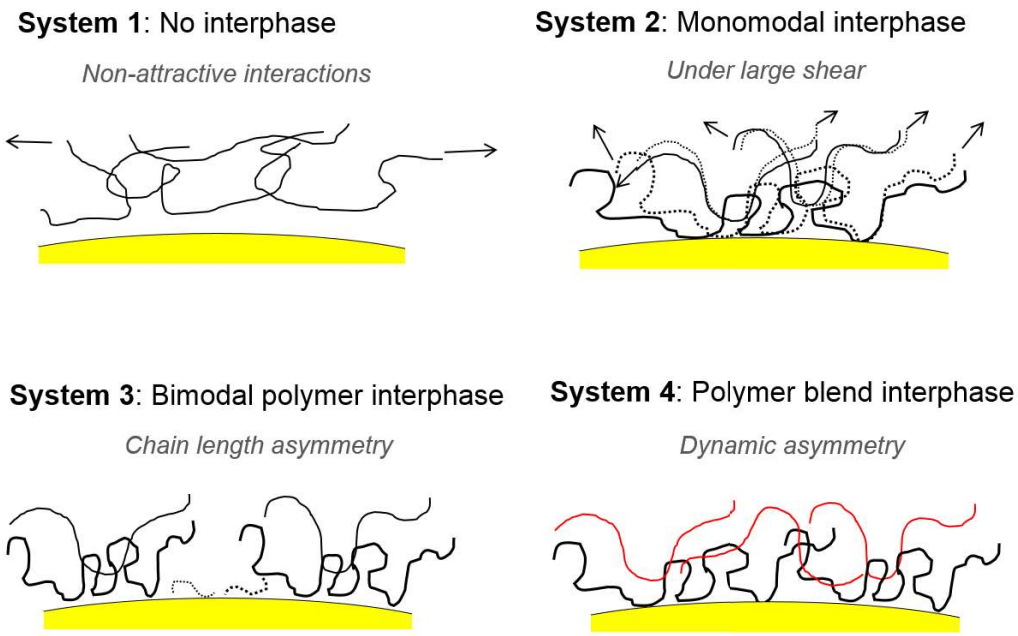

Figure 1. 1. Different interphases of four polymer nanocomposite systems are investigated in this thesis.

In Chapter 2, we report on polystyrene and silica (PS-SiO_2) composite system[21] where hydrophobic polymer and hydrophilic nanoparticles share a repulsive interface; thus polymer adsorption and formation of an interphase is unfavorable. Particles form elongated and connected aggregates at high particle loadings as a result of immiscibility. We focused on the intra-cycle response of PS-SiO_2 nanocomposites to large amplitude oscillatory shearing. We demonstrated, for the first time that, the rapid stress rise at small instantaneous strains is the result of a percolated network, while the large-strain behavior is governed by the non-linear strain-stiffening of entangled polymer chains. Deforming

and resting cycles with varying rest times and transmission electron microscopy (TEM) images unequivocally correlate microstructures to mechanical non-linearities.

Chapter 3 presents an unusual self-stiffening of a model attractive nanocomposite system, poly(methyl methacrylate)-silica (PMMA-SiO_2), under a series of cyclic deformations.[22] We postulate that microscopic relaxation dynamics of polymer is influenced by an interphase region and this effect is suppressed by increasing the particle loading to confine polymer chains. Through a series of well-controlled experiments, we showed that the composites self-stiffen after sufficiently large amplitude shear. Chains desorb from the surface during large shear, entangle denser at rest, resulting in a growing interphase. Small-Angle Neutron Scattering (SANS) and Fourier-Transform Infra-Red (FTIR) spectoscopy experiments provided insights into chain and molecular conformation. Additionally, we showed that stiffening rate is controlled by diffusion of reptating chains at rest.

Entanglement controlled stiffening led to new ideas on how to modulate the strength of interphases. In Chapter 4, we showed that interfacial entanglements can be tuned by simultaneously adsorbing very short and long chains on nanoparticle surfaces.[23] Entanglement density within interphases is controlled by varying volume fraction of long adsorbed chains while keeping particle dispersion state and concentration constant. Results revealed that the strength of interphase and rheological properties can be physically tuned by adsorbing chains of bimodal lengths. Compositional variation of a bound layer leads to dynamic heterogeneities as also measured in dynamic fragility.

Results from Chapter 4 provide a direct evidence for the entanglement driven stiffening mechanism proposed in Chapter 3.

In Chapter 5, we investigated the role of relative mobility between adsorbed and matrix chains to the mechanical behavior. Nanoparticles adsorbed with a high-T_g polymer (PMMA) are dispersed in a miscible low-T_g matrix (poly(ethylene oxide), PEO) to create an interphase consisting of dynamically asymmetric chains. By modulating temperature around the T_g of PMMA, mechanical relaxations of composites are measured as bound polymer becomes glassy and mobile with cooling and heating. Our nanocomposites present an unusual reversible liquid-to-solid transition at temperatures above T_g's of both polymers. Mechanical adaptivity of PEO nanocomposites to temperatures underlies the existence of dynamically asymmetric bound layers on particles, and more importantly their impact on mechanical behavior, which sets these materials apart from conventional polymer composites that soften upon heating. The results suggest that the mobility of the bound polymer is essential for reinforcement contrary to commonly accepted glassy layer hypothesis. Composites with highly asymmetric interphases offer a new route of achieving mechanical adaptivity without cross-linkable or stimuli responsive polymers.

Thermal-stiffening of composites with well-dispersed nanoparticles form an interesting case for particle relaxation as bound polymer vitrifies. In Chapter 6, we present our preliminary results from the X-ray Photon Correlation Spectroscopy (XPCS) for bare SiO_2 and PMMA adsorbed SiO_2 dispersed in PEO matrix. In composites with bare nanoparticles, PEO is adsorbed and bound layer is always mobile at the experimental temperature range. In PMMA adsorbed SiO_2 composite, bound PMMA is

glassy at low temperature and mobile at higher temperatures. We showed that relaxation of bare nanoparticles in PEO is diffusive at various measurement temperatures. To the contrary, dynamics of PMMA adsorbed particles is sub-diffusive in PEO at low temperature with short relaxation times; and the dynamics switches to a diffusive mode with increased relaxation times at high temperature. Particle dynamics probed by the XPCS technique reveal that local viscosity around fillers change with the glassy and mobile PMMA bound layer, which supports the thermo-stiffening behavior presented in Chapter 5. Particle relaxation and rheological measurements of bulk composites show that interphase-governed properties can be modulated without structural changes in bulk systems.

Mechanisms presented here underline the fundamental phenomena of chain dynamics of miscible blends with particles and can be used for designing mechanically adaptive and responsive materials. In Chapter 7, some of the most exciting directions for future work are summarized.

CHAPTER 2

MECHANISTIC MODEL FOR DEFORMATION OF POLYMER NANOCOMPOSITES UNDER LARGE AMPLITUDE SHEAR[1]

Chapter Summary

We report the mechanical response of a model nanocomposite system of polystyrene (PS)-silica to large-amplitude oscillatory shear deformations. Non-linear behavior of PS nanocomposites is discussed with the changes in particle dispersion upon deformation to provide a complete physical picture of their mechanical properties. The elastic stresses for the particle and polymer are resolved by decomposing the total stress into its purely elastic and viscous components for composites at different strain levels within a cycle of deformation. We propose a mechanistic model which captures the deformation of particles and polymer networks at small and large strains, respectively. We show, for the first time, that chain stretching in a polymer nanocomposite obtained in large amplitude oscillatory deformation is in good agreement with the non-linear chain deformation theory of polymeric networks.

---

[1] Reproduced in part with permission from [Senses, E., & Akcora, P. (2013). Mechanistic model for deformation of polymer nanocomposite melts under large amplitude shear. Journal of Polymer Science Part B: Polymer Physics, 51(9), 764-771.] Copyright © 2013 Wiley Periodicals, Inc.

2.1. Introduction

Reinforced composites that are subject to frequent deformation should withstand repeated mechanical loadings and it is desired that their initial structures are retained or recovered. Therefore, it becomes critical to predict the mechanical properties of polymer nanocomposites under large deformation. Structural recovery or reformation after long deformation times adequately determines the potential applications of reinforced materials. The mechanisms for the origin of reinforcement in nanocomposites have been evaluated in terms of the state of particle agglomeration (connected particle network)[24,25] and the strength of particle-polymer interactions[26,27]. The latter effect has been proposed to be due to the immobilization of chains around nanoparticles[28,29] or due to the trapped entanglements[30] as in attractive particle-polymer composites. In the case of polymer bridging between the particles, the polymer conformation has been suggested to be an additional factor to the mechanical behavior in attractive particle-polymer networks where particles and polymer share a wetting interface[31]. Resolving these contributions of particle network, polymer bridging between particles and the percolated glassy layers to the mechanical properties has been challenging. To this end, non-linear viscoelastic properties of composites are pertained intrinsically to the polymer matrix and are shown to enhance with the addition of fillers[25]. Another study of non-linear behavior of filled elastomers shows that elastic moduli do not change with the applied large strain but modifies the lifetimes of glassy bridges[32]. The non-linearity in the elastic stress was explained by the distribution of relaxation times of the percolated glassy layers[32]. Our work focuses on a repulsive composite system where glassy layers do not exist around

the fillers. We aim to explain the origins of non-linear contributions to the elastic stress in terms of particle structures and deformation recovery. In summary, the role of polymer bridging and trapped entanglements between nanoparticles in the reinforcement mechanism is well accepted, however previous mechanical studies are limited to observing the polymer contribution to the overall stress response[25,28,29,32]. Therefore, it is essential that rheological data should be discussed along with the structural changes under shear, but more importantly the elastic term of the stress has to be addressed for the polymer and particle parts to unequivocally distinguish their contributions as the elasticity of polymer chains and stiff materials are well known.

In this work, dynamic response from large-amplitude oscillatory shear (LAOS) experiments is discussed with the changes in particle dispersion to provide a complete physical picture of the mechanical deformation in polymer nanocomposites. LAOS experiments have been applied on microstructural systems in previous works on copolymer solutions and gels. For example, sol-gel transition of PEO-PPO-PEO triblock copolymer solutions is studied in LAOS experiments as they go through microstructural changes[33]. Likewise, the LAOS response of gluten gels was shown to be in agreement with the formation of molecular structures[34]. LAOS has also been a useful method to observe different relaxations of linear and comb polymer melts[35]. Recent improvements on the rheometers (ARES-G2, TA Instruments) for non-linear rheology capabilities as well as mathematical analysis to separate the elastic and viscous component of the total stress allowed us to resolve the non-linearities at large strains[36,37].

We deformed the PS-Si nanocomposites (repulsive system where particles and polymer dislike each other) with large periodic strains and analyzed the elastic stress-strain data to explain the contributions of polymer and particle to the total stress for a wide range of strain. A mechanical model is developed based on a non-linear elastic model for polymeric and particle networks to describe the rich non-linearities. As the structure evolved during the rest time of LAOS, TEM images obtained for different states of deformation and the moduli of the corresponding states allowed us to attribute the mechanical non-linearities to the polymer composite under tension.

2.2. Experimental Section

2.2.1. Composite preparation

Colloidal silica nanoparticles (13±2 nm in size) of Nissan Chemicals were mixed with poly (styrene) (52.5 kg/mol, ~~Đ~~: 1.03) in 1,2 dichlorobenzene to prepare composites containing 2, 7, 15 wt% particle loadings. The solution was first bath-sonicated for 30 min, stirred rigorously for 2 h and then bath-sonicated for another 30 min. The evaporation of the solvent was completed at -38 cm-Hg gauge pressure in approximately 1.5 h and then the oven was set to full vacuum (-76 cm-Hg, gauge) state. The final samples with ~250 μm thickness were annealed at 130 ^{o}C for 4 days, at 150 ^{o}C for 3 days and finally at 180 ^{o}C for 2 h under vacuum.

2.2.2. Structural Characterization

Nanocomposite bulk films were microtomed at room temperature and dispersion of nanoparticles was examined in transmission electron microscope (Philips CM20 FEG TEM/STEM) operated at 200 keV.

2.2.3. Rheology

Rheology measurements were performed on a strain-controlled ARES-G2 rheometer (TA Instruments) equipped with 8-mm diameter parallel plates geometry under nitrogen. The samples annealed according to above procedure were molded with a vacuum assisted compression molder at 150 ^{o}C for 10 min. The samples were finally annealed at 130 ^{o}C for 12 h. The measurements were performed at 170 ^{o}C following sample equilibration time of 10 min. Time sweep experiments during this period confirmed the sample stability. The large amplitude oscillatory shear (LAOS) tests were performed at a fixed angular frequency of 1 rad/s. The time dependence of the modulus was determined by fixing the strain amplitude at 500% and allowing the samples rested for increasing periods of waiting times (5-2000 sec) between 20 cycles of large deformation. Data were collected at a sampling frequency of 300 Hz, giving 1885 points per cycle. After completing each test, the samples were cooled below T_g in one minute. The gap was adjusted so that the normal force never exceeds +/- 1N. This prevented deformation of the sample during the cooling step.

2.3. Results and Discussion

Particle dispersion in all composites prior to rheology measurements was characterized in TEM. Figure 2.1 shows that nanocomposite at 2 wt% loading present string-like structures and further increase of the concentration to 7 and 15wt% results in percolated aggregates. The polymer and nanoparticles share a repulsive interphase; resulting a diffusion-limited nanoparticle aggregates commonly observed for this system

[38]. The branching aggregates; however, well distributed in the polymer, thus allows comparison of different particle loadings.

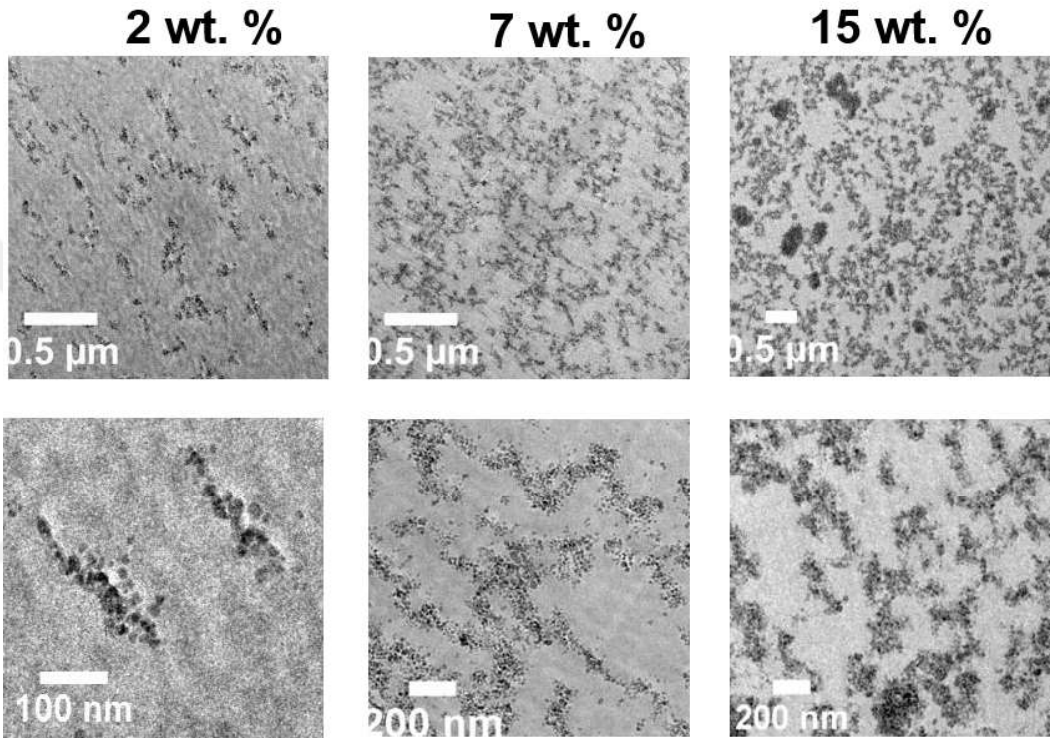

Figure 2. 1. Cartoons presenting components and the TEM images of the resulting PS composites containing 2, 7 and 15 wt% nanoparticles at different magnifications.faigo

We conducted linear viscoelastic measurements on PS homopolymer to estimate the reptation time (τ_{rep}) and diffusion coefficient (D_{rep}) of PS chains. The frequency sweep data obtained at 170 ^{o}C is shown in Figure 2.2a.The entanglement (plateau) modulus (G_{Ne}) is ~200 kPa at this temperature. The zero shear viscosity (η) is determined to be ~4000 Pa.s from the low frequency plateau of the complex viscosity (η^{*}) as shown in Figure 2.2b. The reptation time is related to G_{Ne} and η with the relationship $\eta = (\pi^2/12)$

$\tau_{rep} G_{Ne}$. Thus, τ_{rep} is calculated to be ~0.02 sec at 170 ^{o}C. The storage moduli and loss angle in the linear viscoelastic region for homopolymer and composites at 170 ^{0}C is shown in Figure A1.2.

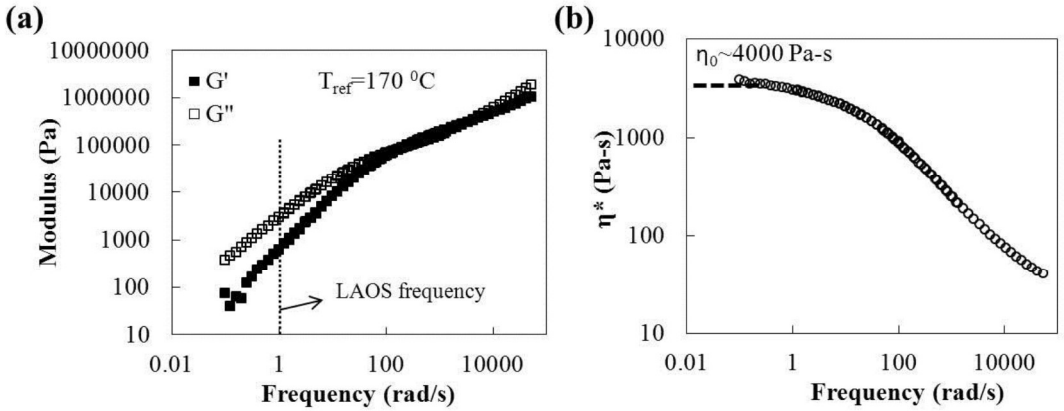

Figure 2. 2. Linear viscoelastic properties of the PS homopolymer. **(a)** Time-temperature superposition of the storage and loss moduli for PS with reference temperature of 170 ^{o}C. Vertical line represents the frequency used in this study. **(b)** Complex viscosity as a function of frequency.

We strained the samples periodically in the non-linear region and observed the resulting mechanical response. When a periodic strain, $\gamma(t)=\gamma_0 \sin(\omega t)$, is imposed to a sample with angular frequency, ω, and strain amplitude, γ_0, the sample is strained in the forward direction from zero to the maximum strain (γ_0) in a quarter of the oscillation period, $\pi/2\omega$. In the following quarter cycle the strain is decreased to zero. This motion is then repeated in the same manner but in the opposite direction and the cycle is completed at one oscillation period. Thus, choosing the strain amplitude greater than the linear

viscoelastic limit, each deformation cycle allows transition of sample from small strain (linear) to large strain (non-linear) response.

As the samples are sheared at large-strain amplitudes, the energy stored by the stiff particle network is overcome by the external work imposed by the deformation and the chains stretching back and forth during periodic loadings may contribute to the rupture of the network. This continuous deformation is responsible for initial cycle-to-cycle strain softening (see Figure A1.1) which is not observed for homopolymer. Thus, the initial few cycles contain particle structural information from the previous state and we analyzed our data from the averaged stress-strain response from the initial first four cycles (see Appendix 1 and Figure A1.1). We applied 20 cycles of sinusoidal strains $\gamma(t)=\gamma_0\sin(\omega t)$, with $\gamma_0=5$ at a fixed frequency of $\omega=1$ rad/s, which was necessary to reach steady stress response for any composition. The frequency was chosen to be 1 rad/s because the polymer's loss (viscous) modulus is higher than the storage (elastic) modulus at that frequency and temperature (see Figure 2.2a), which facilitates shearing without giving rise to instabilities such as edge fracture, wall-slip or crazing (see Appendix 1). While the viscous component is higher than the elastic component at these conditions, the decomposition[32,36,39] of the total stress allows us to separate the elastic component as a function of resting time and concentration (see Appendix 1 for non-linear deformation analysis). Because the deformation of stiff particle network and flexible polymer chains can contribute at different strain levels, it is important to choose strain amplitude high enough to observe both contributions in a cycle of deformation. Figure 2.3 shows the

elastic stress-strain behavior of the homopolymer and 15 wt% loading at different strain amplitudes.

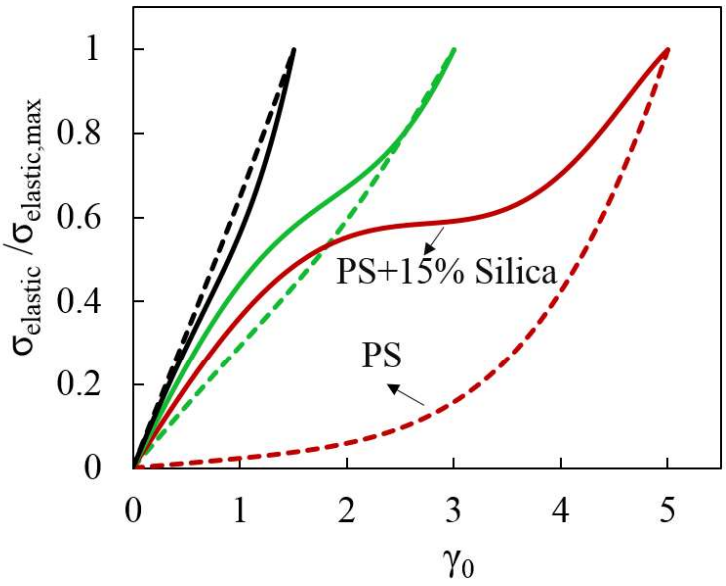

Figure 2.3. Normalized stress-strain curves of homopolymer (dashed lines) and nanocomposite with 15 wt.% compositions (solid lines) at 150% (black curves), 300% (green curves) and 500% (red curves) strain amplitudes. The measurements are done at 170 ^{o}C and 1 rad/sec.

The homopolymer behaves linearly at 150% while strain hardening is observed at the largest strains when the strain amplitude is chosen to be 300% or 500%. The composite, on the other hand, shows non-linear strain softening at intermediate strains, which gets wider and exhibits clear yield-like behavior at 500% strain amplitude. The deformation pattern at this strain amplitude reveals three different regions for the

nanocomposite as a function of strain; while homopolymer only gets harden at large strains without showing a yielding behavior. Thus, the strain amplitude of 5 was large enough to observe the evolution of these different deformation regimes which will be discussed in the following section.

The elastic stress-strain behavior of the homopolymer and composites are presented in Figure 2.4a. In order to compare composites with different particle loadings, we normalized the stress values with their corresponding maximum stress (σ_{max}). The results suggest that the stress response can be divided into three regions: At small strains (region i), the elastic stress rises linearly and the slope of the curves monotonically increases with particle concentration. This region is followed by yield-like behavior for composite samples while homopolymer's stress keeps increasing. The yield strain, which we calculated from the maximum curvature on the stress-strain curve following the linear elastic region[40] (i.e. $|d^2\sigma/d\gamma^2|$=max), was determined to be 1.60 and nearly the same for each concentration. The yield stresses (Figure 2.4a) of the composites show similar linear trend with the maximum stress attained in a cycle. At 15 wt% loading, highly percolated structures (see Figure 2.1) create higher energy barrier for flow to occur. The elastic energy that is stored by means of particle network increases with the particle concentration, reaches to a plateau and the sample yields due to network breaking. The yielding persists over a wide range of strain since the stronger junctions require more energy to break. The specific elastic energy (energy per unit volume) to break the particle network can be estimated by $E = 1/2\ (\sigma_{yield}\ .\gamma_{yield})$, which is the area under the stress-strain curves in the region (i). It is seen that the elastic energy increases with particle

loading at constant yield strain. Since the aggregates at different concentrations have similar fractal-like nature, the strength of particle networks increases with the particle concentration which in turn gives rise to linear dependence of the yield stress while the yield strain becomes unchanged. The breaking of the network continues at strains between 1.6 and 3.6, where both the particles and polymer contribute to the deformation in this regime. As the strain goes beyond 3.6 the polymer gets more stiffen probably due to finite extensibility of the polymer chains[41]. The slope of the curve in this region does not significantly change with particle concentration, therefore deformation at this strain may be attributed to the chain extension. The schematic representation of the three regions is shown in Figure 2.4b. The area under the normalized stress-strain curve and maximum stress determines the total elastic stress stored per volume in a quarter cycle. Thus, the particle-network both increases the strength and stored elastic energy.

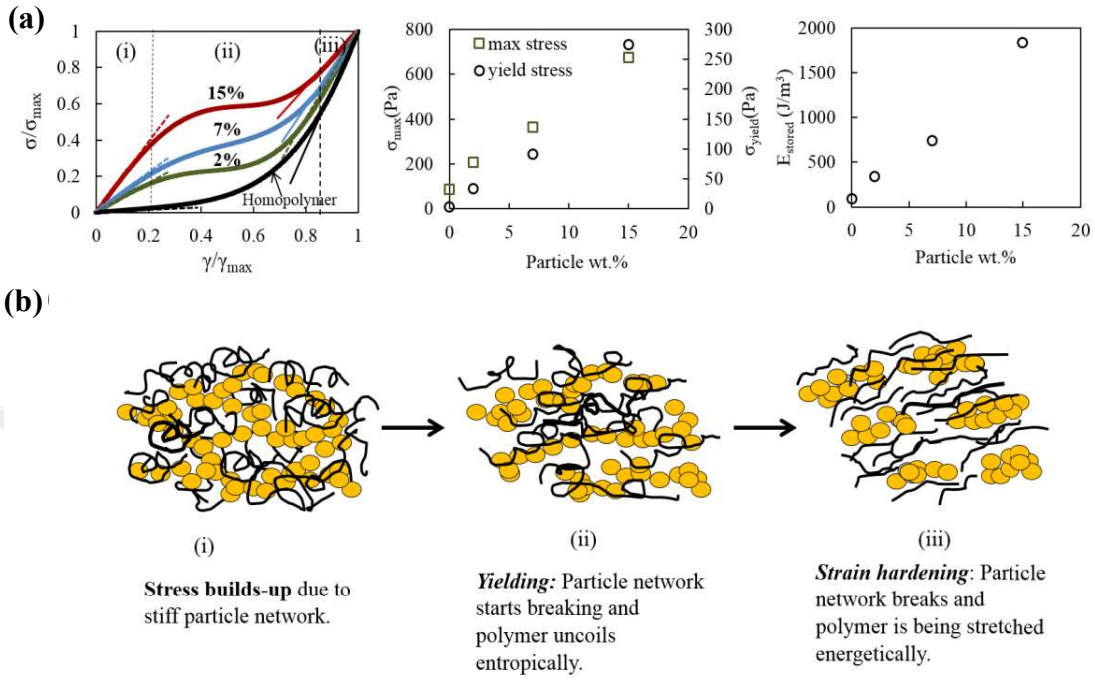

Figure 2. 4. (a) Normalized stress-strain behavior of homopolymer, 2, 7 and 15 wt% nanocomposites shows the behavior of the samples at small strain; yielding and strain hardening at large strains. Maximum stress (at γ=5), yield stress and stored elastic energy are shown as a function of particle concentration. **(b)** Schematic representation of deformation stages of a repulsive nanocomposite having weak interactions between polymer and fillers.

Because particles and polymer govern the deformation at small and large strain levels, respectively, we developed a non-linear deformation model that explains the elastic stress-strain behavior at a wide range of strain. Figure 2.5a presents the mechanical analog of the model which consists of a non-linear elastic spring ($\sigma=G_{part}\gamma^n$) with strain softening parameter, n, that is attached to a friction element (with critical

stress and strain, σ_y, γ_y) in parallel with a Gaussian coil. At strains smaller than the critical strain, only the elastic spring responses to deformation and gives rise to the initial stress build-up. Beyond the critical strain, the friction element starts moving with a constant stress σ_y, while the Gaussian coil is stretched. At large deformation (above 3.6 strain) the polymer coil is highly stretched, the chain presumably deviates from Gaussian statistics and final hardening is observed. Elasticity of a single polymer chain in biological systems and gels and polymeric networks has been well studied both theoretically and experimentally[41,42,43]; however, stretching of polymer chains in melt has not been directly captured from rheology experiments due to the presence of viscous contributions to the measured stress. Since we separated the elastic component of the stress at high strains, the non-linear shear deformation theory for polymer networks[44] may apply in our case and the stress response of polymer coil can be expressed as: $\sigma = \frac{G_p \gamma}{3}\left[1+2\left(1-\frac{\beta I_1(\gamma)}{3}\right)^{-2}\right]$, where G_{pol} is the shear modulus of the polymer, $I_1(\gamma)=(\gamma^2+3)$ is the first invariant for shear deformation and β is the chain elongation ratio and defined as the ratio of mean square of the end-to-end distance of an unperturbed chain to the square of end-to-end distance of the fully extended chain[44] ($\beta = \langle R_0^2 \rangle / R_{max}^2$). The overall stress functions can be expressed at different strain limits as:

$$\sigma = \begin{cases} G_{part}\gamma^n, & 0 \le \gamma < \gamma_y \\ \frac{G_{pol}(\gamma-\gamma_y)}{3}\left[1+2(1-\frac{\beta I_1(\gamma-\gamma_y)}{3})^{-2}\right]+C, & \gamma_y \le \gamma \le \gamma_0 \end{cases}$$

Constant C is used to ensure the continuity of the stress at the yield point and is equal to the constant yield stress generated by the friction element ($C = \sigma_y = G_{part}\gamma_y^n$). Elastic stress-strain curves for homopolymer and composites and the corresponding model fits are shown in Figures 2.5b and 2.5c. Note that for homopolymer, the particle contribution does not exist. We used γ_y=1.6 for all the compositions as determined from the curvature of the stress-strain data. The strain softening parameter (n) is found to be 0.84 ± 0.035, nearly constant for all the composites. Stiffness of the polymer chains (G_{pol}) is found to be increasing with particle concentration and reaches a plateau after 7% loading. In addition, extension ratio (β) of homopolymer increases from 0.06 to 0.1 with the addition of fillers, which is in agreement with the reported values of polymer networks[44]. Increase in β suggests that chains in composites are less stretched than homopolymer. Although the slopes are discontinuous at the critical strain, this model properly relates the macroscopic behavior to the microscopic theoretical models. Similar models exist in the literature to describe non-linear elastic behavior of the flexible gels and biological networks[44,45,46,47]. For example, the spider silk presents very similar non-linear elastic behavior in which nodes act as sacrificial elements and material presents yield-like behavior after initial linear increase. The silk presents stiffening at the largest strains due to finite extensibility of the initially coil-like polymers. The atomistically derived non-linear model was utilized where stiffening behavior is captured with a simple exponential function. The model presented here is based on well-known non-linear deformation theory of polymer chains and networks[44,48] and it is demonstrated here for the first time that the LAOS experiments can capture the single chain deformation.

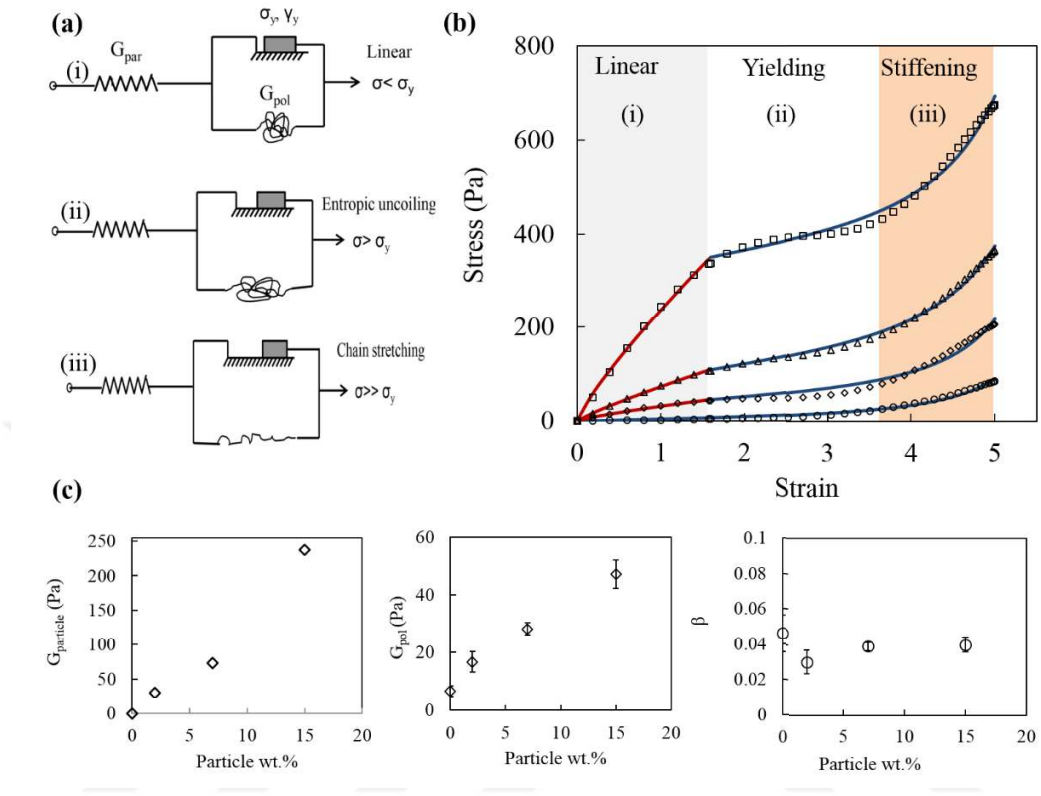

Figure 2.5. (a) Mechanical model for the elastic stress strain curves for different compositions. A power law spring ($\sigma = G_{part}\gamma^n$) with strain softening parameter, n, is combined with a friction element in parallel (with critical stress and strain, σ_y, γ_y) and a Gaussian coil. At strains smaller than the critical strain, only the elastic spring responses. Beyond the critical strain, the friction element freely moves with a constant stress σ_y while the Gaussian coil is stretched. **(b)** The elastic stress-strain curves for homopolymer and composites with model fits. **(c)** The fitting parameters, G_{part}, G_{pol} and β as a function of particle loading.

In order to further elucidate the particle and polymer contributions to the elastic stress, we designed the experimental protocol as schematically shown in Figure 2.6a. We

applied 20 cycles of deformation with the same parameters ($\gamma_0 = 5, \omega = 1$ rad/sec) in each deformation step. Between those steps, the samples are allowed to rest for certain times, increasing from 5 to 2000 seconds. The samples are rested for time periods larger than the relaxation time of polymer (~0.02 sec). This allows relating the change in mechanical behavior to the particle structural evolution but not to the polymer's relaxation during rest time. The stress-strain response from the initial few cycles of each deformation step thus represents the behavior of the structure attained in the preceding rest time. Figure 2.6b shows the stress-strain behavior of homopolymer and composites at initial, after 10 sec and 2000 sec resting. The yield behavior at the initial stage disappears in the intermediate stage (10 sec) and reappears after resting 2000 sec while the behavior of homopolymer presents the same non-linear behavior at any stage. With measurements following 10 sec resting time (shown in red marks in Figure 2.6b and labeled as "deformed"), we probe the mechanical properties of the deformed structures since structures cannot evolve in 10 sec. Note that the particle diffusion distance, $x \sim (Dt)^{0.5}$ is calculated as ~1 nm in 10 sec (with D~8 nm^2/sec, in Appendix 1). It is interesting to note that the stress data collected on deformed composites after 10 sec waiting do not yield as in homopolymer. After measuring the stress response on samples deformed and aged at different times, next we look into the structures in TEM. Figure 2.7b shows strong segregation of particles from the deformed polymer and waited for 10 sec. This allows us to conclude that yielding, which is a result of particles restructuring, appears at small strains. After waiting 2000 sec following the deformation cycle, stress reaches to the initial stress values of composites, which is also depicted in TEM images. SAXS patterns corresponding to

these different states of deformation also confirm that the structure is mostly recovered after long time resting. Particle structure at the deformed state is rather different and anisotropic due to possible shear induced ordered structures form in addition to large segregated regions.

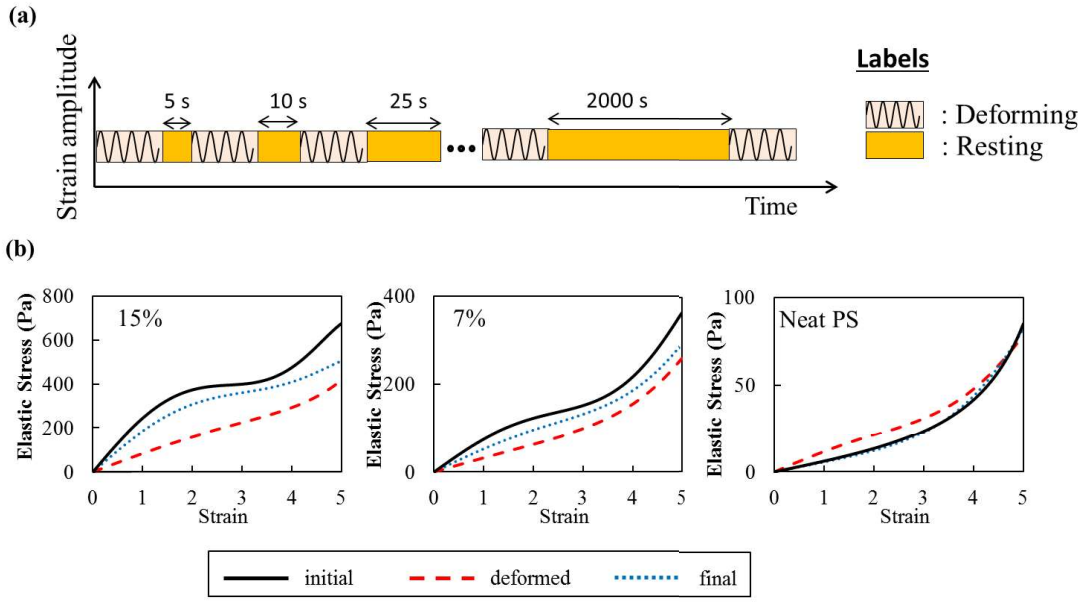

Figure 2. 6. (a) Schematic representation of the experimental timeline: 20 cycles of large periodic deformations with strain amplitude of 500% and frequency of 1 rad/sec in each deformation step. Samples were allowed to rest at certain time periods (5, 10, 25, 50, 100, 300, 900 and 2000 sec) between each deformation steps. **(b)** Stress-strain curves for homopolymer, 7 and 15 wt% compositions at different rest times: deformed (after 10 sec waiting), final (after 2000 sec waiting).

We then calculated the moduli at small (<1.6) and large (>3.6) strains and compared their evolution as a function of resting time in Figure 2.7a. It is seen that the

large strain modulus ($\sigma(\gamma_0)/\gamma_0$) has a weak dependence on waiting time as it is mainly controlled by matrix polymer. However, modulus at small strain, $\lim_{\gamma\to 0}(d\sigma/d\gamma)$, decreases after short waiting times particularly for 15% composite and gets close to the initial value with aging at longer times. This behavior is in-line with the particle structuring at different waiting times as discussed in previous section. At longer resting times, large clusters break leading to an increase in small-strain modulus and yielding reemerges. Here, we comment on the size of our particles and polymer tube length. Our particles of 13 nm in size are larger than the tube length of 52 kDa PS (~ 8.5 nm). In a previous work, Rubinstein[49] suggested that at times longer than the relaxation time of polymer, particles larger than the tube diameter experience ordinary diffusion determined by the bulk viscosity of the melt. In our experiments, the reptation time was 0.02 sec, which is much shorter than the resting times. Thus, particles diffuse during long waiting times of 2000 sec. Since the rest times are longer than the reptation time of polystyrene at any molecular weight, similar aggregation and redispersion of particles remain valid for the same size of particles. 2-D SAXS patterns for composites at different deformation stages are displayed in Figure 2.7b. Particles present some anisotropy in the scattering ring indicating some distortion on the particle aggregation, which is recovered after 2000 sec.

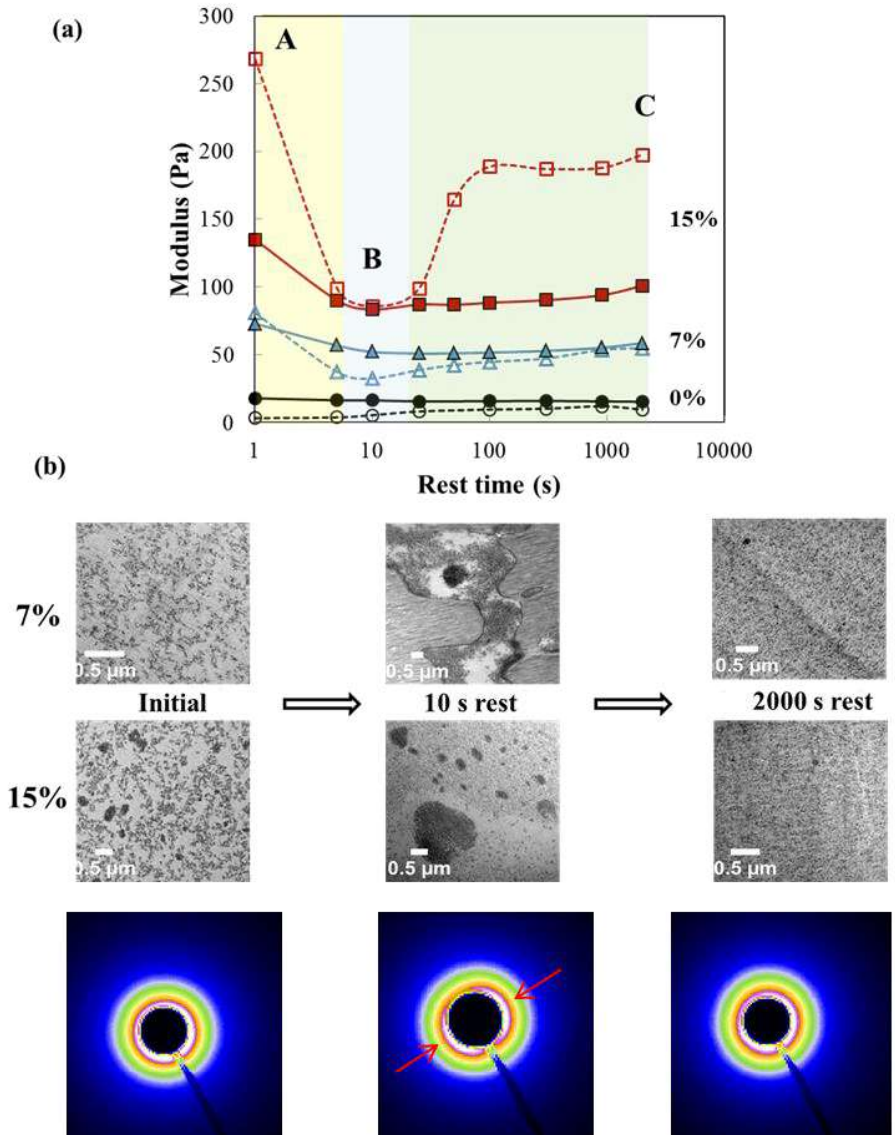

Figure 2. 7. (a) Moduli calculated at small (open symbols) and large (filled symbols) strains as a function of rest time. **(b)** TEM images obtained at initial (A); deformed (10 sec resting) (B); and final (2000 sec resting) (C) stages depict the network breaking and phase segregation in the intermediate stages and following re-dispersion of particles at longer times. 2D SAXS patterns at undeformed, 10 sec and 2000 sec resting states are shown for 7 wt%.

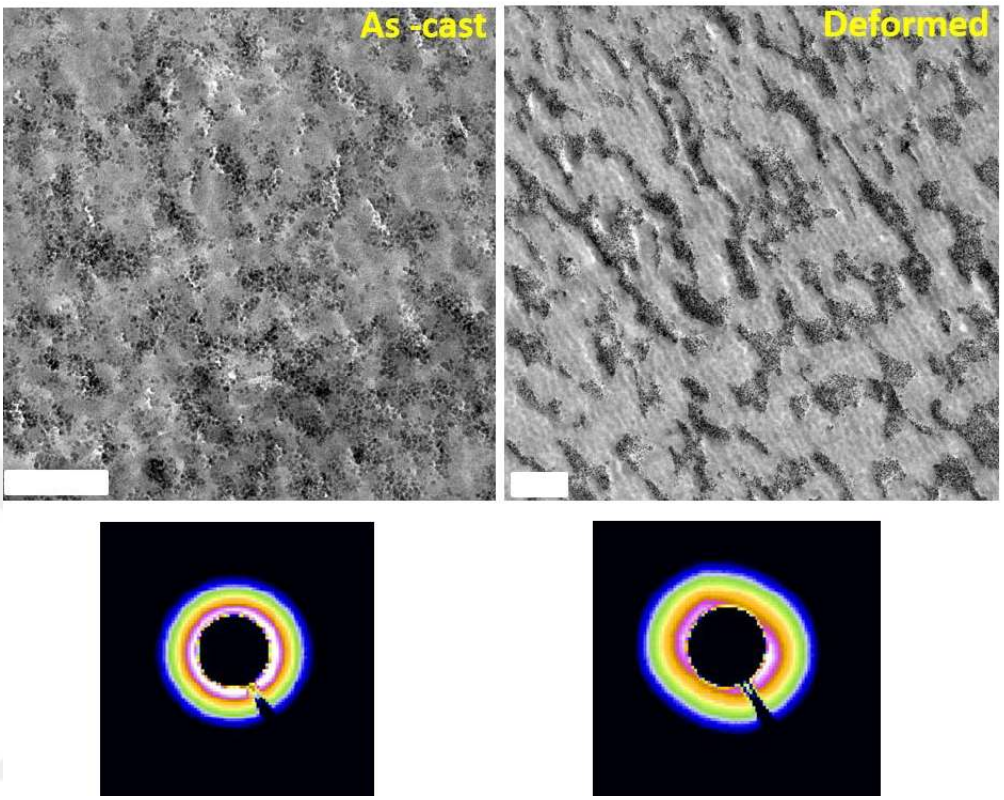

Figure 2. 8. TEM images and corresponding 2D SAXS patterns of 25 wt% sample before and after large deformation showing flow induced anasitropic aligned structure. The scale bars are 500 nm.

The anisotropy is more apparent at larger particle concentrations. We prepared additional composite with 25 wt% particles that clearly shows that aggregates are broken under LAOS and the initial branches of aggregates combine to form well-aligned and uniform structure (Figure 2.8). 2D SAXS detector data present a distorted shape confirming highly anisotropic flow induced structures from bare particles.

2.4. Relationship to Large Amplitude Oscillatory Shear (LAOS) fingerprinting methods: Evolution of higher order harmonics and coefficients of Chebyshev polymonials

Non-linear elastic response of a model repulsive polymer nanocomposite system, PS-SiO_2, is investigated using Fourier Transform Rheology (FTR) methodology[50] and non-linearities are related to inherent material properties to delineate the role of particle agglomeration in this process.

It is shown that polymer nanocomposite with minimal enthalpic interactions between fillers and host matrix presents non-equilibrium states of dispersion under LAOS fields[51]. In standard steady-shear experiments, overshoot in stress with the strain implies common solid-like behavior of the reinforced composites[52,53,54]. However, such measurements only reveal the percolation and structural breakdown of percolated fillers. In LAOS, particle rearrangement influences both viscous and elastic stress components. FTR expresses the total non-linear stress response to sinusoidal excitation as a sum of infinite set of sine and cosine functions with odd integer multiples of the fundamental frequency $\sigma(t,\omega,\gamma_0)=\gamma_0\sum_{n=odd}\left[G_n'\sin(n\omega t)+G_n''\cos(n\omega t)\right]$ with G_n' being the moduli at n^{th} harmonic. The relative intensity of the higher harmonics with respect to fundamental frequency, I_n/I_1, has been used to relate the non-linearities to the materials' properties[55,56,57,58], e.g. an intrinsic property $Q_0=\lim_{\gamma_0\to 0}\left(I_3/I_1{\gamma_0}^2\right)$ has been defined for polymer melts and is shown to be qualitatively sensitive to the chain topology[59]. Cho et al. [60] decomposed the total stress into its elastic σ_e and viscous σ_v components by

using geometric arguments. Ewoldt et al.[61] further utilized the orthonormal decomposition of the elastic and viscous stresses with the Chebyshev polynomials of the first kind as $\sigma_e(\mathrm{x},\omega;\gamma) = \gamma_0 \sum_{n=odd} e_n(\omega,\gamma_0)T_n(x)$ where T_n is the n^{th} order polynomial and e_n is the corresponding elastic coefficient and $x=\gamma/\gamma_0$. First five odd polynomials are plotted within the first quadrant in Figure 2.8. As seen e_1 represents the average stored energy per unit volume within an oscillation cycle and equals to G_1' while e_3 represents the deviations from average response at large strains. The positive e_3 represents strain stiffening and negative e_3 indicates softening within an oscillation cycle. Despite mathematical robustness of both models, physical interpretation of the higher harmonics is still not well understood. While Rogers et al.[62,63] analyzed the non-linear stress response and interpreted the individual harmonics as a sequence of physical processes in colloidal glasses (such as linear stress increase, yielding, flow and reformation), we focus on Chebyshev polynomial analysis. In this section, we aim to relate the rich non-linearities that we explained by the mechanical model to the mathematically robust non-linear analysis. Here, we considered PS homopolymers of three molecular weights (15 kg/mol - Đ: 1.06, 50 kg/mol - Đ: 1.03, 124 kg/mol - Đ: 1.28) and the composites with 2 and 7 and 15 wt% fillers analyzed in the previous sections. LAOS measurements on PS homopolymers were performed at 150 ± 0.05°C under nitrogen environment in a strain-controlled rheometer (ARES-G2, TA Instruments) using a parallel plate geometry and at ω=1 rad/sec. 48 cycles of deformation with γ_0 = 1 and 4 were applied to the samples and data is collected at the sampling frequency of 300 Hz. The stress response averaged from

the last 7 cycles (in the steady state) was decomposed into its elastic and viscous components[60] and analyzed in Fourier-Chebyshev framework[61]. Sample preparation for composites and their deformation protocol consisting of oscillating cycles and resting times were described in the previous section.

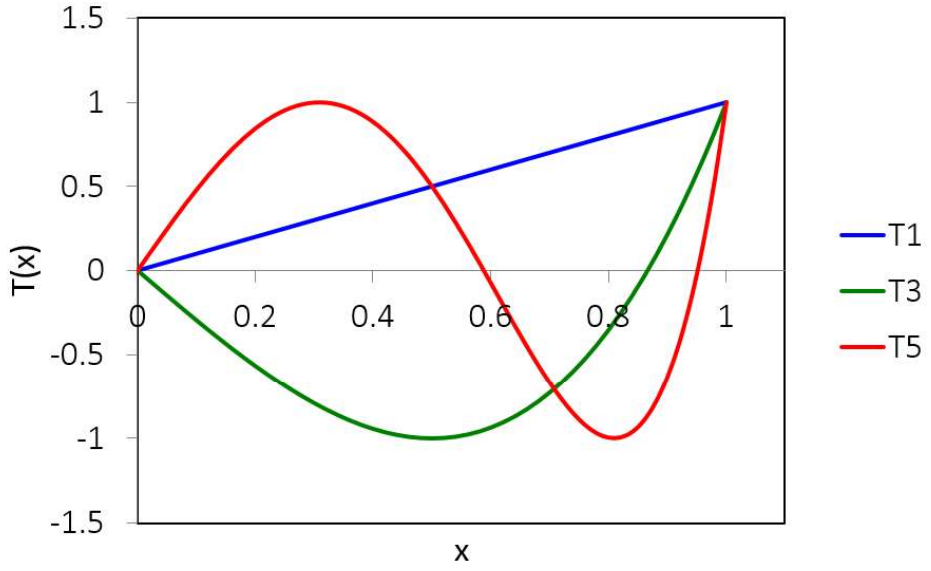

Figure 2. 9. The first (T_1), third (T_3) and fifth (T_5) order bases of Chebyshev polynomials of the 1st kind. x represents the normalized strain, $\gamma(t)/\gamma_0$.

First, we discuss the deformation of homopolymers. Figure 2.9a shows the normalized stress-strain curves for different molecular weights of homopolymer strained at γ_0=2. It is clear that chain length has a pronounced effect on strain-stiffening observed at large strains. Stretching of a Gaussian coil is mainly entropic at small strains and it reaches a limit as the chain is extended to its finite length. We fit the stress-strain data to

non-linear stress function $\sigma = (G_{pol}\gamma/3)\left[1+2\left(1-\beta I_1(\gamma)/3\right)^{-2}\right]$ developed for polymer networks where G_{pol} (shear modulus of polymer) and β (chain elongation ratio) are the fitting parameters and $I_1(\gamma) = \gamma^2 + 3$ is the first invariant for the shear deformation[64]. The Chebyshev polynomial fittings to the same elastic stress-strain response provided elastic constants, e_1 and e_3. Figure 2.9b presents the first harmonic material functions scale with molecular weight as $e_1 = G_1^{'} \propto M_w^{\,3}$, representing the average elasticity of the materials. The deviation in non-linearities of the 15 kg/mol polymer rises as it is much lower than the critical entanglement molecular weight of PS (32 kg/mole)[65]. β is defined as $\beta = < R_0^{\,2} > / R_{\max}^{\,2}$ where $< R_0^{\,2} >$ is the mean square end-to-end distance of an unperturbed chain and $R_{\max}$ is the length of the fully stretched chain. Since $< R_0^{\,2} > \propto bN^2$ and $R_{\max} \propto bN$, the non-linear parameter β is inversely proportional to contour length (i.e. $\beta \propto N^{-1} \propto M_n^{\,-1}$) as shown experimentally in Figure 2.9c. This scaling seems to be valid for a range of strain amplitudes which implies that β is an intrinsic material property. The molecular weight dependences of non-linearities in the experimental data, i.e. variation in β, and non-linear Chebyshev fittings scale as $e_3/e_1 \propto \beta^2$. Thus, our analysis suggests that magnitude of the third order harmonic relative to the fundamental harmonic may be related to the finite extensibility of polymer chains.

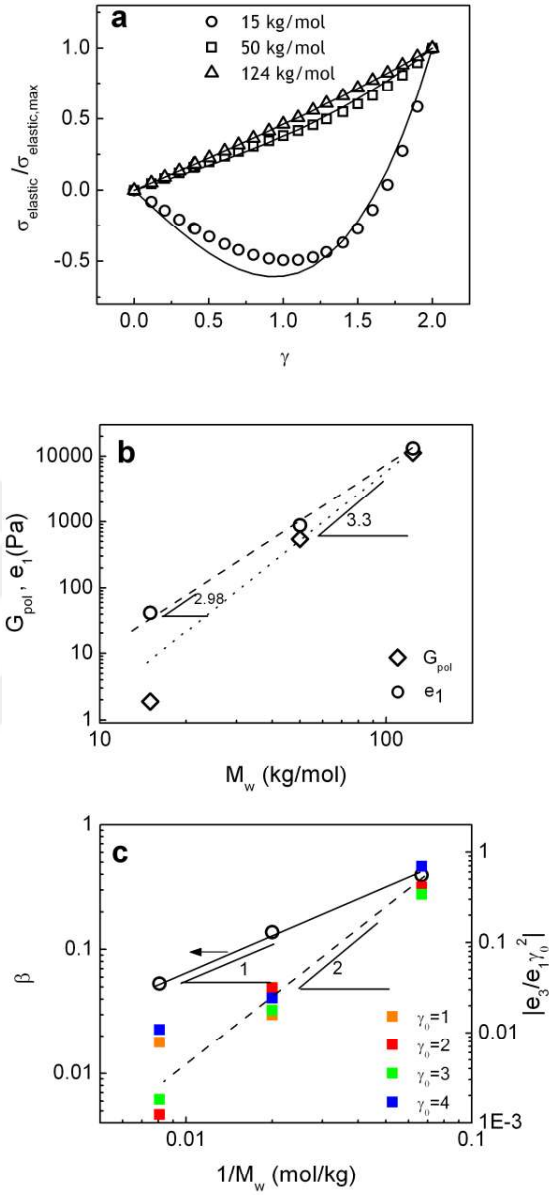

Figure 2. 10. (a) Normalized stress-strain curves for PS homopolymers of different molecular weights and corresponding Chebyshev polynomial fits with the first and third order basis. **(b)** The first order Chebyshev coefficient and G_{pol} determined from the

mechanical model present molecular weight dependence (~M_w^3). **(c)** Chain extension ratio (β) and non-linearities as a function of inverse molecular weight for 15, 50 and 124 kg/mol PS homopolymers obtained at $\gamma_0 = 2$.

Extension ratio is inversely proportional to molecular weight (~M_w^{-1}) as predicted by its definition. Magnitude of the third order Chebyshev coefficient relative to the first order coefficient presents inverse quadratic dependence on molecular weight (~ M_w^{-2}). Next, we analyzed the effect of nanoparticles on non-linearities in polymer nanocomposites. We notice in Figure 2.10 that e_1 and e_3 (Chebyshev coefficients of elastic non-linearities for the first and third order harmonics) are not sufficient to describe the behavior of composites as opposed to homopolymer where the third harmonic sufficiently describe the non-linearities. When e_5 is included, the initial and yield stresses are successfully captured. Figure 2.11a shows that the average elastic modulus (G_1') linearly increases with particle loading. The magnitude of e_3/e_1 decreases in the presence of particles (Figure 2.11b). In contrast, the magnitude of e_5/e_3 increases monotonically with particle loading and e_5 leads to non-linearities. This result in conjunction with the mechanical model suggests that the appearance of e_5 (thus G_5' in FTR) is due to percolated network of nanoparticles and can be related to the particle-particle interactions in polymer repulsive nanocomposites.

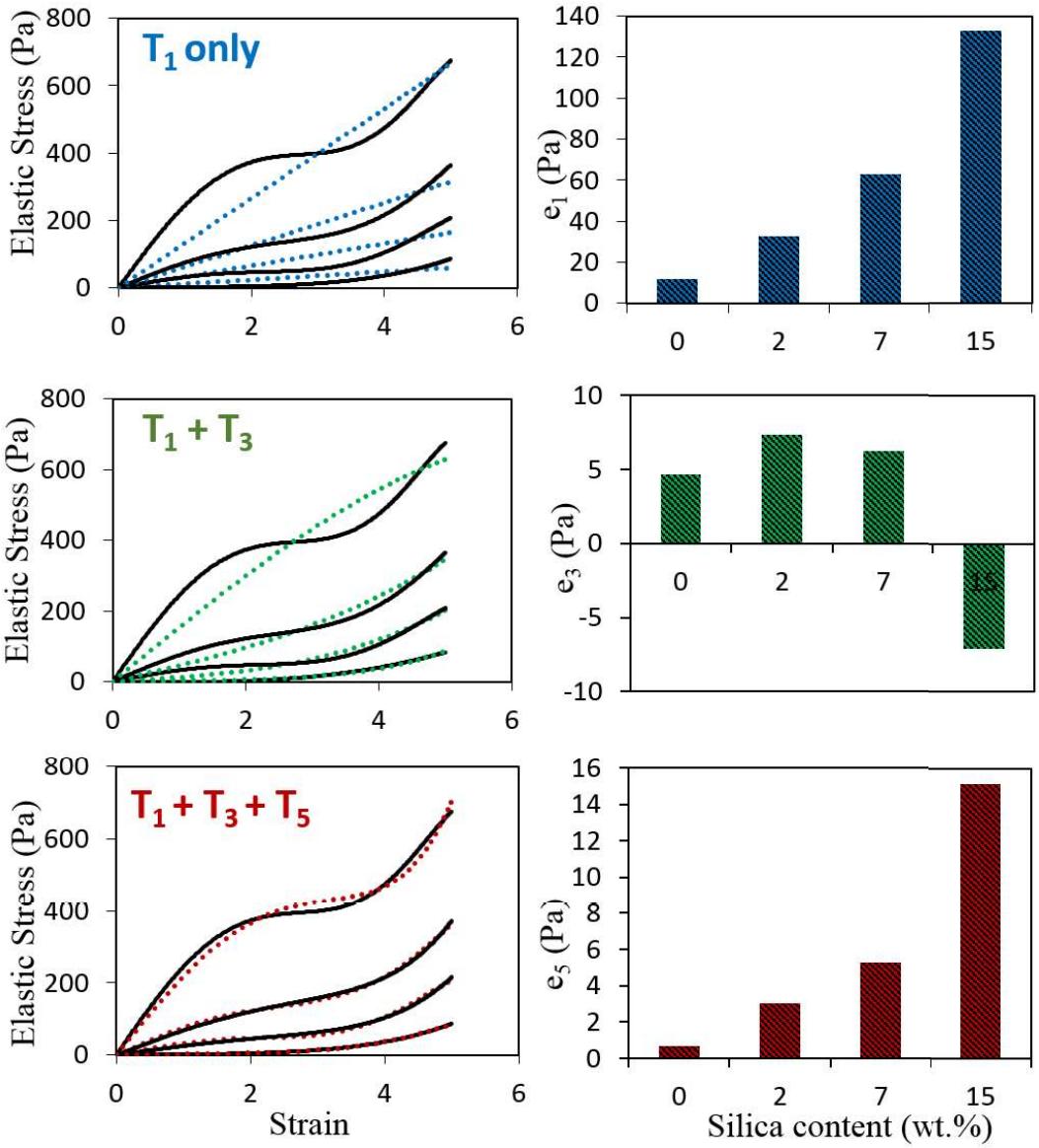

Figure 2. 11. Elastic stress-strain data of nanocomposites and PS homopolymer (50 kg/mol) at different particle loadings of 2, 7 and 15 wt%. The dashed lines represent the fittings consisting of the high-order harmonics at n = 1 and 3 (green line) and n = 1, 3 and 5 (red line).

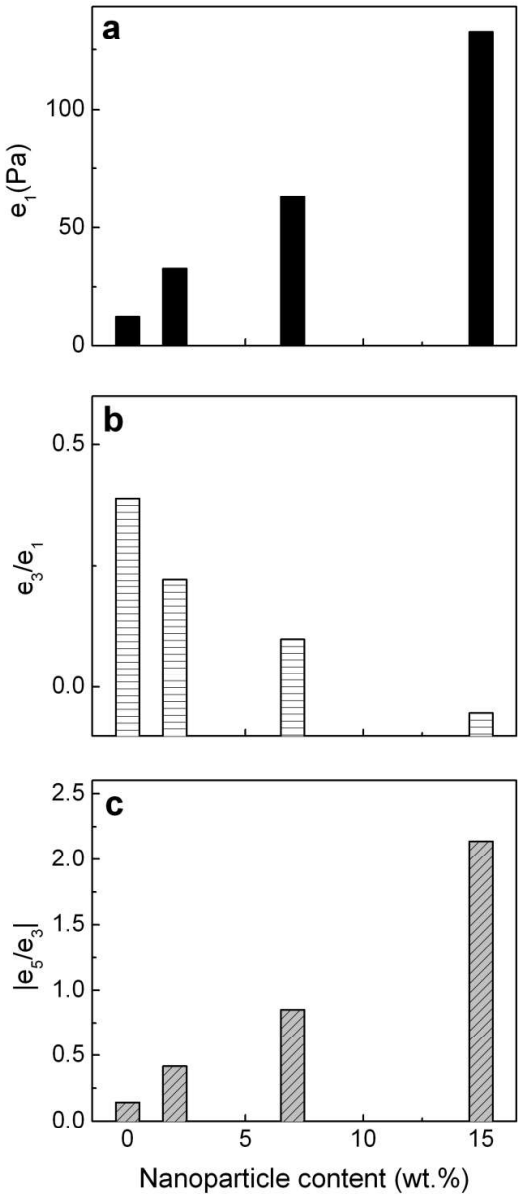

Figure 2. 12. (a) Average elastic modulus monotonically increases with particle wt%. **(b)** e_3/e_1 decreases with particle content indicating decrease in chain elongation ratio in composites. **(c)** The fifth order measure relative to the third order coefficient increases with particle wt%.

The yield strain may also be predicted from the Chebyshev fittings. An accurate definition of the yield strain is the strain at which the stress curve has maximum curvature[40] $\left|\partial^2\sigma/\partial\gamma^2\right|$=max and $\partial^3\sigma_e(x;\omega,\gamma)/\partial\gamma^3\big|_{\gamma_y} = \gamma_0 \sum_{n=odd}^{5} e_n(\omega,\gamma_0)\,\partial^3 T_n(x)/\partial\gamma^3\big|_{\gamma_y} = 0$ .The yield strain becomes $\gamma_y = \sqrt{1/2 - e_3/10e_5}\,/2$. The predicted yield strain (1.55±0.3) is found to be very close to the experimental value (1.6), thus e_5/e_3 ratio can be used to estimate the yield strain. We note that when $e_3/e_5 > 5$, γ_y the prediction is not physically meaningful!

Figure 2.12 shows the evolution of e_3/e_1 and e_5/e_1 as a function of waiting time. A decrease of e_5/e_1 is denoted to the clustering of particles, mostly occurring at resting in which the chain extension appears prominent with the increase in e_3/e_1 during this clustering. Upon further deformation and resting, particle originated non-linearities reappear and initial structures are recovered. Thus, the magnitude of e_5 (or $G_5^{'}$) may be a useful tool to measure of dispersion quality in nanocomposites.

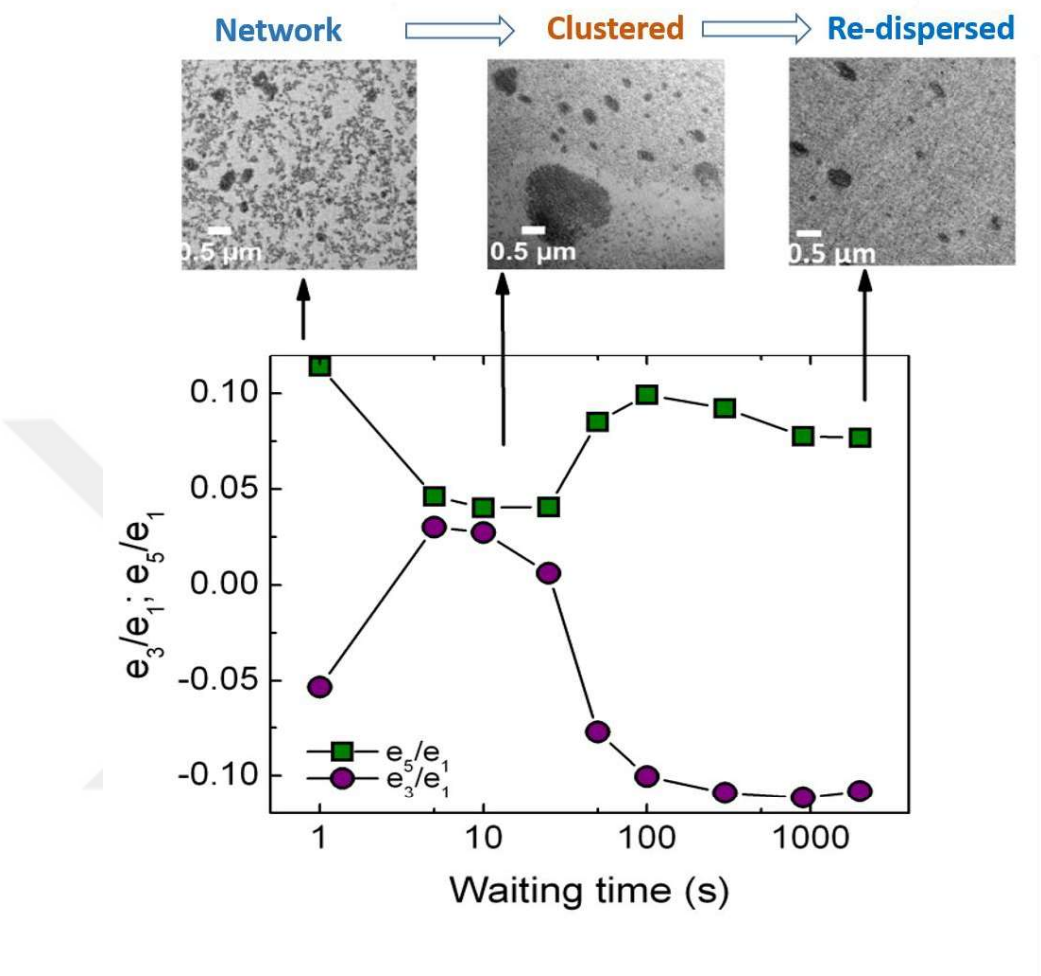

Figure 2. 13. Evolution of e_3 and e_5 relative to e_1 as a function of resting time. TEM micrographs show dispersion of nanoparticles at initial, 10 sec and 2000 sec resting following deformation.

2.5. Chapter Conclusions

In summary, we have reported the elastic stress contributions from particle and polymer components of silica filled PS composites in large-amplitude oscillatory measurements. We show that stress response at small strains is the result of percolated particle network whereas large strain behavior is determined by the polymer extension. By examining the structures of composites at different deformation states, we have shown that the reformation of initial structures is driven by the particles diffusing in liquid polymer during rest times. We have suggested a mechanistic analog for the deformation mechanism and demonstrated that the elastic stress-strain response of nanocomposites is in good agreement with the non-linear deformation theory for the polymer that is coupled with the power law expression corresponding to the particles' deformation. Through LAOS and TEM experiment results, we conclude that when a nanocomposite is deformed at large strains, polymer chains are highly stretched around nanoparticles, and composites strain-harden as analogous to polymeric networks under deformation. The non-linear mechanical results presented here for a repulsive composite system showcase the importance of filler-polymer interactions and filler dispersion on the elastic response of reinforced nanocomposites. In addition, we compared our mechanistic model and LAOS fingerprinting methods. LAOS experiment protocols presented here can be applied to other composite systems such as grafted polymers and attractive composites to separate the mechanical differences between bound layer existing systems and polymer-grafted nanoparticles. We conjecture that the deformation of grafted and matrix homopolymers can both contribute to the elastic stress while deformation of

bound homopolymer around particles will be rather different and possibly require more complicated modeling which will be the focus of future studies.

CHAPTER 3

AN INTERPHASE DRIVEN STIFFENING MECHANISM IN POLYMER NANOCOMPOSITES[2]

Chapter Summary

Dynamic mechanical response in responsive and adaptive composites can be achieved through a responsive polymer; with the chemical regulators affecting the bonding between fillers, or through reversible covalent bonding. Tuning the interphases between fillers and polymer matrix can play a critical role in all these systems to enhance their adaptive responses. Here, we present that the bonding-debonding of chains on nanoparticles can be modulated under extensive periodic strains. Mechanical response of an attractive model polymer composite, PMMA filled with silica nanoparticles, is monitored in a series of deformation-resting experiments allowing us to tune the interfacial strength of polymer. Chains that are desorbed from the surface with the oscillatory shear entangle with the free chains during the rest time. We show that a periodic deformation process results in unusual stiffening of composites. Mechanical response during the recovery reveals this behavior arising from the enhancement in the entanglement of chains at interphases. The interfacial hardening can be used in designing polymer composites with stress-sensitive interphases to achieve new repair mechanisms for biomedical applications, and also in energy absorbing reinforced systems.

---

[2] Reproduced with permission from [Senses, E., & Akcora, P. (2013). An interface-driven stiffening mechanism in polymer nanocomposites. Macromolecules, 46(5), 1868-1874.] Copyright [2013] American Chemical Society

3.1. Introduction

Use of inorganic blocks in polymer matrices has been an efficient method for nature to render strength and response mechanisms of hybrid materials[66,67,68,69,70,71,72]. The structure and mechanical behavior of biological materials has been extensively studied, however, it still remains a challenge to mimic their structures and response mechanisms. In biominerals and biomimetic systems, the organic matrix plays an important role as its interaction with the inorganic component determines its functioning[73,74]. For example, the collagen fibrils of bone are held by an organic matrix and the bone stiffens through calcium-mediated sacrificial bonds[75,76]. Upon stretching the matrix chains, bonds between matrix and collagen fibrils break but can reform when relaxed. The possibility of designing adaptive materials in a similar way as nature, has generated wide interest in responsive nanocomposites for diverse applications such as drug delivery, biosensors, and microelectromechanical systems[66,77]. Photo,[78] temperature[79], pH[66], and chemo responsive polymers[80] regulate their mechanical properties with different mechanisms; all in which nanoscale interactions play a key role in their polymer networks, mesophases, or composites. The chemo-responsive mechanical adaptability of a sea cucumber skin[71] is one example of how chemical regulators can be effective when the nanofibers interact through strong hydrogen bonds. Inspired by the nanoscale interactions in natural composites, we focus on a synthetic polymer composite having attractive interactions between its polymer matrix and inorganic fillers to explore the role of the interfacial layer on their mechanical response.

The dynamics of interfacial and confined polymers in composites with attractive particle-polymer interactions is explored in various simulations and experimental studies[81,82,17]. The enthalpy gained with the favorable monomer-surface interaction is balanced by the decrease in entropy of the chain, resulting in the formation of an adsorbed polymer layer in tails and a low fraction of loops and trains on the surfaces[83]. Moreover, adsorption of polymer chains adjacent to an attractive surface leads to an increases in glass transition temperature; which also reveals the dynamic heterogeneities in polymer relaxation[84,85,13]. The interaction of the adsorbed polymer with the free matrix chains can potentially change the mechanical behavior of composites. Correspondingly, such attractive systems can present unusual mechanical responses if the entanglement density of the interfacial layer is altered. Riggleman et al.[86] have hypothesized in their simulation work that a distinct mechanical response at large deformation is possible for a system with strong particle-polymer interactions. Here, we present the stiffening of such composites with attractive polymer-particle interactions under deformation experimentally and elaborate on the mechanism of the process which occurs through reversible adsorption-desorption of chains. Our results delineate the role of entanglement density on response dynamics. The observed behavior is clearly different than strain-stiffening of polymeric and biological networks under dynamic stresses[87,88]. Moreover, adsorption of polymer chains on attractive surfaces can be enhanced when their molecular conformation is affected through interactions with the surface. We examine the elastic properties of polymer composites under various deformation conditions and demonstrate that polymers having attractive interfacial interactions with their fillers can

strengthen after shear. This behavior, which is manifested only after large strains and for well-defined interfacial distances, offers tunable reinforcement properties to polymer nanocomposites, implying that the composite can stiffen as needed.

3.2. Experimental Section

3.2.1. Sample preparation

PMMA of 36 kg/mole, synthesized by ATRP method, is mixed with colloidal silica nanoparticles (supplied by Nissan Chemicals) in 1,2-Dichlorobenzene by bath sonication for 30 min and then stirred rigorously for 2 h. After sonication for an additional 30 min, the solution was immediately poured into a glass dish placed in an oven preheated at 130 ^{o}C. The evaporation of the solvent was completed under -38 cm-Hg gauge pressure in approximately 1 h and the final ~250 μm films were annealed at 130 ^{o}C for 4 days and at 150 ^{o}C for 3 days under vacuum. We further annealed the films at 180 ^{o}C for 2 h under vacuum to ensure complete removal of the solvent.

3.2.2. Structural Characterization

The particle structures in bulk films were determined using TEM microscopy (Philips CM20 FEG TEM/STEM) on as-prepared samples. SAXS patterns of samples were obtained at beamline X27C at the National Synchrotron Light Source of Brookhaven National Laboratory. The air-background subtracted data were fit to the Beaucage unified equation; $I(q) = \sum_i G_i \exp(-q^2 R_{gi}{}^2/3) + B_i[\frac{(erf(qR_{gi}/\sqrt{6}))^3}{q}]^{p_i}$, where R_g is the radius of gyration, p is the fractal dimension of the scattering objects, and G_i,

and B_i are constants for i^{th} structural level. For our samples, only one level fit was sufficient to describe the patterns.

SANS measurements were performed at the BL-6 (extended q-range SANS) in the Spallation Neutron Source at the Oak Ridge National Laboratory (ORNL). Hydrogenated PMMA (M_w = 45.4 kg/mole, Đ: 1.23, SLD: $1.06*10^{-6}$ $Å^{-2}$) was mixed with deuterated PMMA (Polymer Source Inc.,M_w = 45 kg/mole, Đ: 1.10, SLD: $5.18*10^{-6}$ $Å^{-2}$) to contrast match with silica (SLD: $3.41*10^{-6}$ $Å^{-2}$). The measurements were performed at $0.028\ Å^{-1} < q < 1.25\ Å^{-1}$.

3.2.3. Rheology

Rheology measurements were performed on a strain-controlled ARES-G2 rheometer (TA Instruments) equipped with 8-mm diameter parallel plate geometry under nitrogen. The samples annealed according to above procedure were molded with a vacuum assisted compression molder at 180 ^oC for 10 min. Samples were finally annealed at 130 ^oC for 12 h. The measurements were performed at 210 ^oC following sample equilibration time of 10 min. Time sweep experiments during this period confirmed the sample stability. We additionally performed time sweep experiments for longer times (Appendix 2, Figure A2.2) and observed no time dependence. Large amplitude oscillatory shear (LAOS) tests were performed at an angular frequency of 1 rad/sec. Time dependence of the stiffening was determined by fixing the strain amplitude at 300% and allowing the sample rested for increasing periods of waiting times (5-2000 sec) between 20 cycles of large deformation. Time sweep experiments (with small strains) allowed monitoring the evolutions of the modulus during rest times. Strain

amplitude dependence was tested by fixing the waiting time at 900 sec between 30 cycles of periodic strains and repeating the measurements with different amplitudes (from 50% to 500%). Data were collected at a sampling frequency of 300 Hz, giving 1885 points per cycle. After completing each test, samples were cooled below T_g in one minute. The gap was adjusted so that normal force never exceeds +/- 1N. This prevented deformation of the sample during the cooling step.

3.2.4. Rheology data analysis

In a typical small amplitude oscillatory shear experiment, a sinusoidal strain, $\gamma(t) = \gamma_0 \sin\omega t$, is applied in the linear viscolestic region with strain amplitude (γ_0) and frequency (ω) and the stress response is measured. Similar to the dynamic viscoelastic measurements, a sinusoidal strain is applied in a typical large amplitude oscillatory shear test. The stress response to large strains is still periodic but not purely sinusoidal. Thus, the elastic and viscous components of the total stress cannot be obtained directly as in the case of small periodic deformation. Instead, stress can be decomposed into its purely elastic and viscous components by using geometric arguments[36]. This method utilized the idea that elastic stress should exhibit odd-symmetry with respect to sin(ωt) and even symmetry with respect to cos(ωt) and that the viscous stress should exhibit odd-symmetry to cos(ωt) and even symmetry to sin(ωt). Stress decomposition is performed by using MITLaos software[39] and the modulus is calculated from the elastic component of the total stress. Since the sample is deformed during 20-30 cycles of deformation in each step, only the initial few cycles contain the structural information from the previous rest time; thus, we analyzed the LAOS response averaged from the stress response

between the 2nd and 5th cycles. We specifically were very careful about experimental artifact due to sample deformation and rheological instabilities.

3.2.5. Fourier-Transform Infrared Spectroscopy analysis

Samples for IR characterization are molded to specific thicknesses using the parallel plates of rheometer at 190 ^{o}C under nitrogen by applying a constant force of 1N. During sample cooling the normal force is kept in the range of ±0.5N, adjusting the gap automatically to prevent any thermal strain. Absorption spectra are obtained using a Tensor 27 FTIR spectrometer (Bruker Optics) in the range of 400-4000 cm^{-1} with 60 scans of 4 cm^{-1} resolution.

3.3. Results and Discussion

3.3.1. Dispersion and Linear Viscoelastic Response

We chose poly(methyl methacrylate) (PMMA) for our organic matrix because it is known that PMMA interacts with the hydroxyl groups on silica surfaces via hydrogen bonding[14,89]. This interaction favors the physical adsorption of the polymer chains to the nanoparticle surfaces, allowing us to investigate the stiffening mechanism at the interphases. We dispersed spherical silica nanoparticles of two different sizes (13 and 56 nm in diameter) at various compositions (2-50 wt%) in a PMMA matrix (36 kg/mol, ~~Đ~~: 1.03). Using spherical nanoparticles rather than anisotropic nanoparticles has notable advantage as the latter has low percolation threshold where particle network can contribute to the overall stress response. Figures 3.1 show the well-dispersion states of all compositions for 13 and 56 nm nanoparticles in PMMA homopolymer. SAXS data for composites consisting of 13 nm particles (Figure 3.2a) verified that size of particles

obtained from the Unified fittings is close to the actual radius of particles (Appendix 2 Table A2.1).

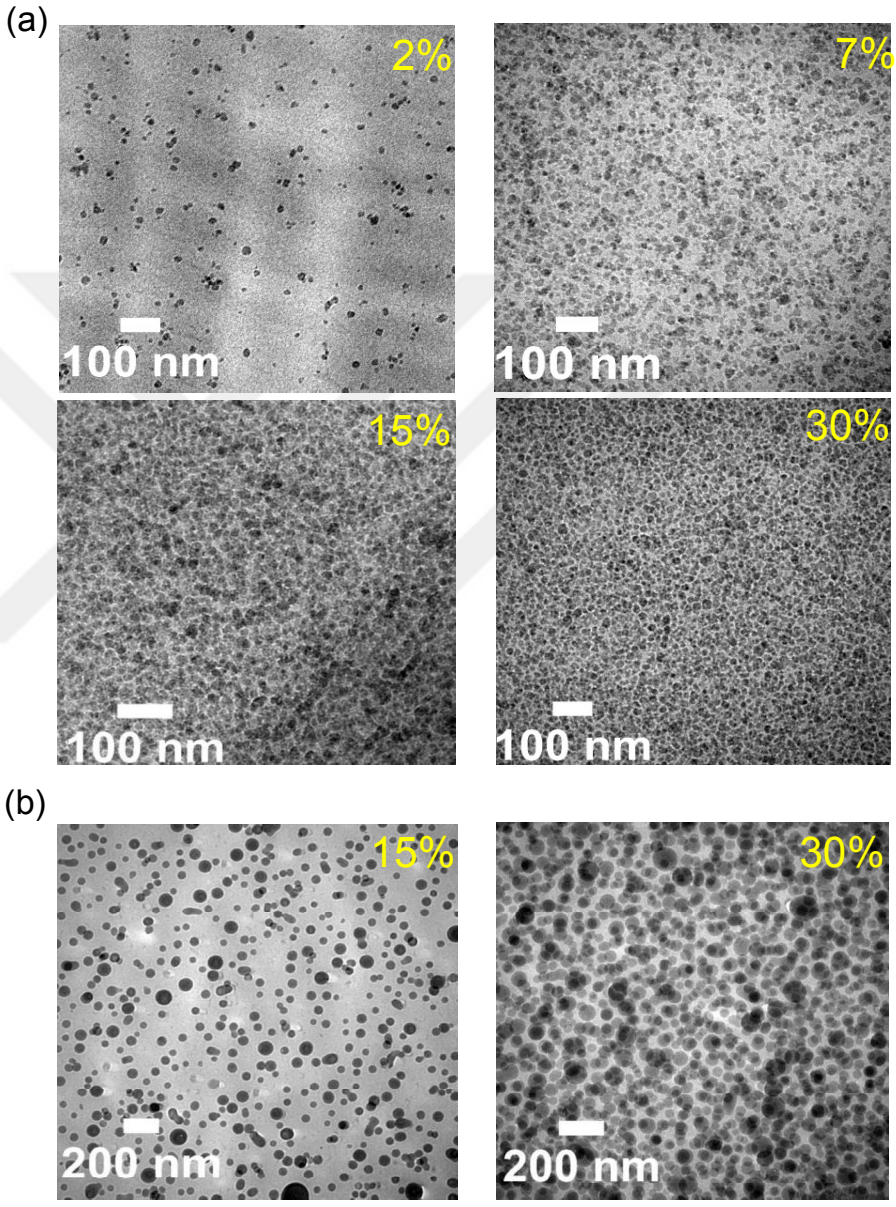

Figure 3. 1. Transmission electron micrographs of PMMA (36 kg/mol) composites filled with **(a)** 13 nm **(b)** 56 nm SiO_2 nanoparticles.

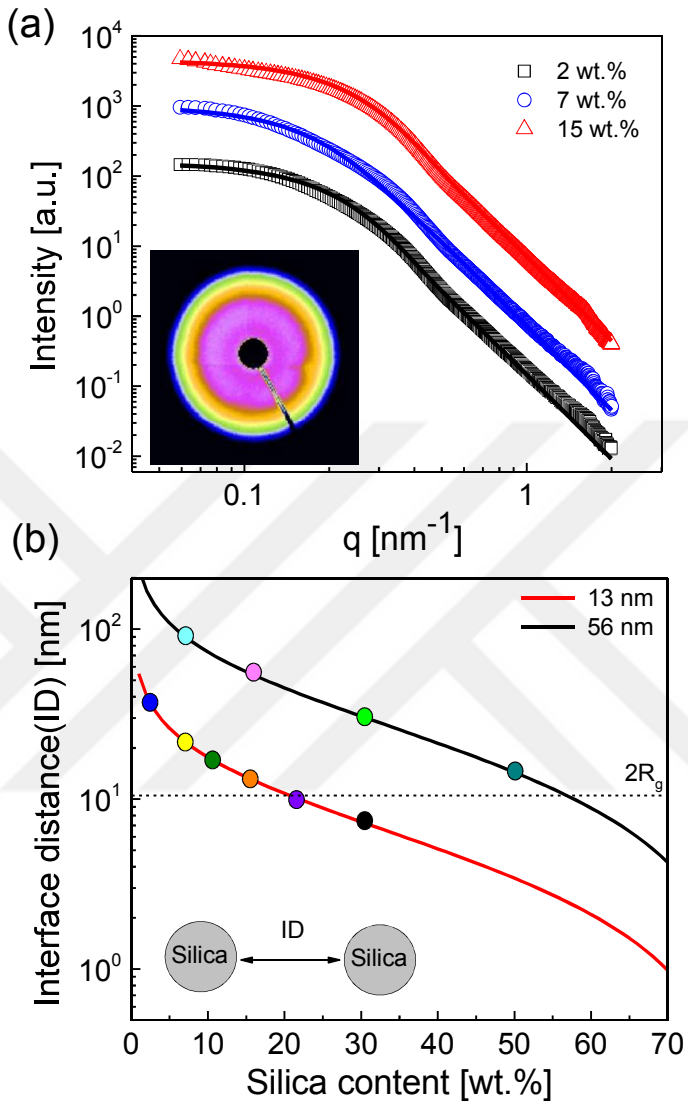

Figure 3. 2. (a) SAXS results for PMMA composites containing 13 nm particles. Lines are the 1-level unified fittings to the data. The inset image is a representative 2D SAXS pattern for 15% sample. **(b)** Interparticle distance (ID) as a function of concentration for randomly packed spherical SiO_2 nanoparticles of different sizes. Marks on curves represent sample compositions used in this work.

The slope at the Porod region was found to be -4 for all compositions, which further confirms that the particles are individually dispersed with sharp interfaces. Figure 3.2b represents the face-to-face interparticle distance at various particle loadings calculated using $ID = d\left[\left(\frac{\phi_{max}}{\phi}\right)^{1/3}\left[\exp(\ln\sigma)^2\right] - 1\right]$ where d is the number average particle diameter, σ is the polydispersity of the particles, and ϕ_{max} is the maximum volume packing fraction which is $2/\pi$ for the randomly distributed particles[90]. We determined the number average particle sizes and polydispersities from Dynamic Light Scattering (DLS) to be 13.1 nm (σ = 1.18) and 56.3 nm (σ = 1.17). The size of the polymer ($2R_g$) is calculated to be 11 nm (see Appendix 2 for calculations). By changing the loading amounts of 13 nm particles from 2-30 wt%, polymer chains are confined when $ID/2R_g<1$, whereas with 56 nm particles, the chains are not confined since $ID/2R_g>>1$. In this work, we systematically investigated the effect of confinement on the large deformation mechanical response of composites presenting individually dispersed nanoparticles.

We first obtained the linear viscoelastic response of the well-dispersed composites at 210 ^oC. Figure 3.3a shows the storage moduli (G') and loss angle for the composites. It is seen that the frequency dependence of the moduli is not significantly changed for the samples with $ID/2R_g>1$. Composites with 13 nm particles show significant deviation from neat PMMA at 30% loading whereas a similar response is achieved with 56 nm particles at 50 wt%. To further quantify the effect of interparticle separation on the equilibrium (linear) viscoelastic behavior, we calculated the reinforcement factor at 1

rad/sec as the ratio of the elastic modulus of the composites with respect to that of neat polymer. Figure 3.3b suggests that similar level of reinforcement is obtained at larger $ID/2R_g$ for large particles compared to smaller ones, possibly due to denser adsorbed layer form on larger particles avoiding impeding curvature effect on chain adsorption.[13]

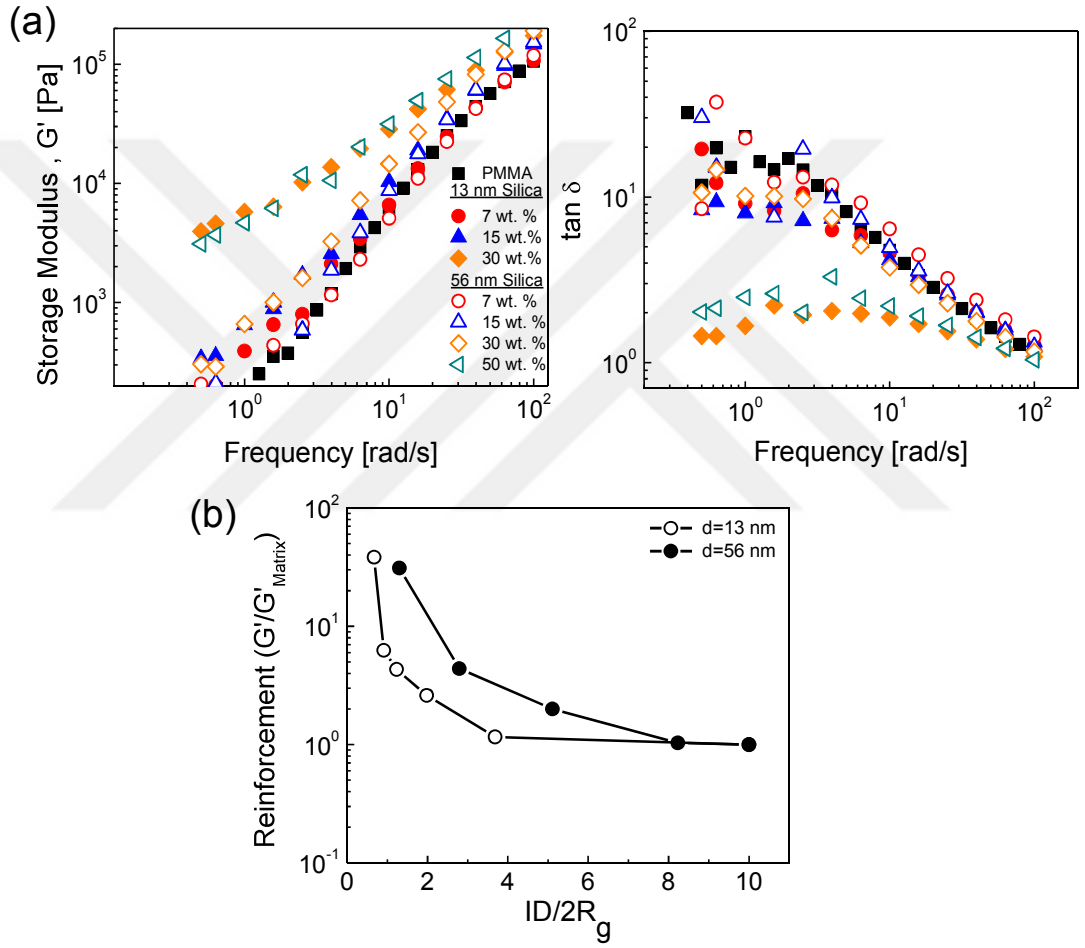

Figure 3. 3. **(a)** Linear elastic (G') modulus and loss angle behavior of PMMA (36 kg/mol) and its composites with 13 and 56 nm silica nanoparticles at different loadings at 210 ^{o}C. **(b)** Reinforcement factor calculated from linear elastic modulus data at 1 rad/sec frequency.

3.3.2. Response to Large Amplitude Deformation

Next, we deformed the samples periodically with a strain amplitude ($\gamma(t) = \gamma_0 \sin(\omega t)$), greater than the maximum limit of the linear viscoelasticity at 210 ^{o}C. In a cycle of deformation, the strain is increased from zero to γ_0 in a certain time range (quarter of the oscillation period, $\pi/2\omega$) and decreased to zero at a time equal to half of the period. This motion is then repeated in the same manner but in the opposite direction and the cycle is completed at one oscillation period. Cycles provide dynamic properties such as moduli and viscosity in the non-linear region (see experimental section for details). As the samples are sheared at large-strain amplitudes, physical bonds between polymer and nanoparticles at the surface can be broken and polymer segments can be desorbed from the surface. This continuous deformation of samples results in an initial strain softening due to chain desorption. When deformation stops for specified waiting times, polymer chains relax and can be readsorbed to the surface.

To monitor time evolution of this process, we designed an experimental protocol where samples are subjected to rest at varying times between deformation cycles. This deformation-waiting cycle timelines of our protocol are described in Figure 3.4a. In the first experimental set, we applied 20 cycles of sine strains with $\gamma_0 = 3$ and at $\omega = 1$ rad/sec. Between each deformation step, the samples are allowed to rest for certain periods of time, increasing from 5 to 2000 sec. Figure 3.4b shows that the storage moduli of composites increase with particle loadings with longer waiting times after deformation and this behavior is shown to be limited by 22 wt% loading. To highlight the increase in

the moduli values with respect to their initial modulus, we present the normalized non-linear data with resting time in Figure 3.4d.

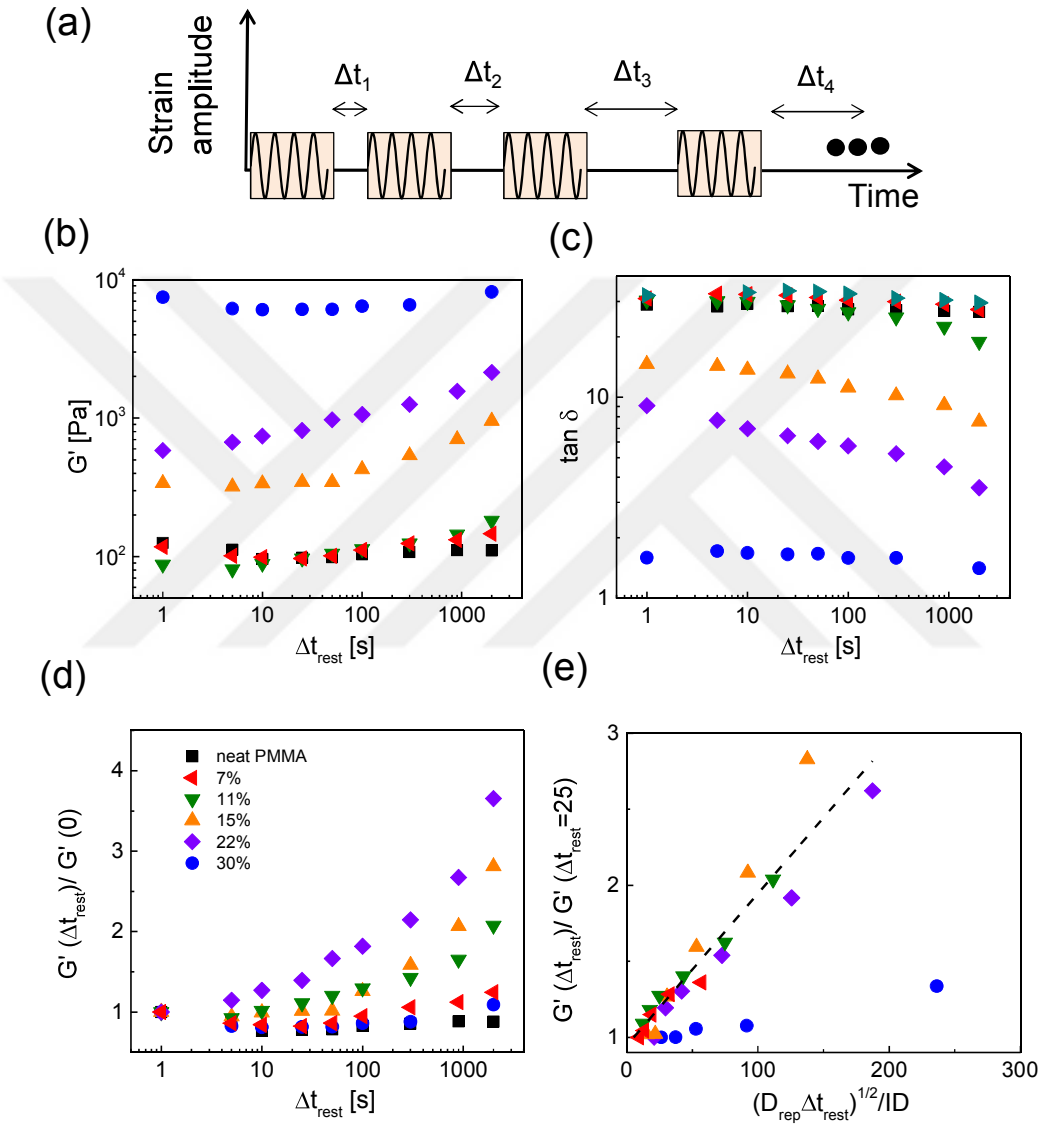

Figure 3. 4. (a) Diagram of deformation-wait time experiments. 20 cycles of sinusoidal strain at 300% amplitude is applied in each deformation with various waiting times (5, 10, 25, 50, 100, 300, 900 and 2000 sec) at 210 ^{o}C. **(b)** Elastic moduli and **(c)** loss tangent

(tanδ) of PMMA homopolymer and composites at 210^{o}C from non-linear deformation experiments**. (d)** Elastic modulus normalized to the initial modulus versus waiting time for PMMA homopolymer and PMMA-Si composites with 13 nm particles. **(e)** Stiffening of PMMA-Si composites with 13 nm particles represented as a function of the ratio of the diffusion distance to inter-particle distance (x/ID). Lines are guides to the eye.

The modulus of 30 wt% composite does not change with deformation and resting as shown in Figures 3.4b and 3.4d, because free chains cannot interact with the adsorbed polymer layer at such small interparticle distances (ID/2Rg<1). This continuous cycle enhances both the entanglement of the desorbed chains with the free matrix chains and the molecular alignment of the PMMA molecules during resting. The deformation and adsorption processes form a dense adsorbed layer, resulting in a strengthening at the interface of the adsorbed polymer. Nanocomposites with 56 nm particles showed no significant stiffening as they are all above the confinement region (Appendix 2 Figure A2.1). Loss tangent (tanδ) values of Figure 3.4c clearly displays the deviation from the liquid-like behavior and becomes more solid-like with deformation for all the composites excluding 30 wt%, while tanδ of homopolymer does not change with resting time.

To validate the argument of strengthening during the waiting times, we calculated the diffusion distance of a reptating chain during the resting time (Δt_{rest}). Reptation time, τ_{rep} , is calculated from our linear viscoelastic measurements as 0.02 sec at 210 ^{o}C (see Appendix A2 for details). Diffusion coefficient (D_{rep}) of a reptating chain can therefore be calculated from $D_{rep} = R_g^{\,2} / \tau_{rep}$ as 1512 nm^2/s. Thus, the diffusion distance of the

reptating chain scales as $x \sim (D_{rep}\Delta t_{rest})^{1/2}$. The normalized modulus data as a function of x/ID for each composition having 13 nm particles falls on the same line (Figure 3.4e), indicating that diffusing chains determine the overall stiffening at all particle compositions except at 30 wt%. Next, we investigated the effect of strain amplitude on the stiffening mechanism. The strain amplitude is a critical parameter for stiffening since it determines the energy input to the system. For this purpose, we performed experiments at different strain amplitudes while keeping the waiting times fixed at 900 sec (Figure 3.5a), sufficient time to observe stiffening for 15% and 22% loadings. Samples were subjected to 30 deformation cycles at different strain amplitudes ranging from 50 to 500%. 30 cycles were chosen to ensure that the stress response reaches to steady-state for all compositions. For 15 and 22 wt% composites, there is a critical strain amplitude around 300% where the plateau modulus is reached (Figure 3.5b). Homopolymer and 7 wt% composite do not exhibit stiffening over time at any strain amplitude. This suggests that the free matrix chains are dominating the response for those samples. We note that the loop concentration at the interphase is presumably saturated at the critical strain and further interaction of the free chains with the adsorbed layer is limited. We have done similar deformation-waiting experiments on a composite system (polystyrene-silica, PS-Si) where interactions between polymer and particles are repulsive. Contrary to PMMA, we observed that a repulsive system strain-soften under cyclic deformations in the vicinity of particles (see Chapter 1).

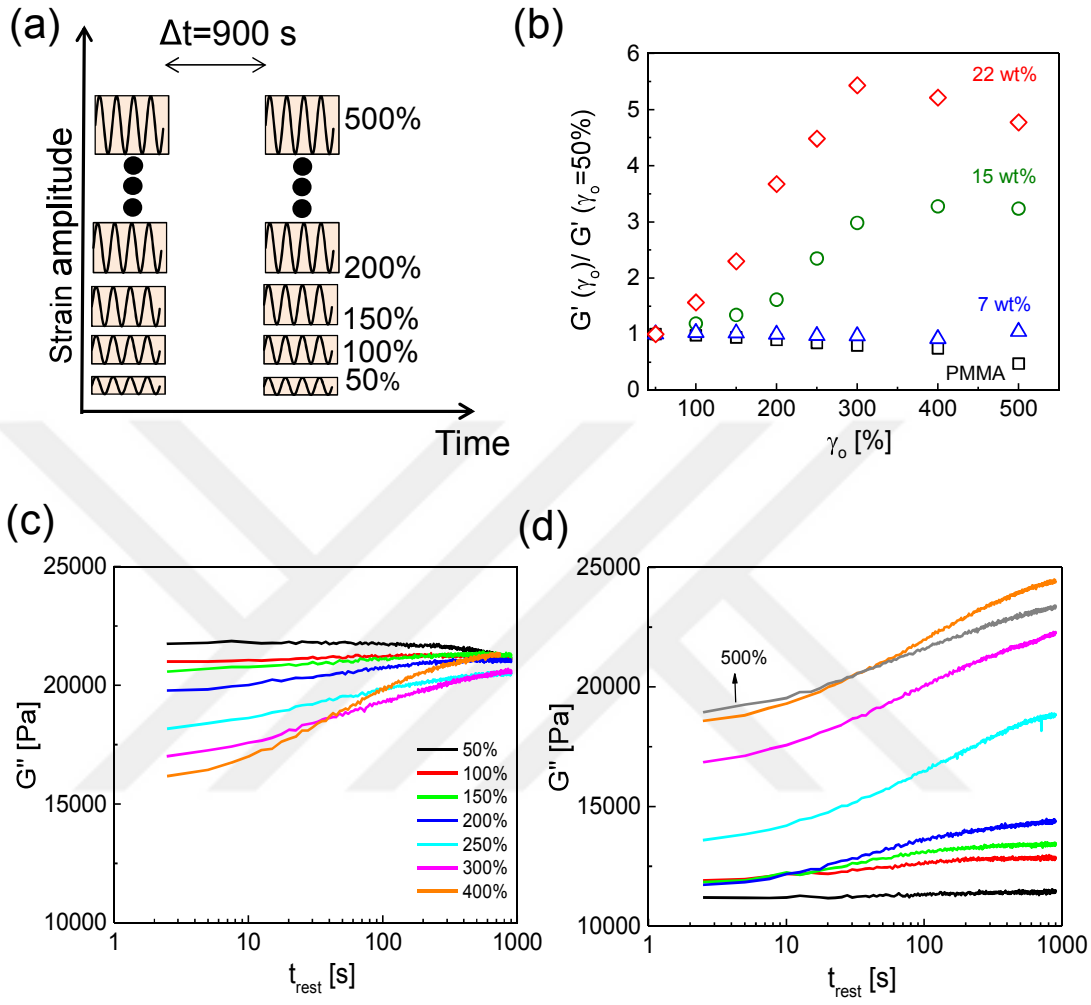

Figure 3. 5. (a) Diagram of deformation-strain amplitude experiments for PMMA system. 30 cycles of sinusoidal strain are applied in each deformation step. The rest time is kept constant at 900 sec. The moduli for different strain amplitudes after 900 sec waiting time are normalized with the moduli for γ_0=0.5. **(b)** Normalized modulus of PMMA composites versus strain amplitude for 0, 7, 15 and 22 wt% particle compositions. Small-strain time sweeps during 900 s rest times for **(c)** homopolymer at 5

rad/sec and **(d)** 15% PMMA composite 1 rad/sec, measured at 210 ^{o}C after deformation at different strain amplitudes from 50% to 500%..

Characteristic Lissajous plots and elastic stress-strain curves of attractive PMMA-Si and repulsive PS-SiO_2 composites at different deformation states are shown in Figure 3.6. The elastic stress-strain response revealed a clear yield-like behavior for PS-SiO_2 at the intermediate strains. TEM images obtained at different stages of the deformation (shown in Figure 3.7) suggested that the rupture of particle network results in strain softening behavior, contrary to stiffening observed for PMMA-SiO_2 system. The sharp increase in the stress-strain curves of attractive composites is the result of interfacial strengthening. Further, we verify the particle size after deformation in PMMA-Si through small-angle neutron scattering (SANS) experiments (Appendix Figure A2.2 and Table A2.2). This information leads us to conclude that the stiffening is due to polymer rather than particle structuring.

During 900 sec waiting time, we collected viscoelastic modulus data at small (10%) strain amplitude (Figure 3.5c) and observed that the homopolymer recovers its modulus to the initial modulus value when it is at rest. Figure 3.5d shows that the stiffening behavior appears during the rest time of the 15 wt% composite. Moreover, the initial time sweep data (at 50% strain) shows that the modulus remains constant over time. We conjecture that deformation leads to self-strengthening of the system as the interphase evolves into a dense entangled layer as discussed in the following section. The stiffening mechanism, which occurs in a process of deformation followed by resting, was further verified by employing an intermediate strain amplitude (150%) on the 22 wt% composite

during its resting period as shown in Figure 3.8. We observed that composites stiffen less when the chain relaxation process is disrupted with the large deformation.

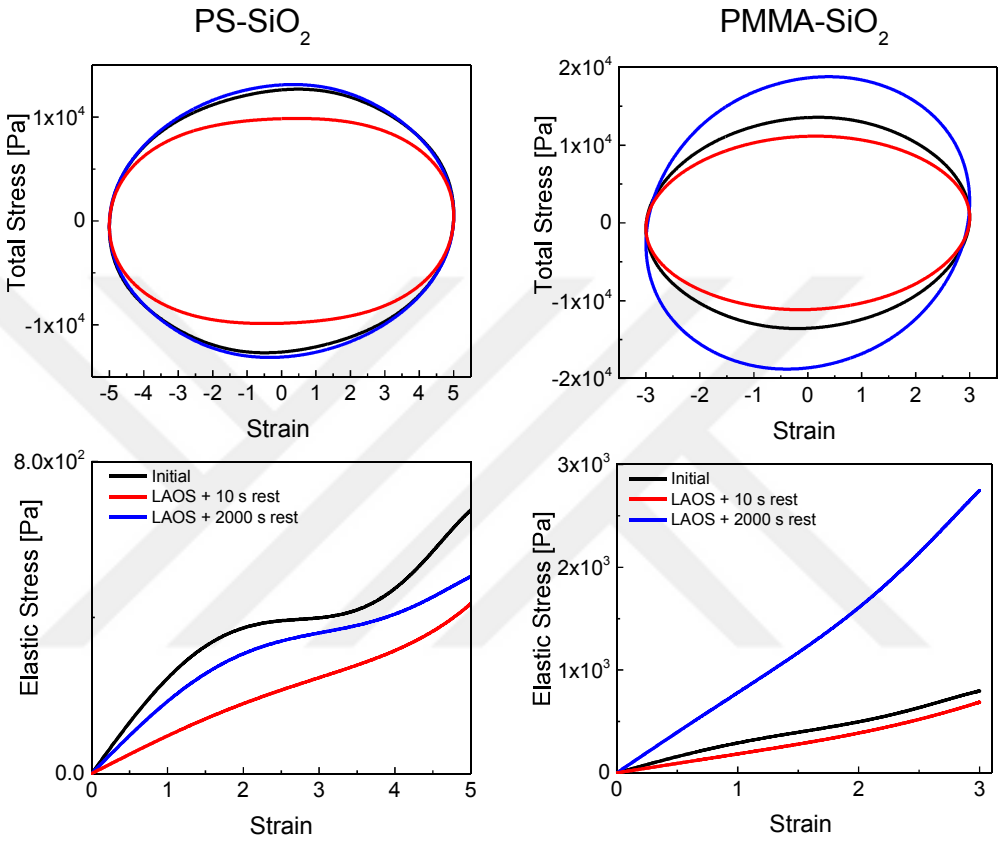

Figure 3. 6. Lissajous plots (total stress-strain) and elastic stress-strain curves for PMMA ($\overline{M}_w$: 36 kg/mol)-15 wt% silica (13 nm) and PS ($\overline{M}_w$: 52 kg/mol)-15 wt% silica (13 nm) composite at the initial stage and after 10 and 2000 sec waiting times measured at 210 ^{o}C.

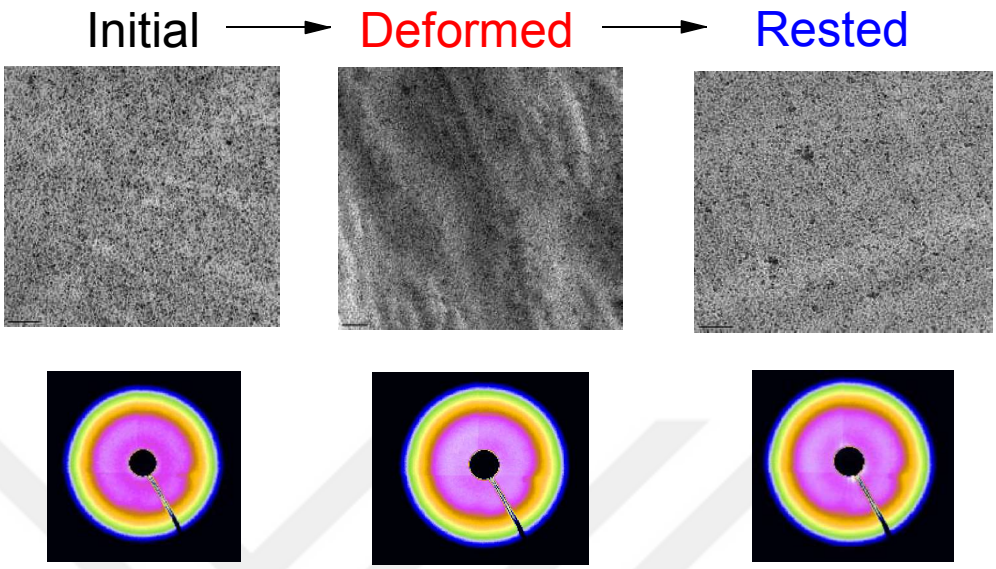

Figure 3. 7. TEM images and 2D SAXS patterns for PMMA ($\overline{M}_w$: 36 kg/mol)-15 wt% SiO_2 (13 nm) at the initial (undeformed) stage and after applying shear and resting in 10 sec (deformed) and 2000 sec (rested).

3.3.3. Chain conformation and molecular packing

To understand the effect of filler on polymer conformation, we have performed Small-Angle Neutron Scattering (SANS) and Fourier-transform infrared (FTIR) spectroscopy measurements on composites before and after deformation. Analysis of SANS data revealed no measurable change in the Gaussian conformation of chains when samples are deformed (Figure 3.9 and Appendix 2 Figure A2.4).

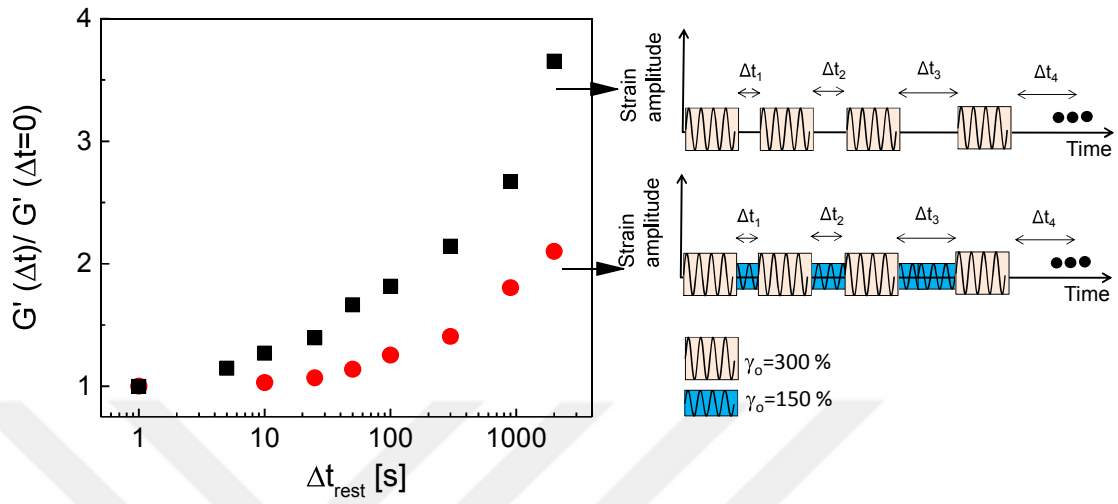

Figure 3. 8. Normalized modulus as a function of waiting time for PMMA-SiO_2 22 wt% composite with no strain and 150% strain applied during waiting times.

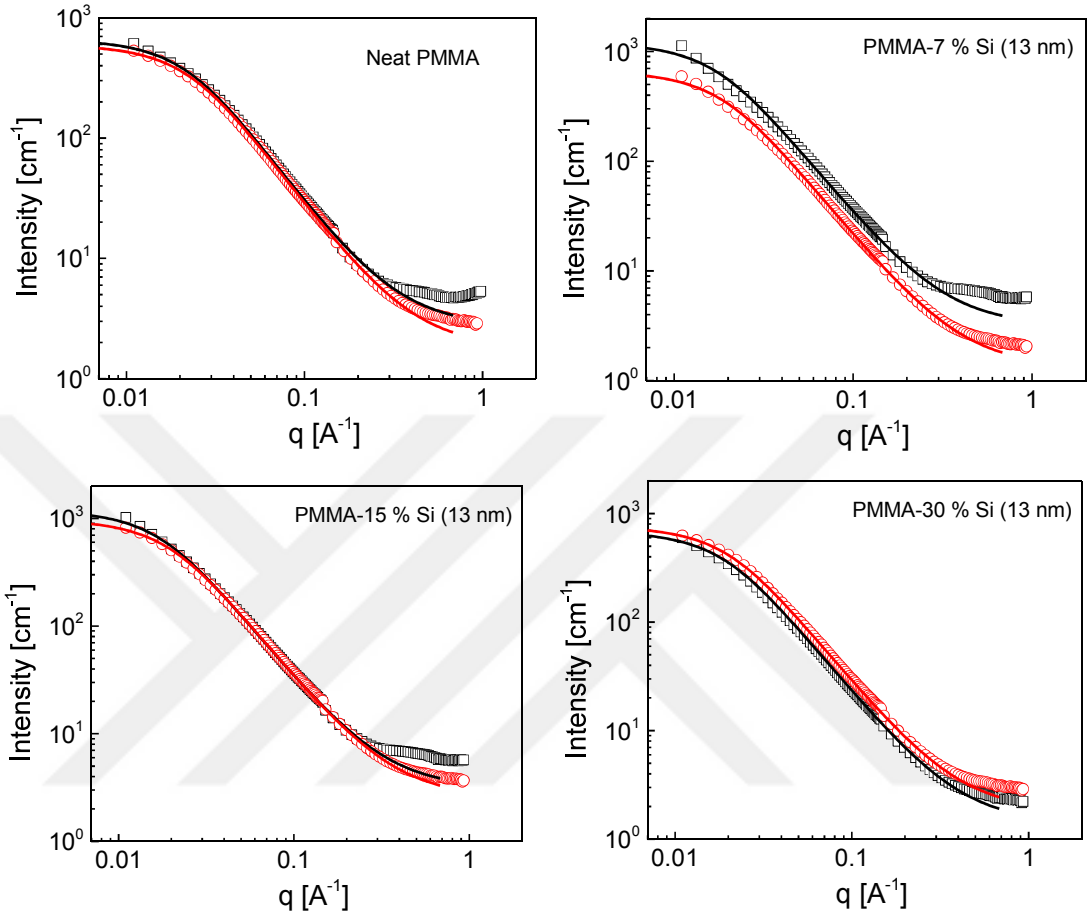

Figure 3. 9. SANS profiles of nanocomposites (13 nm silica) before (black) and after (red) deformation. Lines represent Debye fits. Error bars are smaller than the symbol sizes.

We performed FTIR experiments on undeformed/deformed composites, as IR-absorption has been used previously to confirm the closer packing of PMMA chains on particle surfaces at all trans (TT) conformations[91,92]. Thus, the appearance of TT at 860 cm^{-1} after particle addition refers to denser packing of PMMA on particles. Figure 3.10a presents the IR-absorption graphs of undeformed composites where the TT peak height

relative to the trans-gauche (TG) peak at 843 cm^{-1} increases with particle composition. Figure 3.10b shows that the molecular conformation of the homopolymer does not change with deformation. At 22 and 30 wt% loadings, the heights of the TT peaks relative to the TG peaks decrease after deformation. These results imply desorption of the adsorbed polymer segments on particle surfaces after deformation, which can occur through processes such as removal of the trains and increase of the ratio of loops and tails. For 15% loading samples, no significant change is observed, possibly due to lower interfacial density and a small amount of adsorbed polymer present in the sample. We hereby demonstrate that PMMA conformation enhances the strength of adsorption leading to formation of a dense layer on spherical nanoparticles and that large strain amplitudes are required to desorb them. Further, we suggest that the entanglement of free matrix chains with the surface-associated chains is enhanced under repeated cyclic deformations. This mechanism can be utilized in responsive composites to improve their mechanical adaptability under frequent mechanical loadings.

3.4. Chapter Conclusions

It is well accepted that strong interactions between polymer and fillers lead to individually dispersed nanoparticles. Observing the evolution of interphases in such attractive composites under deformation is critical to explore the adaptive mechanical behavior. The continuous process of "deformation and waiting" allows us to measure the mechanical response from adsorption and desorption of chains forming longer loops. During the resting time, more free chains entangle with these loops which create denser adsorbed polymer layers. Consequently, the composite having attractive interactions with

its fillers behaves like a stress sensor at surfaces during deformation and becomes more reinforced during resting. Softening response of a PS-SiO_2 (repulsive) composite system with its aggregated particles confirmed that the increase in elastic stresses in an attractive system depends on molecular conformation and interfacial chain density. Relaxation of chains in attractive interphases under large deformation presents an interfacially controlled strengthening mechanism. This dynamic mechanical reinforcement mechanism has practical implications for designing mechanically responsive composites.

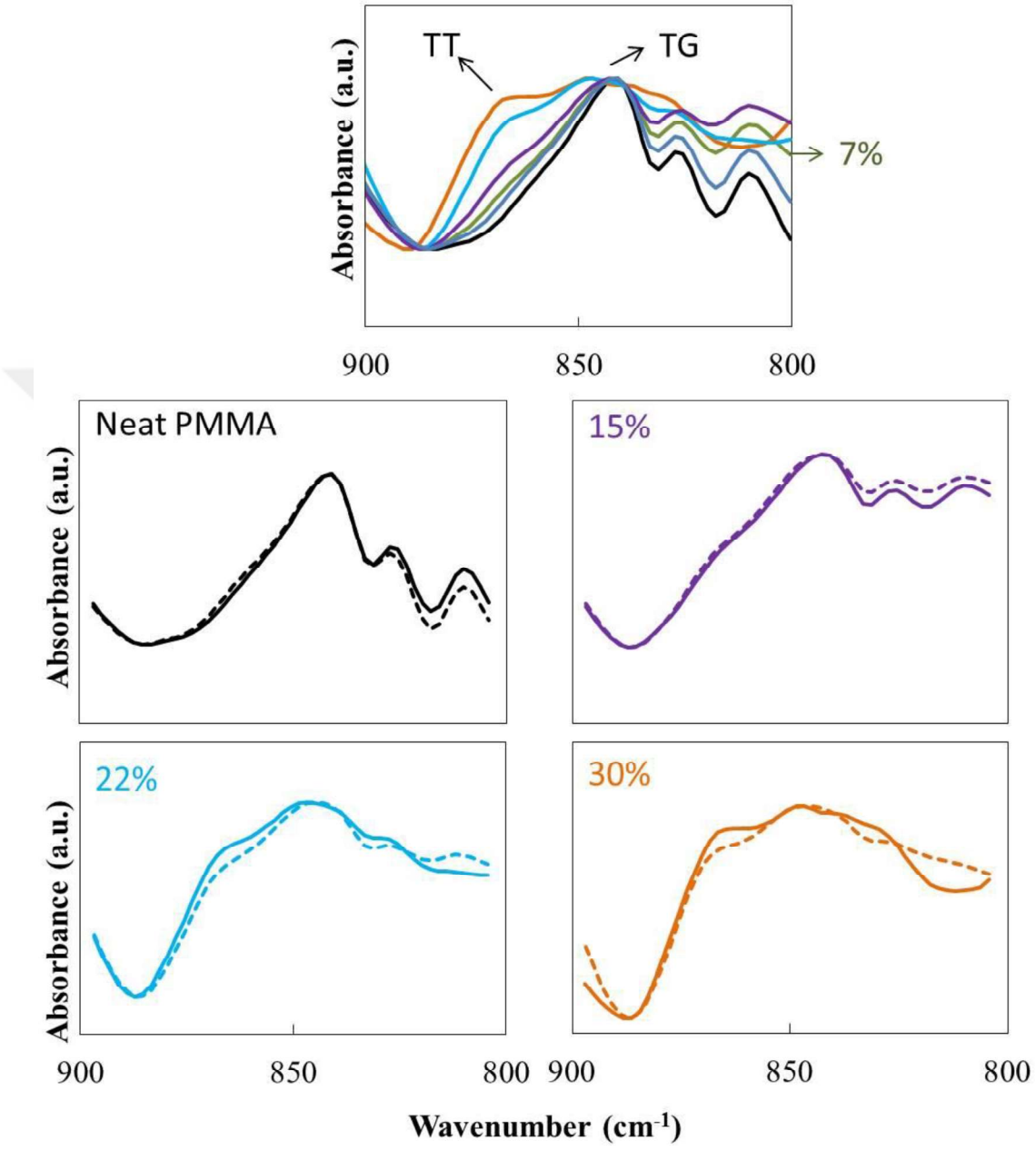

Figure 3. 10. FTIR absorption spectra of PMMA homopolymer and its nanocomposites with 15, 22 and 30 wt% silica loadings before deformation (top figure) and comparison of absorption spectra of undeformed (solid line) and deformed (dashed line) samples for each composition.

CHAPTER 4

TUNING MECHANICAL PROPERTIES OF POLYMER NANOCOMPOSITES WITH BIMODAL POLYMER BOUND LAYERS[3]

Chapter Summary

Mechanical properties of polymer nanocomposites can be enhanced by increasing nanoparticle loadings or by changing dispersion states. We demonstrate that a bound layer composed of short and long chains can be exploited to regulate the elastic modulus of bulk polymer nanocomposites within two orders of magnitude. The bound layer thickness on particles with high coverage of long chains is reduced with oscillatory deformation in a model attractive nanocomposite system. Reversibility of bound layer is, thus, possible for the short chains in the interphase. Compositional dynamic heterogeneity in the interphase has subsequent effects on the fragility of composites. With increasing amount of adsorbed long chains, fragility index systematically improves from moderate to high values. Our results suggest that the interphase layer between adsorbed chains and free matrix directly governs the reinforcement in poly(methyl methacrylate)-silica nanocomposites and can be dynamically altered under large shear.

[3] [Senses, E., & Akcora, P. (2014). Tuning mechanical properties of nanocomposites with bimodal polymer bound layers. *RSC Advances*, *4*(91), 49628-49634] Reproduced by permission of The Royal Society of Chemistry

.

4.1. Introduction

In this work, we alter the effective interphase with the adsorption of bimodal chains on nanoparticle surfaces and examine the role of adsorbed layer on mechanical properties of poly(methyl methacrylate)-silica (PMMA-SiO_2) nanocomposites. The interfacial layer effect has been studied recently on composites of polymer-grafted nanoparticles by Schadler et al.[93]. Well-dispersion was achieved in the allophobic dewetting regime with bimodal brushes. This finding then led them to study the role of matrix-brush entanglement on thermomechanical properties[93]. The problem of interfacial effect between grafted and free chains may look analogous to our work in which the interphases are between bare particles and adsorbed bimodal chains**.** In our system, however, bimodal chains are used to alter bound layer interactions between bare nanoparticles and the matrix which can tune the physical properties of composites and also can be prepared easily as opposed to grafting methods applied to nanoparticles[94]. Adsorption of homopolymers[12,22] or diblock copolymers[95] on bare has been attracting more attention as a new strategy to disperse nanoparticles effectively in polymer matrices for their practical processibility.

Here, we demonstrate that by adsorbing bimodal blends of very short (< entanglement molecular weight, M_e of PMMA: 12.5 kg/mol[96]) and long polymer chains (> M_e), the bound layer interactions can be physically modified from weak to strong within identical dispersion states. Additionally, we examine the mechanical consequences of bound layers at different compositions in attractive nanocomposites. Large amplitude oscillatory shear (LAOS) experiments on composites reveal that entanglements change

within a bound layer[22]. In our past work, we have shown that loops and tails in the interfacial layer of PMMA-SiO_2 nanocomposite can be dynamically altered in LAOS runs[22]. An interesting finding was that as sample rests between two deformation cycles, matrix chains entangled more densely with the adsorbed chains, and led to large increases in elastic modulus compared to the deformed unfilled polymer. This work now aims to reveal the effect of entanglements within this interphase by changing its composition on the mechanical and glassy properties of nanocomposites.

4.2. Experimental Section

4.2.1. Materials

PMMA's of different molecular weights were synthesized by ATRP polymerization using p-toluenesulfonyl chloride (TsCl) initiator, CuBr-$CuBr_2$ catalyst system with 2,2'-bipyridine in toluene at 70 ^oC. The reactions were complete within 24 hours. Colloidal SiO_2 nanoparticles (13 nm and 55 nm in diameter) in methyl ethyl ketone were supplied by Nissan Chemicals America and used as received. The specifications of our samples are listed in Table 3.1.

Table 4. 1. Specifications of nanoparticles adsorbed with varying polymer blend compositions.

molecular weight $\overline{M}_n$ **[kg/mol] (Dispersity ,** $Đ$**)**		**volume fraction of long chains in blends** Φ_L	**SiO_2** **Size [nm]**	**wt %**
96 (1.12)	4.3 (1.1)	1, 0.8, 0.5, 0.2, 0	13, 55	15
68 (1.05)	2.6 (1.1)	1, 0.95, 0.85, 0.7, 0.3, 0	55	30
12 (1.15)	2.6 (1.1)	1, 0.8, 0.5, 0.2, 0	55	30

4.2.2. Adsorbed bimodal chains on nanoparticles

Bimodal polymer blend solutions were prepared in acetonitrile (at 40 mg/mL) with varying long chain compositions. Blend solutions were mixed with nanoparticles at 30 wt% using a bath sonicator for 30 min. Solutions were stirred vigorously for 2 h and were immediately poured into Teflon dishes and evaporated overnight. Films were then annealed under vacuum at 150 ^{o}C for 3 days and at 180 ^{o}C for 2 h to ensure complete removal of solvent. Nanocomposites were then re-dissolved in acetonitrile and nanoparticles with bound polymer were recollected by centrifugation at 11,000 rpm for 5 min. Washing process was repeated 3 times to ensure all unbound chains were removed.

4.2.3. Bound layer characterization

DLS measurements were carried out with a Zetasizer NanoS (Malvern Instruments) at particle concentration of ~1 mg/mL in acetonitrile to measure the hydrodynamic thickness of adsorbed layer. Measurement duration was 11 s, and data were averaged over 10 runs. TGA measurements were performed on a Q50 TGA (TA Instruments) to determine the mass amount of adsorbed polymer. Measurements were performed under a constant flow of nitrogen of 20 mL/min at a heating rate of 20 ^{o}C/min, starting from 40 ^{o}C up to 580 ^{o}C, while pausing isothermally at 150 ^{o}C for 20 min to ensure samples were free of solvent and then finally incubated at 580 ^{o}C for 20 min.

4.2.4. Fourier Transform Infra-Red characterization

Dry samples were mixed with KBr powder and compression molded to obtain transparent uniform films. Absorption spectra were obtained using a Tensor 27FTIR

spectrometer (Bruker Optics) in the range of 400–4000 cm^{-1} with 64 scans of 4 cm^{-1} resolution.

4.2.5. Nanocomposite preparation

Polymer bound particles were mixed with PMMA (M_n: 28 kg/mol, ~~$Đ$~~: 1.15) and solution cast to form bulk films. Films were then annealed for 3 days at 150 ^oC and 2 h at 180 ^oC under vacuum to remove any residual solvent.

4.2.6. Nanoparticle structural characterization

Films were microtomed into ~100 nm slices with a diamond knife at room temperature and examined by transmission electron microscopy (FEI CM20 FE S/TEM) at 200 keV. SAXS measurements were performed at Beamline X27C at the National Synchrotron Light Source (NSLS), Brookhaven National Laboratory. Air background subtracted data were fit to the unified equation; $I(q)=\sum_i A_i \exp[-q^2 R_{gi}^2/3]+B_i[((\mathrm{erf}(\frac{qR_{gi}}{\sqrt{6}}))^3)/(q)]^p{}_i$, where R_g is the radius of gyration, and p is the fractal dimension of the scattering objects and A_i and B_i are constants for the i^{th} structural level. One level fit was sufficient to describe the patterns.

4.2.7. Rheological characterization

Linear and non-linear tests were performed on a strain-controlled ARES-G2 (TA Instruments) with 8-mm stainless-steel parallel plate fixtures. Composite samples were molded with a vacuum assisted compression molder at 180 ^oC for 10 min and then annealed at 130 ^oC for 12 h prior to the measurements. Experiments were performed at 210 ^oC after 10 min equilibration time. LAOS tests were performed at a fixed frequency

of 1 rad/sec and at strain amplitude 300%. Measurement time was 300 s and data was collected at 300 Hz sampling frequency. Sheared samples were quenched below T_g of PMMA in ~1 min while the axial force is controlled within ±1 N to prevent thermal strain. Data was analyzed by using MITLaos software as previously reported[97].

4.2.8. Glass transition and dynamic fragility

Fragility and glass transition temperatures on composite films were determined by using Q100 DSC (TA Instruments). The samples were first heated to 175 ^oC for 5 min and then cooled down to 30 ^oC at different cooling rates (Q) ranging from 0.2 to 30 ^oC/min followed by heating to 175 ^oC by standard heating rate of 10 ^oC/min. The glass transition temperatures (T_g) were determined from the inflection point on the heating curves following the standard cooling rate Q_{std} = 20 ^oC/min. The limiting fictive temperatures, T_f, were obtained from each heating scan by using the instrument software (Q-Advantage). The dynamic fragility index, *m*, was determined from the relationship, $\ln(Q/Q_{std}) = m - mT_{f,std} / T_f$, where $T_{f,std}$ is the standard fictive temperature for Q_{std}[98].

4.3. Results and Discussion

4.3.1. Bimodal chain adsorption on nanoparticles

We first studied the dispersion of bare nanoparticles in homopolymer blend matrices. Hydrogen bonding between oxygen atoms on PMMA and hydroxyl groups on SiO_2 favors the physical adsorption of polymer to nanoparticle surfaces. Polymer-solvent interactions govern the adsorption process. For example, samples prepared in MEK or THF, which are good solvents for PMMA, exhibited poor dispersion since solvent can

displace chains on nanoparticles and impede the adsorption of chains. We further tested this by preparing composites with THF solvent (good solvent for PMMA).

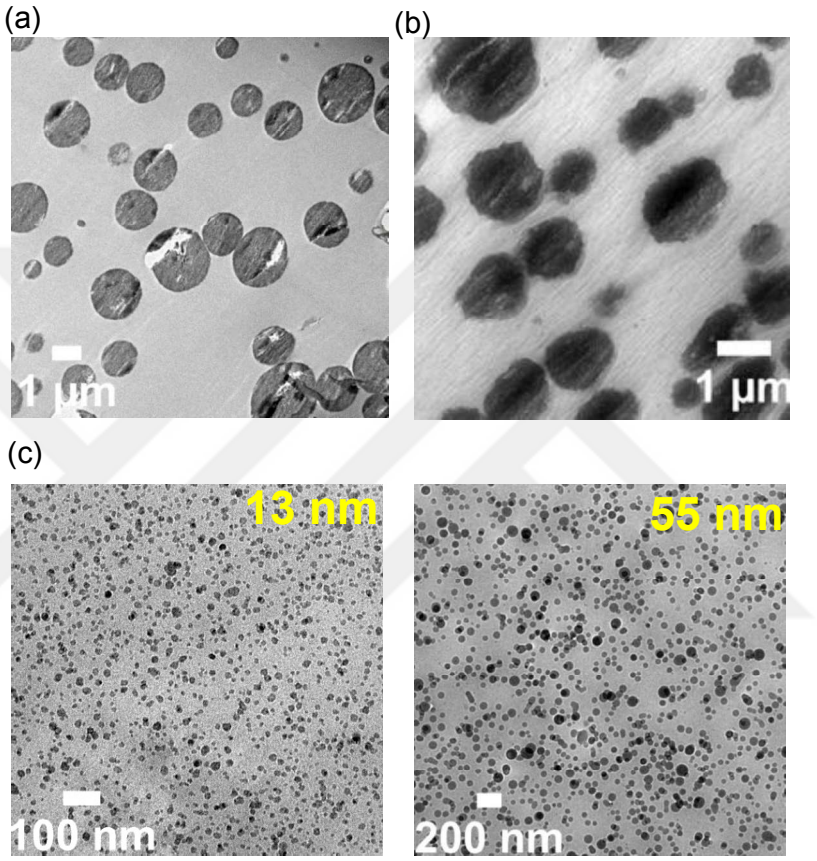

Figure 4. 1. TEM images of **(a)** PMMA-SiO_2 (13 nm) and **(b)** PS-SiO_2 (13 nm) composites prepared by solution casting from THF. PMMA matrix consists of 50:50 blends of 4.3 kg/mol and 96 kg/mol chains. PS matrix consists of 50:50 blends of 5 kg/mol and 100 kg/mol chains. **(c)** Individual dispersion of SiO2 nanoparticles (13 nm

and 55 nm) in PMMA (50:50 blends of 4.3 and 96 kg/mol chains) cast from acetonitrile. Particle loadings are 15 wt% in all samples.

Figure 4.1a shows that 13 nm particles aggregate to form micron size clusters with sharp interfaces compared to the individual dispersion achieved with acetonitrile (θ-solvent) (Figure 4.1c). Strong interaction between THF and PMMA makes the adsorption unfavorable in solution, and the particle dispersion becomes similar to that for a repulsive system, as in PS-SiO_2 in which identical micron-size clusters formed in the matrix (Figure 4.1c). Another reason to choose a θ-solvent is that in good solvents the chains are swollen ($R_g \sim M^{\alpha}$ with $\alpha = 0.8$) due to excluded volume effect while in melt and θ-solvent the chains assume ideal Gaussian conformation ($\alpha = 0.5$). Hence, using θ-solvent allows keeping ideal conformation of chains from casting stage to annealing and avoids possible interfacial stress due to entropic contraction.

We thus used acetonitrile, a θ-solvent for PMMA, in preparation of our composites as chains can adopt their ideal chain conformations in both solution and melt states[99]. We mixed SiO_2 nanoparticles in solutions of blend homopolymers (96 and 4.3 kg/mol PMMA). TEMs in Figures 4.2a-b show individual dispersion of nanoparticles (13 nm and 55 nm in diameter, at 15 wt% loading) in 96-4.3 kg/mol blend matrix (50/50 vol/vol %). Figure 4.2c displays SAXS patterns for 13 nm nanoparticles in matrices with different blend compositions. Individually dispersed nanoparticles of ~7 nm radius were obtained from low q-fitting, governed by the Guinier equation[100]: $I(q)=I_0\exp[-(qR_g)^2/3]$. The

scaling in the Porod regime, $I(q) \propto q^{-4}$, suggests particles are dispersed with sharp surfaces in all samples.

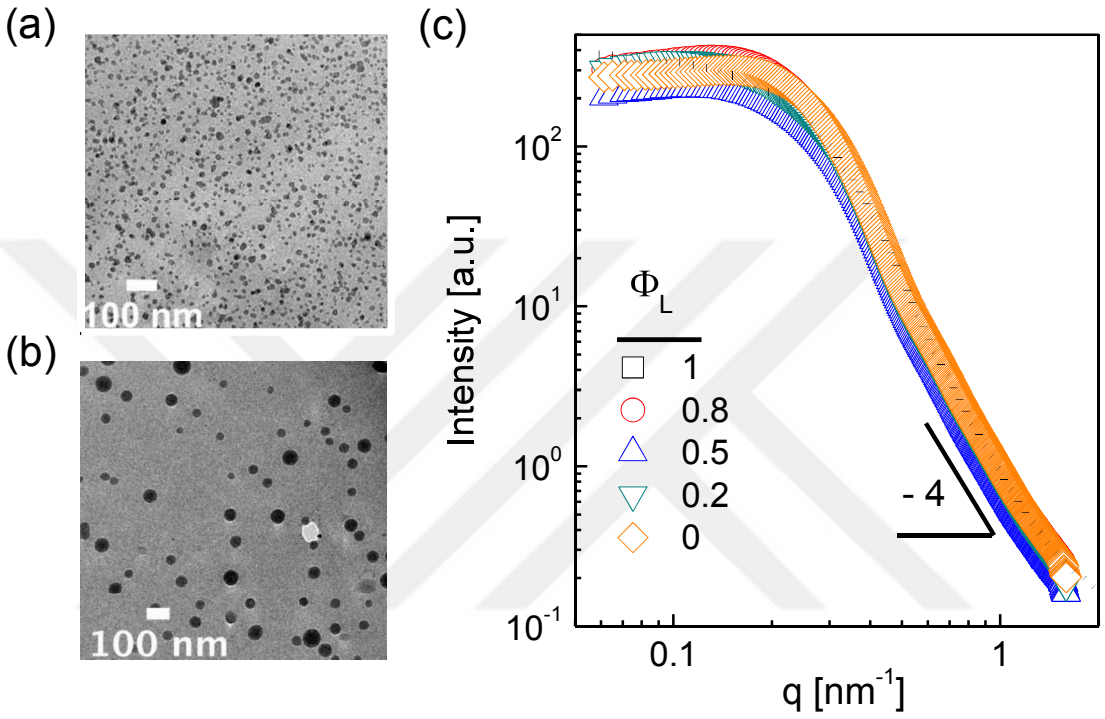

Figure 4. 2. TEM images for **(a)** 13 nm and **(b)** 55 nm SiO_2 nanoparticles in matrix composed of 96 and 4.3 kg/mol PMMA homopolymers at 50/50 vol%. Images at low magnifications are presented in Figure S2. **(c)** SAXS patterns for nanocomposites of different matrix compositions. Φ_L is the volume fraction of long chains in blend matrix. Dashed line is a Unified fit for a single level structure. Particle loading is 15 wt% in all composites.

Next, we dispersed bare particles in 68 kg/mol and 2.6 kg/mol PMMA homopolymer mixtures for bimodal chain adsorption (see experimental for procedure). We used 55 nm

nanoparticles in our composites because the amount of adsorbed polymer on 55 nm particles is higher due to less curvature effect. Nanoparticles extracted from composites were analyzed in DLS and TGA (data shown in Figure 4.3a-b) following the reported protocol[12]. It is evident that hydrodynamic sizes of polymer bound nanoparticles (h) are larger than bound polymer thicknesses (t), and both parameters systematically increase with the fraction of long chains (Figure 4.3c). These results indicate that the composition of the bound layer changes by varying the fractions of long and short chains in the blend matrix.

Differences in desorption probabilities drives the well-known competitive adsorption of chains with different lengths on flat surfaces. It was shown by Dijt et al.[101] that kinetics of adsorption is primarily determined by transport of chains from dilute solution to the surface. Short chains that are adsorbed first are replaced by long chains eventually[102,103]. These studies on the preferential adsorption or exchange of long and short chains are in dilute solution limit. This mechanism does not apply in our system because particles are adsorbed in concentrated polymer solution. Granick et al.[104] showed that strongly adsorbing chains on surface can sterically pin weakly adsorbed ones, resulting in their extended life-time on surface. In the case of bimodal chain adsorption, weakly adsorbed short chains can be pinned by the strongly adsorbed long polymers. This may create an additional entropic barrier to prevent desorption of short chains.

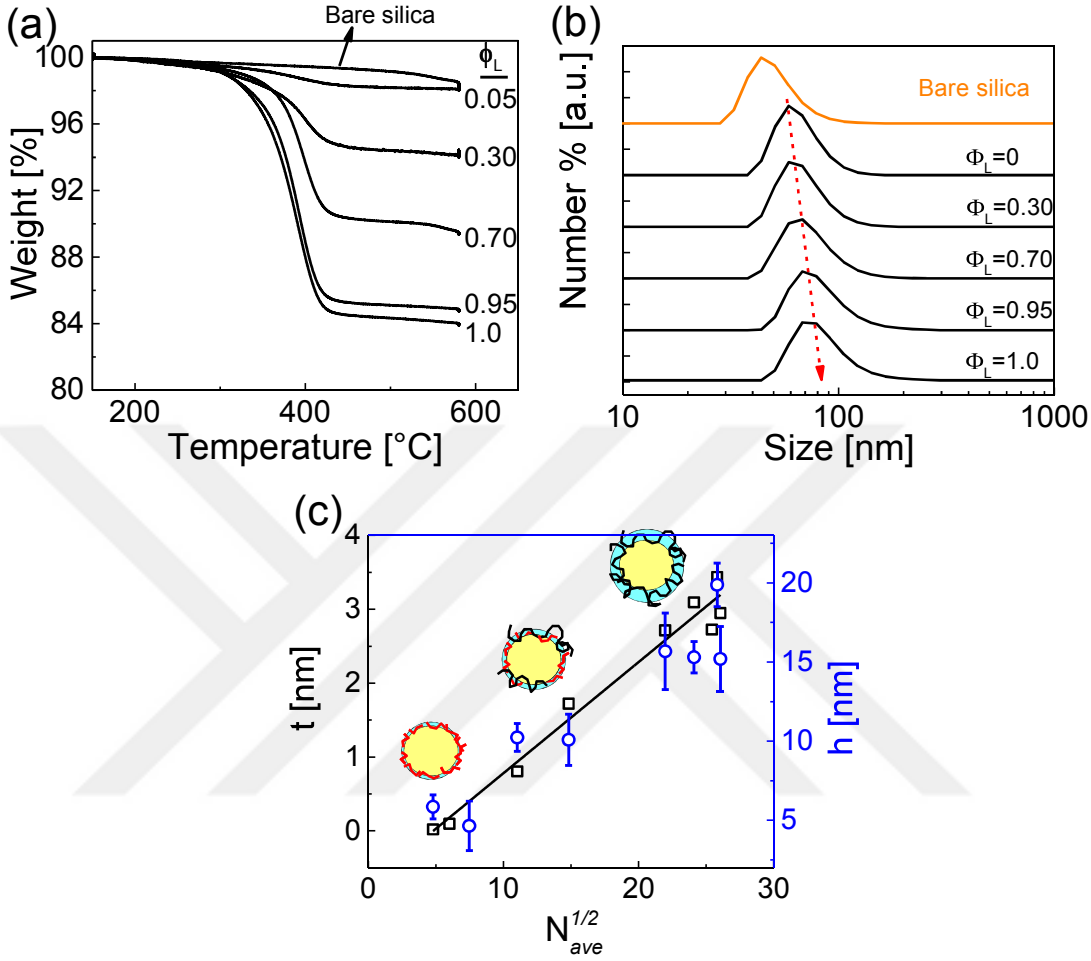

Figure 4. 3. (a) Hydrodynamic size distributions of 68-2.6 kg/mol PMMA blend adsorbed on SiO_2 nanoparticles (55 nm) as a function of Φ_L. **(b)** Weight loss curves of corresponding particles are measured in TGA. **(c)** Bound layer thicknesses determined from TGA (t) (black squares) and DLS (h) (blue circles) as a function of $N_{ave}^{1/2}$. Cartoons represent the bound layer thickness variation with increasing coverage of long chains on particles.

It is also known that conformation of adsorbed chains from semi-dilute concentration or melt is the same as in solution[105]. Thus, the scaling for bound layers with the chain length, $N^{1/2}C^{7/8}$, at semi-dilute concentration is a reasonable argument and can be applied for the adsorbed amount of bimodal chains from their close-to semi-dilute concentration solutions. Virgiliis et al.[106] predicted that the amount of polymer adsorbed from melt scales with $N^{1/2}$, which agrees with the theoretical predictions by Fleer[107]. In our system with bimodal bound layer, thickness of bound layer also varies linearly with $N_{ave}^{1/2}$ as shown in Figure 2. N_{ave} is defined as $N_{ave} = \Phi_L N_L + (1-\Phi_L) N_S$, where Φ_L is the volume fraction of long chains (68 kg/mol), N_L and N_S is the degree of polymerization for long chains and short chains (2.6 kg/mol), respectively.

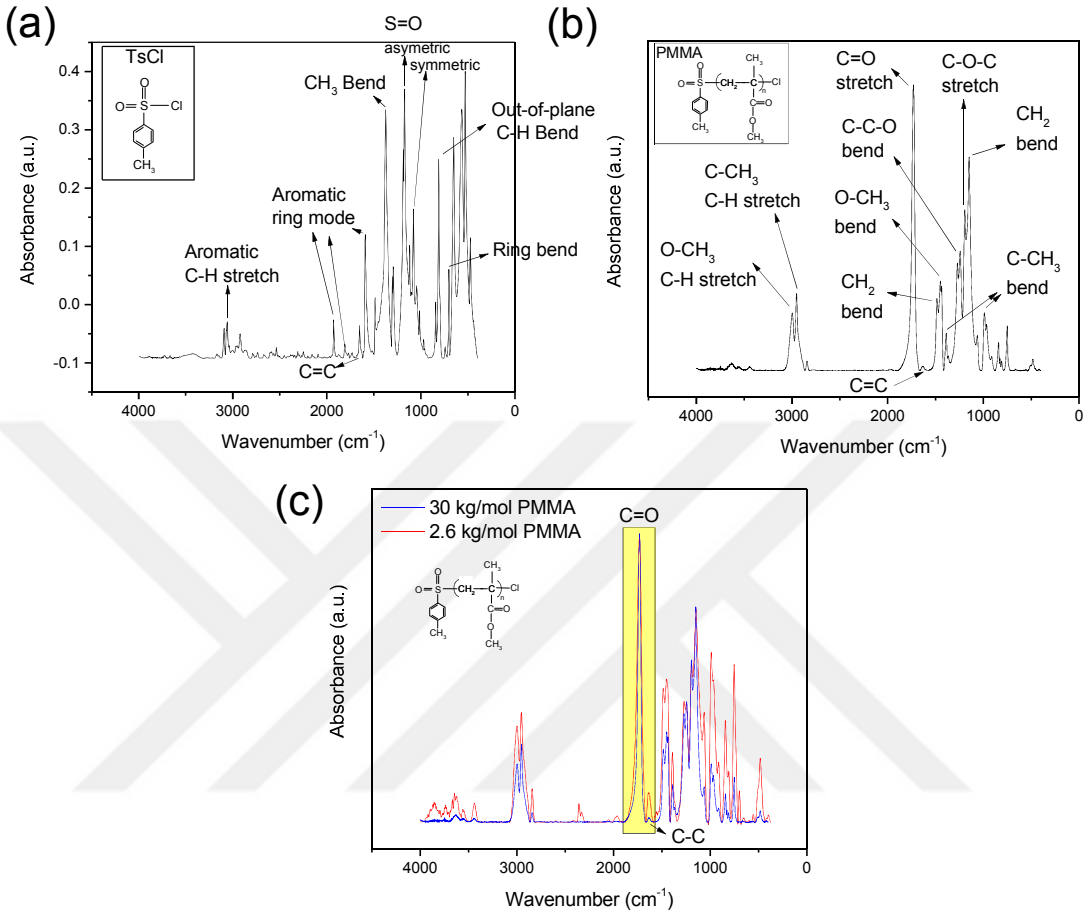

Figure 4. 4. FTIR spectra for **(a)** TsCl (chain end group) and **(b)** PMMA (30 kg/mol) synthesized using TsCl. **(c)** Comparison of short (2.6 kg/mol) and long (30 kg/mol) PMMA spectra showing the enhanced C=C peak at 1652 cm^{-1} for short chains.

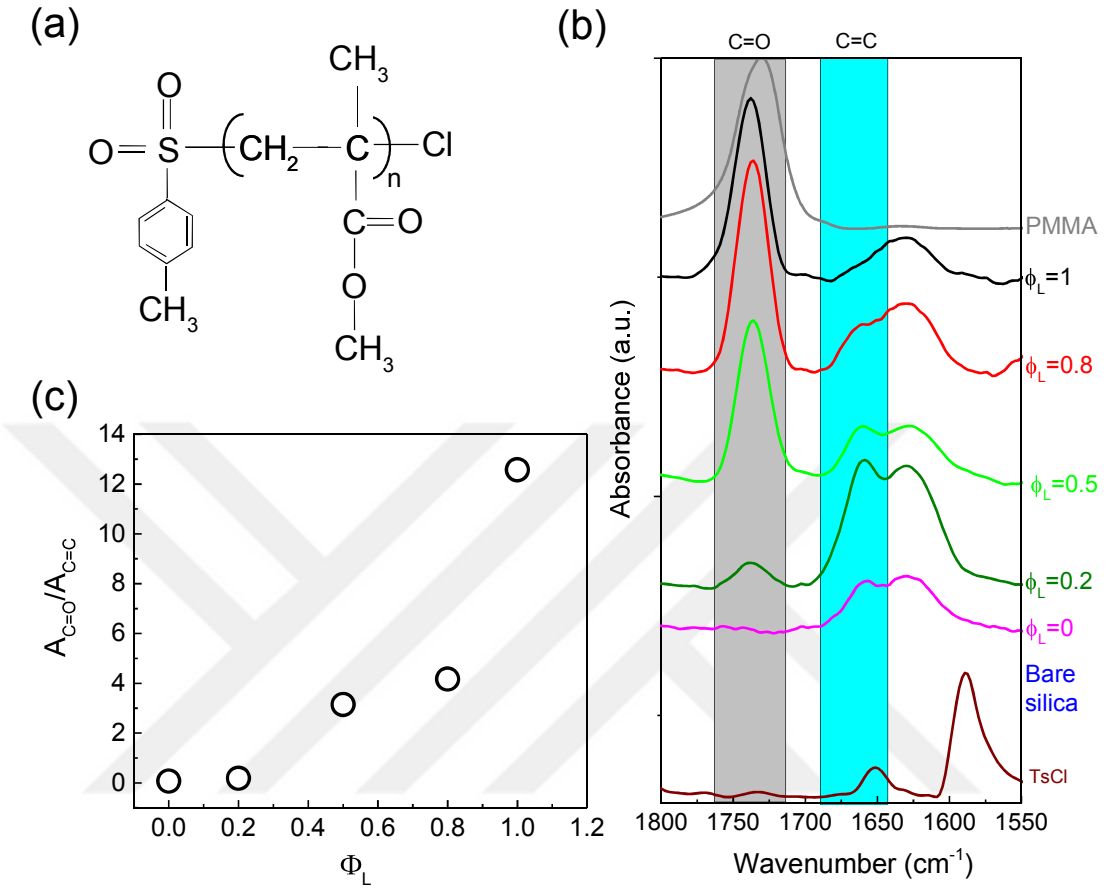

Figure 4. 5. (a) The structure of the PMMA with its end groups are shown in the inset. **(b)** FTIR spectra for bare and adsorbing bimodal PMMA chains (2.6 kg/mol and 150 kg/mol) 55 nm SiO_2 nanoparticles at different long chain composition. **(c)** Ratio of peak areas corresponding to C=O (of monomer) and C=C (of end group).

While previous studies suggest that the adsorbed polymer composition should assume the blend concentration in solution and melt matrix, and our DLS and TGA characterization well-agree with the theoretical predictions, it is important to verify the existence and fraction of the short chains after annealing and washing steps. It is,

however, extremely challenging to directly measure the bound layer composition. Various techniques such as positron annihilation spectroscopy[13], neutron spin-echo spectroscopy[108], NMR[109,110] and small-angle neutron scattering[111] have been used to determine the thickness, conformation and dynamics of the adsorbed polymer. Here, we took advantage of both the large asymmetry of adsorbed chain lengths and the contribution of end-groups (structure shown in Figure 4.4a) to evaluate the bound layer composition. Figure 4.4b-c shows the FTIR peaks for neat 30 kg/mol PMMA and comparison of short and long chains. Figure 4.5 presents the IR spectra of bare components and the bimodal PMMA adsorbed nanoparticles in the range of 1800-1550 cm^{-1} involving the C=O region (1740 cm^{-1}) of the PMMA and C=C peak (1652 cm^{-1}) of TsCl. As the number of chain ends is inversely proportional to the chain length (1/N), C=O peak dominates over C=C peak for all-long-chain adsorbed particles ($\Phi_L = 1$) while C=C/C=O ratio progressively increases with increasing short chain concentration. This is further quantified by the areal fractions of C=O and C=C regions (Figure 4.5c). It is clear from the FTIR spectra and the DLS/TGA analysis that the short chains contribution increases monotonically with increasing short chain ratio on bimodal matrix from which the chains are adsorbed on nanoparticles.

4.3.2. Effects of bimodal adsorbed chains on linear viscoelastic properties of nanocomposites

The main focus of our work is to examine mechanical consequences of bimodal bound layers on nanoparticles in melts. Nanoparticles adsorbed with bimodal chains of 68 and 2.6 kg/mol PMMA homopolymers (samples in Figure 4.2) are redispersed in 28 kg/mol

PMMA matrix. Matrix molecular weight is chosen carefully to be 28 kg/mol above entanglement molecular weight in order to observe the changes of relaxation times during deformation[22]. Dispersion state of nanoparticles adsorbed with bimodal chains in 28 kg/mol PMMA matrix is shown in Figure 4.2. It is expected that PMMA of 2.6 kg/mol is unable to form loops or entangle with matrix chains near the surface. Thus, changing the fraction of long adsorbed chains can control interfacial entanglement density, and hence rheological properties in attractive nanocomposites. Figure 3.6 shows the elastic modulus (G′), loss modulus (G") and tanδ over four decades of angular frequencies for various bound layer compositions. The low frequency regime of G′ clearly shows changes in equilibrium relaxation behavior upon increasing the loop concentration on filler surfaces. Elastic modulus is modified by two orders of magnitude with the increased amount of long chains in bound layers within the same dispersion state of fillers. This is clearly different than conventional nanocomposite studies where the reinforcement is usually increased by increasing particle loading[112]. Our study further reveals the effect of interfacial entanglements on tuning the rheological properties within the same particle dispersion and concentration.

Well dispersion of nanoparticles allowed us to further analyze our linear data in terms of viscosity and compare with the theoretical predictions. We obtained the zero-shear viscosities η_0 by fitting the complex viscosity data to three parameter Cross model $\frac{\eta^* - \eta_0}{\eta_0} = \frac{1}{1 + K\omega^m}$. We first obtained the parameters for the particle-free matrix as $\eta_{0,free} = 5162$ Pa.s , $K_{free} = 0.017$ and $m_{free} = 0.72$. Viscosity parameters for

nanocomposite samples were obtained by superposing the contributions of free matrix chains and interphase. We kept the matrix contribution the same since the particle loading is constant thus its hydrodynamic effect would be the same.; and only allow interphase parameters to vary in the composite viscosity fitting for $\eta^* = \eta^*_{free} + \eta^*_{interphase}$. Because polymer type is the same at the interphase and free matrix, we kept the exponent the same as for free chains ($m_{free} = m_{interphase} = 0.72$). We then obtained the parameters $K_{interphase}$ and $\eta_{0,interphase}$ for each bound layer composition, Φ_L. Contributions from free and interphase polymer and their superposition is illustrated on composite sample with $\Phi_L = 1$ in Figure 4.7a. The fittings for all composites are shown in Figure 4.7b. Fitting parameters for the interphase contributions in each sample are given in Appendix 3 Table A3.1. The overall zero shear viscosity then becomes $\eta_0 = \eta_{0,free} + \eta_{0,interphase}$.

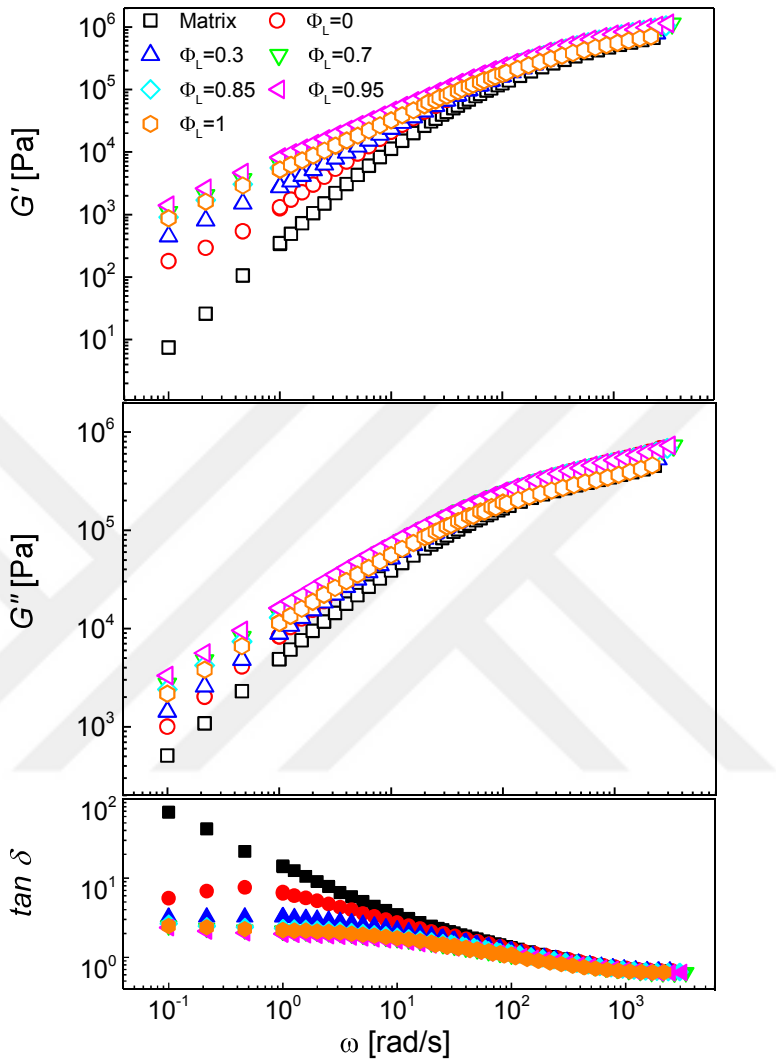

Figure 4. 6. Linear elastic and loss moduli, and loss tangent of the nanocomposites with particles adsorbed with a mixture of 68 kg/mol and 2.6 kg/mol PMMA in 28 kg/mol PMMA matrix. Particle volume fraction, φ_{part} = 0.17 and T_{ref} = 210 ^{o}C.

The reinforcement factors obtained at different Φ_L (i.e. log ($\eta_0(\Phi_L)$ / $\eta_{0,Matrix}$) are then plotted against the hydrodynamic size of the particles (h) (Figure 4.7c). Linear

dependence was extrapolated to h = 0 to obtain the reinforcement of well-dispersed particles in the absence of adsorbed layer (forming a non-sticky and well-dispersed particle case). The extrapolated value, 1.6, agrees reasonably well with the Guth prediction[113] ($\eta/\eta_{Matrix} = 1+2.5\varphi+14.1\varphi^2 = 1.84$ with $\varphi = 0.17$ in our case) in which the reinforcement is due to hydrodynamic contribution at high loadings. This result suggests that the viscosity increase in attractive nanocomposites can be effectively altered with the interfacial entanglements. To verify that reinforcement is a result of entanglements within the bound layer, we prepared a composite bound with 12 and 2.6 kg/mol chains at the same particle loading. Figure A3.1 (Appendix 3) shows no such reinforcement of this composite because interfacial entanglements are less effective with 12 kg/mol chains ($<M_e$).

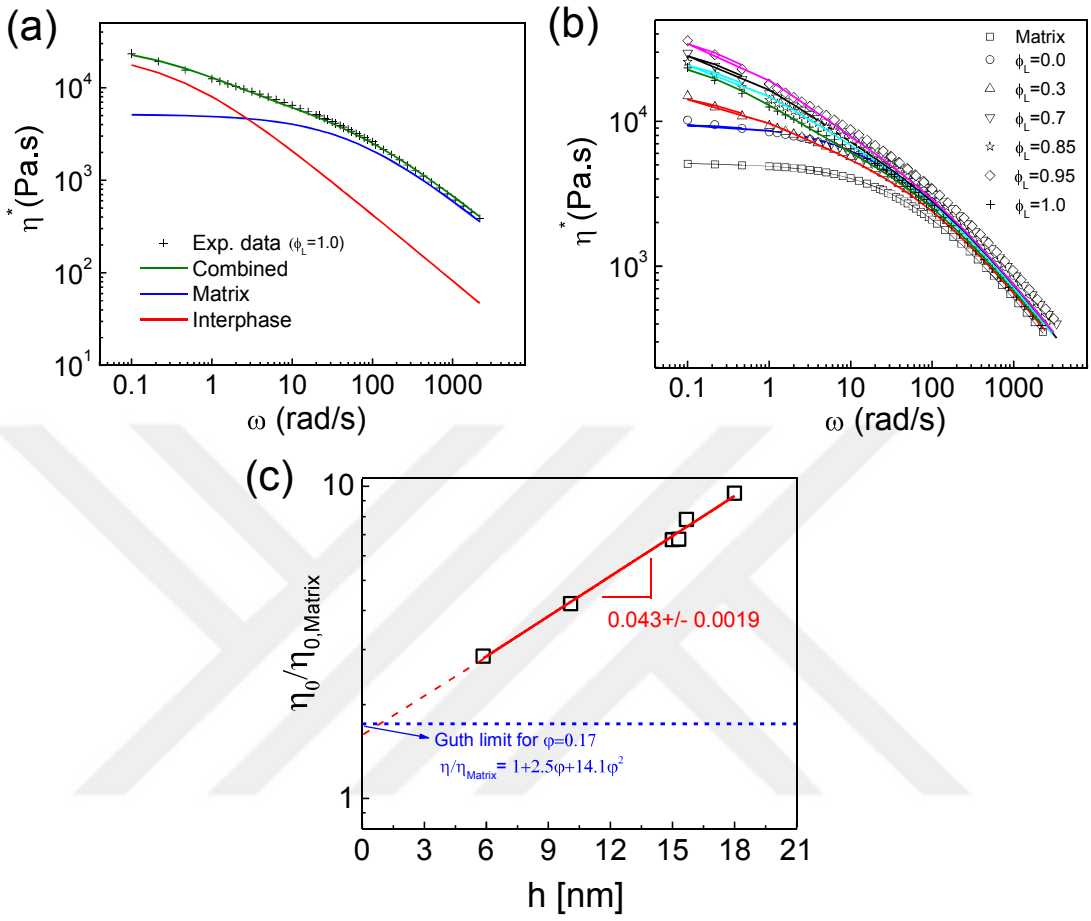

Figure 4. 7. (a) Complex viscosity response of composite (30 wt%) obtained from linear viscoelastic results shown in Figure 3.6 and corresponding model fit. Lines are free and interphase polymer contributions to the composite viscosity. **(b)** Model fittings for all the composites and the matrix. **(c)** Relative zero-shear viscosities as a function of hydrodynamic size of the particles. Flat line is the Guth prediction for spherical particles at high loadings. Particle loading is 30 wt% in all composites.

4.3.2. Effects of bimodal adsorbed chains on large amplitude shear response of nanocomposites

We next investigated the large shear response. In our previous work, we showed in PMMA-SiO_2 nanocomposite system that entanglement density around fillers can be altered with application of large amplitude oscillatory shear[22]. When the recovery of polymer modulus was monitored at rest, it was seen that composite stiffened after applying large strains, while the homopolymer recovered its initial modulus. During large-amplitude oscillatory deformations, chains can be desorbed and readsorbed, and the loop concentration may increase, which can lead to a self-stiffening behavior after shear due to increased entanglement density at the interphase. Correspondingly, such attractive systems can display unusual mechanical responses if the entanglement density of the interfacial layer is altered in a controlled fashion. Here, we further substantiate the origin of the self-stiffening of attractive composites by only changing the concentration of the loops using bimodal adsorbed chains. We apply similar deformation protocol[22] (see experimental) to our composites and expect to see stiffening due to interphase effect formed by adsorbed bimodal chains. Samples were deformed for 300 sec and then immediately quenched below T_g. Stress-response averaged from the last 5 cycles were analyzed. Stress-strain curves (Lissajous plots) for the matrix and composites (Figure 4.8a) present strengthening in non-linear regime. Total response is decomposed into its elastic and viscous components. Figure 4.8b shows the intra-cycle elastic stress-strain behavior of composites. It is evident that the average stress increases with the amount of long chains in the bound layer. Non-linear strain-stiffening[97], $G_L^{'}/G_S^{'}$,determined from

the ratio of the modulus in the limit of zero strain, $G_S' = \lim_{\gamma \to 0} (d\sigma/d\gamma)$, and large-strain γ_0, $G_L' = \sigma(\gamma_0)/\gamma_0$, shows a strong dependence on the composition of the bound layer (Figure 4.8c). Strain stiffening at large strain is due to stretching of the chains[21], which is governed by the entanglements at the interphase as schematically represented in Figure 4.8d.

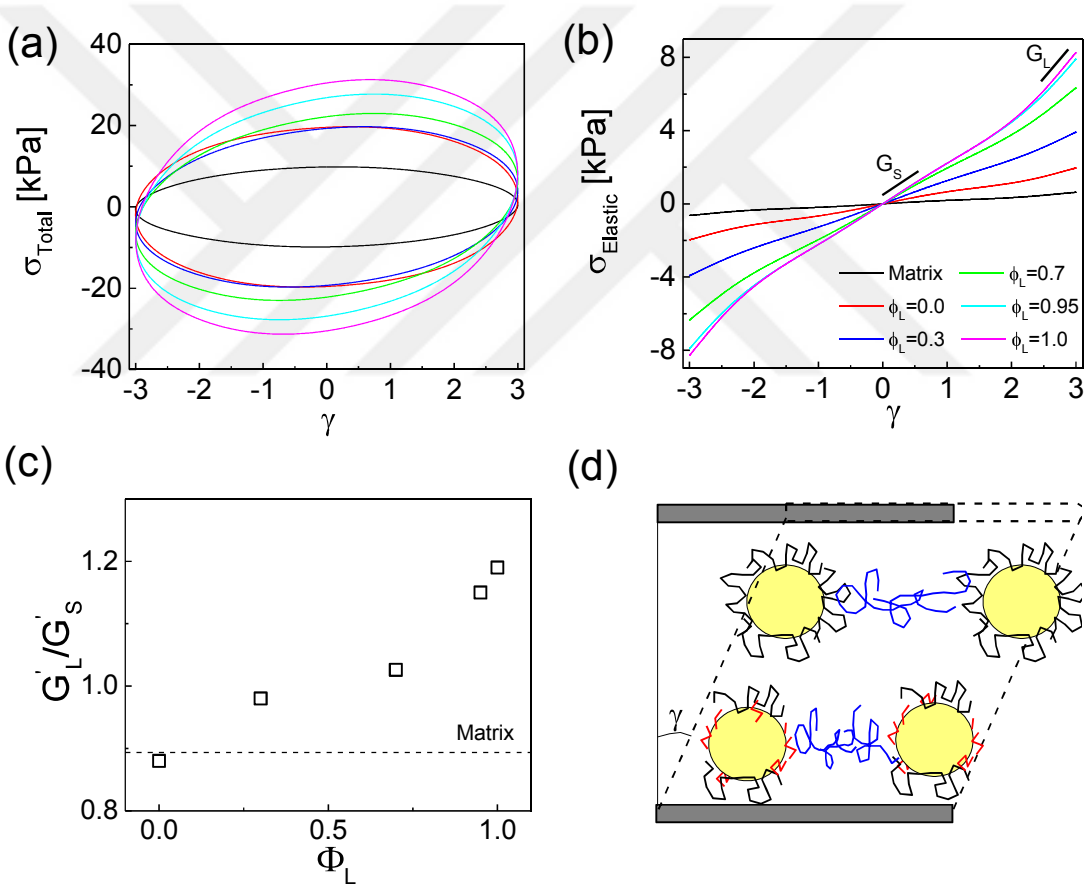

Figure 4. 8. (a) Total stress-strain curves (Lissajous plots) for 28 kg/mol PMMA homopolymer and its composites containing SiO_2 nanoparticles (at 30 wt%) adsorbed

with a mixture of 68 and 2.6 kg/mol PMMA at varying compositions. LAOS tests were performed at T = 210 ^{o}C, with γ_0 = 3 and ω = 1 rad/sec. **(b)** Corresponding decomposed elastic stress-strain behavior of nanocomposites. Slopes presented are the moduli at the limit of zero-strain (G_S') and maximum-strain (G_L'). **(c)** Strain-stiffening (G_L' / G_S') as a function of Φ_L. **(d)** Schematic representation of chains stretching under large shear at different entanglement levels.

The entropic barrier for desorption of short chains can be overcome by large shear. By distorting the conformation of the long chains on surface, this barrier is reduced and desorption/readsorption can be facilitated by large shear. To examine the deformation effect on bound layer thickness, samples deformed at large strains were quenched below T_g, and particles were recollected. Figure 4.9 compares the bound layer thicknesses before and after deformation. TGA results indicate that the bound layer thickness is reduced at high coverage of long chains after deformation which suggests that number of loops increases with shear and enables the denser entanglements at interphases, resulting in the stiffening observed under shear. The bound layer thickness remains nearly the same with small fractions of short chains which may be readsorbed on surfaces easily during and after deformation. This result reveals that bound layer of short chains is more likely to be reversible compared to the readsorption of long chains.

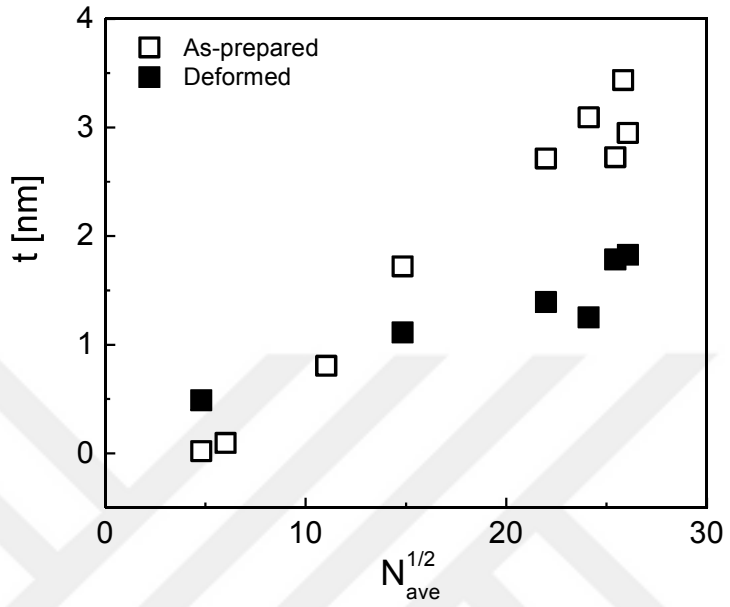

Figure 4. 9. Bound layer thicknesses (t) determined from TGA as a function of $N_{ave}^{1/2}$ before (open symbols) and after deformation (filled symbols).

4.3.3. Effect of bound layer composition on glass transition and fragility

As interphases become more heterogeneous by adsorption of bimodal polymer chains with different mobilities, the glassy behavior may also be altered. To understand the consequences of the enhanced dynamic properties and the interphase effect on thermal properties, we performed glass transition (T_g) and fictive temperature (T_f) measurements on composites. Figure A3.2 (in Appendix 3) shows that T_g and T_f are not dependent on the bound layer thickness, which is consistent with small T_g changes reported for nanocomposites with attractive polymer-filler interactions[114]. T_g increase in attractive

nanocomposites has been commonly observed in confined environments induced by nanoparticles[115], however in our system particles do not form any confined regions since interparticle distance (ID)/$2R_g$ ratio falls in the unconfined regime. Fragility index is a measure of deviations from Arrhenius type behavior in the vicinity of glass transition and was shown to increase with monomer-surface interaction and particle loading[116]. We measured that with the adsorption of bimodal chains on particles, interphases become compositionally heterogeneous and dynamic fragility index increases from 115 to 168 (Figure 4.10b). This behavior is attributed to the increased interfacial entanglements of long chains. According to Adam-Gibbs theory[117], relaxations become increasingly cooperative and the size of the cooperative rearranging regions (CRR) governs the behavior of liquid upon cooling. With the loop forming long chains on the surface, the size of the CRR can be increased through entanglements in the interphase, thus composites become more fragile with Φ_L. We note the maximum in fragility is seen at Φ_L ~ 0.90, which may be explained by the additional dynamic heterogeneities created by the swelling of bound layer with short chains. It is interesting that the storage moduli shows a similar trend (Appendix 3, Figure A3.3), reaching a maximum around Φ_L ~ 90-0.95. It is known that the short chains may act as a solvent when Graessley parameter ($Gr = M_L Me^2/M_S^3$ with M_L, Me and M_S being molecular weights for long chains, entanglement and short chains) is above a critical value, $Gr>Gr_{,C}$. Gr,c is on the order of unity and Gr = 68*12.52/2.63=604 in our case so $Gr>>Gr_{,c}$ [118]. The dilation of the chains result in swelling of the entanglement tube which may result in longer loops on the surface compared to monomodal long chains. This effect is more apparent in the dilute regime of

the short chains since the long chains will start disentangling with larger short chain ratios and the reinforcement will be less pronounced. Results here suggest that using bimodal chains with small fraction of short chains on nanoparticle surface can further improve the interfacial strength between matrix and fillers. Furthermore, the maxima observed at similar compositions imply that the elastic reinforcement in nanocomposite melts can be related to dynamic fragility, which are often thought to be unrelated. Further theoretical and experimental studies are needed to elucidate the effect of bimodal adsorbing chains on the glass-transition and fragility index.

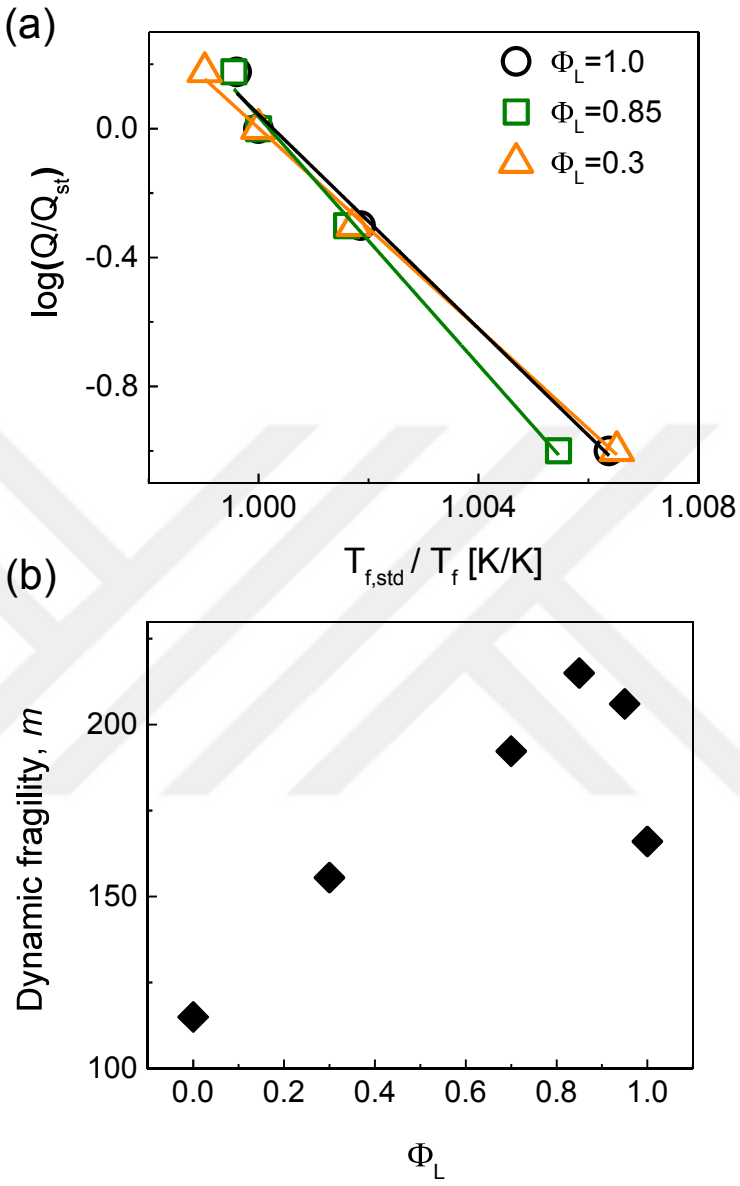

Figure 4. 10. (a) Representative normalized cooling rate versus normalized fictive temperature plots to determine fragility index. **(b)** Change in dynamic fragility index with long chain concentration on nanoparticles.

4.4. Chapter Conclusions

We showed on an attractive polymer nanocomposite system that bound layer interactions are tuned upon adsorbing homopolymers of bimodal chain lengths on nanoparticles. Subsequent changes in interfacial entanglement density enhance the elastic properties of nanocomposites. While glass transition is not affected by dynamic heterogeneities created with bimodal chains on surfaces, the fragility index is varied systematically from moderate to high values. These results corroborate the consequences of bound layer on mechanical and glassy properties of nanocomposites. Bimodal bound layers reveal the role of interphase layer on reinforcement mechanism and can further be used to modulate stiffness of polymer nanocomposites through shear-induced desorption/readsorption of chains.

CHAPTER 5

REVERSIBLE THERMAL-STIFFENING IN POLYMER NANOCOMPOSITES[4]

Chapter Summary

Miscible polymer blends with different glass transition temperatures (T_g) are known to create confined interphases between glassy and mobile chains. Here, we show that nanoparticles adsorbed with a high-T_g polymer, PMMA and dispersed in a low-T_g matrix polymer, poly(ethylene oxide) (PEO), exhibit a liquid-to-solid transition at temperatures above T_g's of both polymers. The mechanical adaptivity of nanocomposites to temperature underlies the existence of dynamically asymmetric bound layers on nanoparticles, and more importantly reveals their impact on microscopic mechanical behavior of composites, showcasing an unusual reversible stiffening behavior, which sets these materials apart from conventional polymer composites that soften upon heating.

5.1. Introduction

It is often desirable for materials to sustain fluidity at low temperature and exhibit reinforcement in the molten state. It is, however, a challenging task to retain mechanical performance, particularly in viscoelastic materials, with heating. This behavior, which holds a critical importance for mechanical adaptivity in soft materials, may be achieved with reversible stiffening at high temperatures. Stiffening in soft materials has been

[4] Submitted to ACS Applied Materials and Interfaces.

realized through responsive polymers or reversible crosslinking mechanism[79,119-121]. For example, layered films of poly(N-isopropyl acrylamide) (PNIPAM) tethered Au nanoparticles exhibit reversible hardening near the lower critical solution temperature (LCST) of PNIPAM, yet the moduli remain below kPa's due to existence of solvent[79]. Dynamic supramolecular linkages[122,123] and thermoreversible cross-linking[124-126] yield reversibility in elastic properties of hydrogels and networks with remarkable self-healing character; however, these materials do not exhibit liquid-to-solid transition as they are often permanently cross-linked. Carbon nanotube filled polydimethylsiloxane and liquid crystal elastomers under cyclic deformation are shown to self-stiffen[88,127,128], however, these mechanisms are either irreversible or require structural changes such as crystal orientation and stress-activated chemical reactions.

It is well established that mechanical behavior of polymer nanocomposites (PNCs) is controlled by matrix-filler interphases and dispersion states[129-131], which are governed by ligand type on nanoparticles and polymer chemistry. In nanocomposites, interactions between physically adsorbed polymer layer on particles (e.g. extent of entanglements) and matrix chains determine the mechanical properties of PNCs[23,108,132]. We recently showed that entanglements of free chains with the bound layer can irreversibly grow under large periodic oscillatory shear[22]. Here, we present a reversible thermal-stiffening behavior in solvent-free polymer nanocomposites without covalent bonding or temperature-responsive polymers, by exploiting interphases which consist of polymer blends with two different glass-transition temperatures (T_g). Such interphases

are utilized to result in dynamically asymmetric regions around nanofillers that will impact the macroscopic mechanical properties of bulk PNC films.

Dynamic asymmetry in miscible polymer blends with large T_g differences between the individual components (e.g. PEO, PMMA, poly(vinyl methyl ether)-PS, poly(vinyl acetate)-PEO) have been studied in bulk polymer blends that are rich in high-T_g component[133-137]. At sufficiently low temperatures, a low-T_g polymer is confined within glassy chains. Consequently, low-T_g chains remain highly mobile as their dynamics is decoupled from surrounding chains. Such dynamic heterogeneity is commonly attributed to compositional heterogeneities due to thermal fluctuations[138], or self-concentration due to chain connectivity[139]. At higher temperatures, however, both chains are mobile and their relaxation is rather cooperative[140]. Adsorbing a high-T_g polymer (PMMA) on 55 nm silica nanoparticles and dispersing them in a low-T_g matrix (PEO), hence, allows us to tune the mechanical response of composites with an effective interphase layer that becomes more mobile due to dynamic confinement of PEO chains in glassy PMMA at temperatures below $T_{g\text{-PMMA}}$.

The stiffening mechanism is schematically illustrated in Figure 5.1. We chose PMMA-PEO system because T_g's of these blend components are very different ($\Delta T_g \sim 200\ ^oC$) with negligible enthalpic interaction[141]. At temperatures lower than T_g of PMMA, PEO matrix chains are dynamically decoupled as they are highly mobile within glassy PMMA chains. The frozen PMMA chains do not contribute to composite relaxation, thus matrix PEO chains govern the flow behavior. At temperatures higher than T_g of PMMA, bound PMMA chains slowly relax and dynamically couple with PEO chains in the interphase.

This can result in dynamic pinning of PEO chains at particle surfaces and hence stiffen the bulk material.

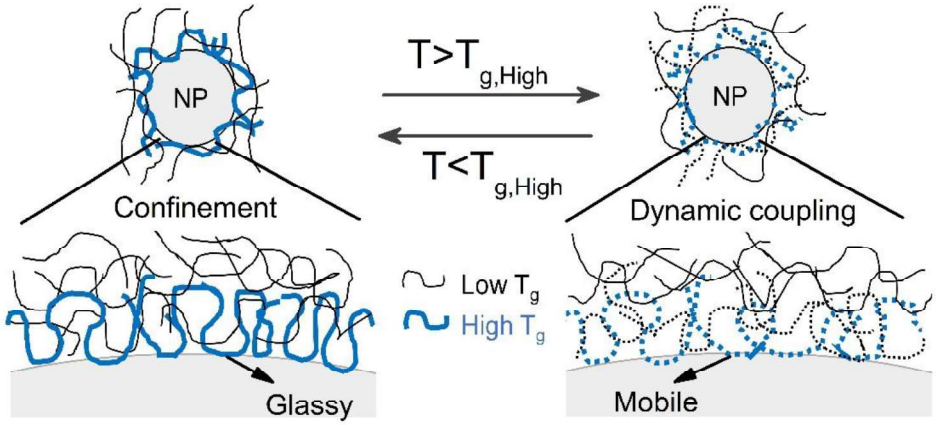

Figure 5. 1. Schematic illustration of thermo-responsive interphases in a polymer nanocomposite. Nanoparticles adsorbed with PMMA (thick blue lines) are dispersed in a miscible polymer PEO matrix (thin black lines). At temperatures below T_g of PMMA, as shown on the left, PEO chains are confined within frozen PMMA loops and its dynamic decouples from polymer on surface. At temperatures higher than T_g of PMMA, as shown on the right, adsorbed polymer becomes mobile and dynamically couple with matrix chains.

5.2. Experimental Section

5.2.1. Materials

PMMA at different molecular weights were synthesized by ATRP polymerization using p-toluenesulfonyl chloride (TsCl) initiator, CuBr-$CuBr_2$ catalyst system with 2,2'-

bipyridine in toluene under nitrogen environment at 70 ^{o}C. Colloidal SiO_2 nanoparticles (MEK-ST-L, 55 nm) dispersed in methyl ethyl ketone were supplied by Nissan Chemical America Corporation and used as received. PEO (-OH terminated and M_v = 100,000 g/mol) was purchased from Sigma Aldrich and vacuum dried for three days at room temperature.

5.2.2. Adsorbed polymer on nanoparticles and characterization

PMMA was dissolved in acetonitrile (at ~30 mg/mL) before colloidal SiO_2 was added at 30 wt% and mixed in a bath sonicator for 30 min. Solution was stirred vigorously for 2 h. Particles adsorbed with PMMA were recollected by centrifugation at 11,000 rpm for 5 min. Washing process was repeated 3 times to ensure all unbound chains were removed. Finally, collected particles were dispersed at 4-6 wt% in acetonitrile. DLS measurements were carried out with a Zetasizer NanoS (Malvern Instruments) at particle concentration of ~1 mg/mL in acetonitrile to measure the hydrodynamic thickness of adsorbed layers. Measurement duration was 11 sec, and data were averaged over 10 runs. TGA measurements were performed on a Q50 TGA (TA Instruments) to determine the mass amount of adsorbed polymer on nanoparticles. Measurements were performed under a constant flow of nitrogen of 20 mL/min at a heating rate of 20 ^{o}C/min, starting from 40 ^{o}C up to 580 ^{o}C, while pausing isothermally at 150 ^{o}C for 20 min to ensure samples were free of solvent and then finally incubated at 580 ^{o}C for 20 min.

5.2.3. Nanocomposite preparation and characterization

PEO was dissolved in acetonitrile at 25 mg/mL and PMMA bound particles were added while stirring polymer solution. Final solutions were stirred vigorously for 30 min and cast into Teflon dishes to form bulk films of ~100-150 μm films. Films were then annealed at 90 ^{o}C for 2 days, at 120 ^{o}C for 12 h and finally at 150 ^{o}C for 2 h under vacuum to remove any residual solvent. SEM images were obtained using a Zeiss Auriga Dual-Beam FIB-SEM on freeze-fractured surfaces of the films. Differential Scanning Calorimetry (DSC) was used to measure glass transition (T_g) and crystallization temperatures. To determine T_g, 5-10 mg samples were first heated to 175 ^{o}C for 5 min and then cooled down to 30 ^{o}C at 20 ^{o}C/min cooling rate followed by a heating ramp to 175 ^{o}C by 10 ^{o}C /min heating rate. T_g's were determined from the inflection point on heating curves. For melting temperature, samples were first equilibrated at -70 ^{o}C and then heated to 170 ^{o}C at 20 ^{o}C /min. After isothermal waiting for 5 min, samples were cooled back to -70 ^{o}C at the same rate. This cycle was repeated and crystallization temperatures were determined from the second cooling curves.

5.2.4. Rheological characterization

Rheology experiments were performed on a strain-controlled ARES-G2 (TA Instruments) with 8-mm stainless-steel parallel plate fixtures in a forced convection oven maintaining temperature within ±0.1 °C in nitrogen. Composite samples were molded with a vacuum assisted compression molder at 90 ^{o}C. For temperature sweep experiments, samples were first heated to 190 ^{o}C and thermally equilibrated to ensure complete melting of samples and then cooled down to 85 ^{o}C at 5 ^{o}C/min and equilibrated

for 5 min. Sinusoidal strain with an amplitude of 0.5% (in linear region) was applied at an angular frequency of 5 rad/sec in oscillation-temperature ramp mode. Temperature sweep experiments were performed at a strain amplitude of 0.5% (in linear regime for the whole temperature range) and at 5 rad/sec with 5 ^{o}C/min heating rate. Modulus data were collected at 0.2 Hz sampling rate. Heating-cooling cycle scans were performed following the same protocol. Isothermal aging response was determined by pausing the heating and cooling scans at desired temperatures and modulus data were collected. Measurements were done in quasi-equilibrium at which rate of deformation was much faster than the heating rate. This was confirmed on neat polymers with isothermal responses followed by heating steps. Strain amplitudes in linear regions at different temperatures for each frequency are determined. Creep-recovery tests were performed at different temperatures following 10 min equilibration. Small constant stress of 100 Pa was applied and corresponding deformation was monitored for 5 min and then stress is decreased to zero to monitor the recovery. Solid-to-liquid transition of PMMA in Figure 5.2d was obtained by heating PMMA to 200 ^{o}C and waiting for thermal equilibrium for 10 min. Samples were then cooled down to 110 ^{o}C at 10 ^{o}C/min rate and waited for 10 min for thermal equilibrium. Sample was then heated to 200 ^{o}C at 5 ^{o}C/min (same rate as PEO and composites) while small strain amplitude of 0.1% is applied at 5 rad/sec frequency with data collected at a 0.4 Hz. Data below 110 ^{o}C was obtained in a similar way but at high-torque mode of the instrument to prevent overshoot.

5.3. Results

We first adsorbed PMMA of different chain lengths (68 and 2.3 kg/mol) on 55 nm colloidal silica (SiO_2) nanoparticles to investigate the effect of interparticle distance and interphase on stiffening. PMMA adsorbed particles at loadings of 15-50 wt% are then dispersed in PEO matrix (M_w: 100 kg/mol). Figure 2a and Appendix 4-Figure A4.1 show that nanoparticles are individually dispersed in PEO at all particle concentrations. The average interparticle distance is calculated using $ID=d[(\Phi_{max}/\Phi)^{1/3}-1]$, where d is the number-average particle diameter and Φ_{max} is the maximum volume packing fraction which is $2/\pi$ for the randomly distributed particles. The ratio of interparticle distance between particles and size of PEO chain, $ID/2R_g$, is systematically varied to create unconfined and confined polymer regions (Figure 5.2b). Bulk T_g for 68 and 2.3 kg/mol PMMA is determined to be 130 and 92 ^oC, respectively using a differential scanning calorimeter (DSC) (Appendix 4-Figure A4.2d). PEO-PMMA is an LCST type blend system[142,143] and has been shown to be miscible up to above 230 ^oC for similar molecular weights[144]. We chose our experimental temperature range 80-200 ^oC as it is well above the crystallization temperature of nanocomposites (Figure 5.2c). Note that T_g of PMMA and PEO is 135 and -65 ^oC, respectively. The amount of adsorbed PMMA is very small ~8 wt%, even in the highest particle loading of 50 wt%, that its T_g cannot be measured in nanocomposites.

Dynamic linear mechanical response (at fixed frequency, 5 rad/sec) for homopolymers and 20 wt% composite with PMMA (68 kg/mol) adsorbed SiO_2 particles to a temperature ramp (5 ^oC/min) is presented in Figure 5.2d. Bulk PMMA undergoes a glass-rubber

transition at ~135 ^{o}C which is also seen in the loss tangent peak and its elastic modulus decreases by three orders of magnitude. Neat PEO behaves as a viscous liquid with low elastic moduli (~kPa) decreasing monotonically with temperature. The composite behaves similar to PEO up to $T_{g,PMMA}$ with typical moduli below 10 kPa and then stiffens with temperature beyond $T_{g,PMMA}$ to a modulus close to the entanglement plateau of PMMA (1.8 MPa). Loss tangent for the composite clearly shows the switching of mechanical behavior from liquid to solid states with temperature.

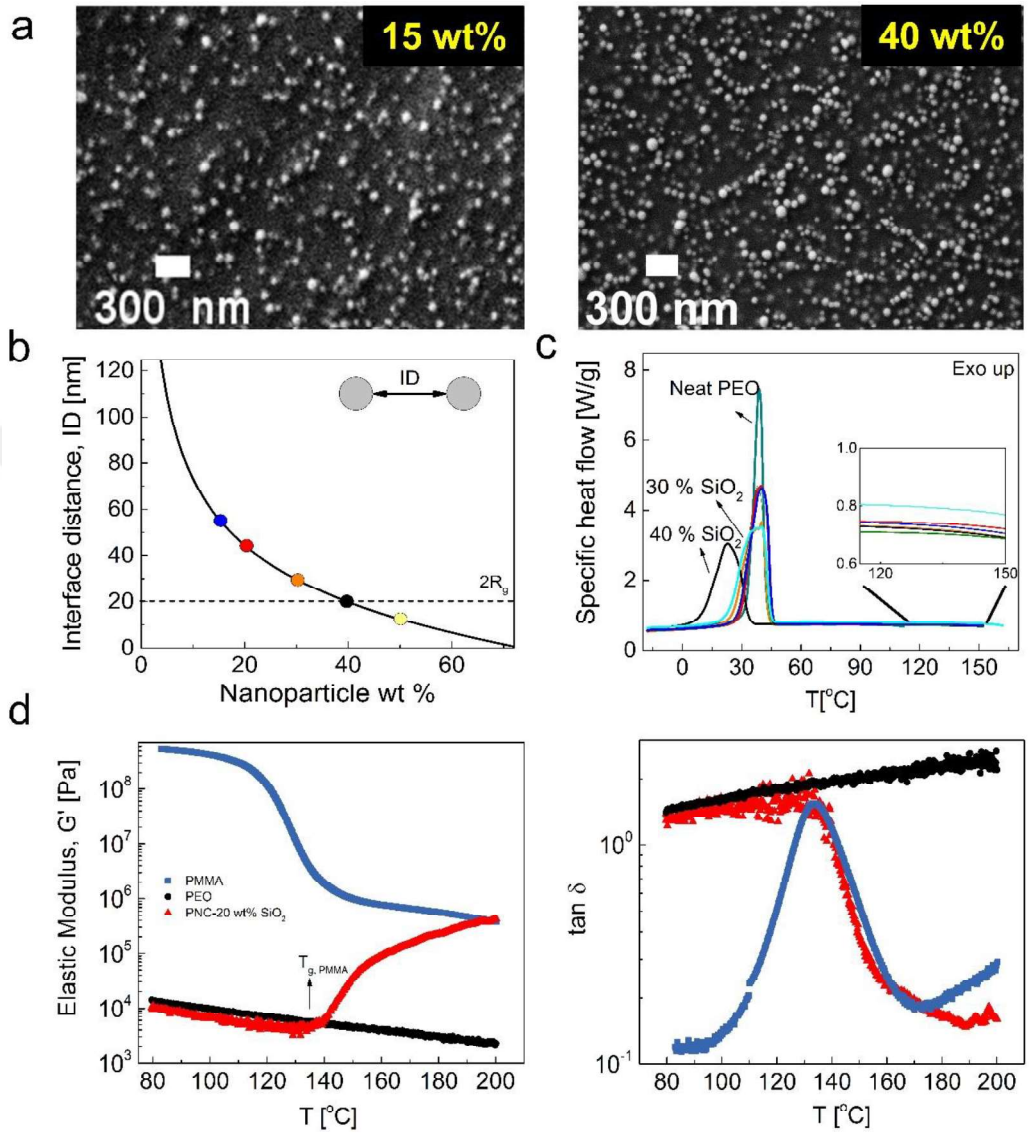

Figure 5. 2. Sample characteristics and thermo-responsive behavior of PEO-SiO_2 nanocomposites relative to pure polymers. **(a)** Scanning electron micrographs on freeze-fractured surfaces of nanocomposites with 15 and 40 wt% SiO_2 nanoparticles adsorbed with 68 kg/mol PMMA show the individual dispersion of nanoparticles in PEO matrix

(see Supplementary Figure S1 for different compositions). (**b)** Average interparticle distance (ID) versus particle loading. Dashed line is for the matrix chain size ($2R_g$). (**c)** Melting temperatures of neat PEO and composites are obtained in heat flow curves. (**d)** Elastic modulus, G′, behavior of PMMA, PEO and 20 wt% composite versus temperature (at 5 ^oC/min heating rate) and their corresponding loss tangent behavior.

By increasing particle loading, liquid-to-solid transitions broaden as shown in Figures 5.3a-b. All 68 kg/mol PMMA adsorbed particles induce stiffening, yet, the transition temperature shifts to a higher value as the interparticle separation (ID) increases. This shift can be explained by the longer time required for reptating chains within larger interparticle distances. Loss angle behavior clearly presents a liquid-to-rubbery transition for all compositions. Note that the particle loading decreased the low temperature moduli as well as the transition temperature. This is very unusual behavior since nanoparticles usually improve the moduli. However, in the case of blend interphase, this seems to be reversed due to enhanced mobility of host PEO chains in the presence of glassy PMMA chains.

It is seen that even in small particle loadings with $ID>>2R_g$, composites stiffen in a similar manner. This suggests that confinement induced by nanoparticles is not effective in stiffening. It is seen in Figure 5.3a that the modulus of PEO/PMMA blend with (95:5 wt:wt) composition decreases with temperature similar to neat PEO, which indicates that stiffening arises from nanoparticles adsorbed with long polymer chains. Thus, the dynamic coupling of the PEO and PMMA near the nanoparticle surface, resulting

dynamic pinning of PEO chains at the surface results in stiffening. In addition, percolation of the nanoparticles cannot explain the observed stiffening since the percolation would result in highly reinforced composite at low temperatures through glassy bridges of PMMA and softening as the PMMA chains become more mobile. To further elucidate the percolation effect, 50 wt% sample with ($ID/2R_g<1$) (Appendix 4-Figure A4.4a) is used. The starting modulus value is the highest of all composites due to possible interparticle bridging, yet, the stiffening transition is similar to other compositions. Note that the transition temperature for this highly confined sample shifts back to higher levels possibly due to restricted chain motion within such small spaces rather than the percolation effect.

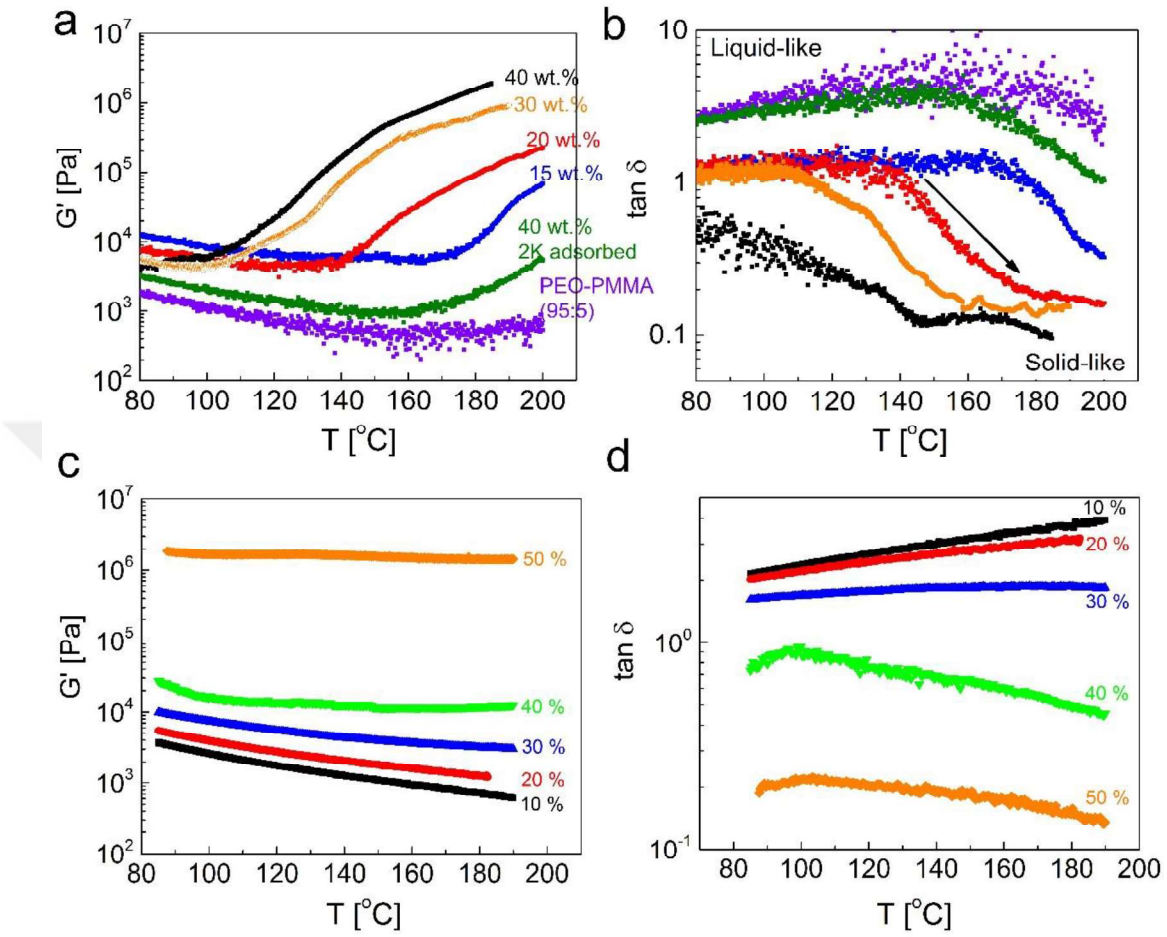

Figure 5. 3. Effect of particle loading on mechanical response of conventional and thermos- stiffening nanocomposites. **(a)** Elastic moduli and **(b)** loss tangents of PEO-PMMA blend (in the absence of SiO_2) and nanocomposites with various loading of nanoparticles adsorbed with 68 kg/mol PMMA versus temperature. **(c)** Elastic moduli and **(d)** loss tangents of conventional PEO-SiO_2 nanocomposites (with no bound PMMA).

Molecular weight of adsorbed polymer also affects the thermo-stiffening because shorter chains have lower T_g's due to entropic contribution of chain ends and loop formations and interfacial entanglements are more effective with longer chains. Particles adsorbed with short PMMA chains (2.3 kg/mol; Đ: 1.13) do not effectively stiffen the composites compared to other samples with 68 kg/mol PMMA adsorbed particles. We further tested the chain length effect by adsorbing long (M_w = 200 kg/mol, Đ: 1.17) and short PMMA chains (M_w = 9.6 kg/mol, Đ: 1.06) (Figure 5.4 and Appendix 4-Figure A4.3). Interphases with longer chains reinforce the composites at low temperatures and exhibit thermo-stiffening at elevated temperatures. Unlike long chains, only 40 wt% composite with particles adsorbed with 10 kg/mol PMMA exhibits stiffening. Note that particles are uniformly dispersed in all these composites.

We additionally prepared PEO nanocomposites with non-adsorbed SiO_2 (Figure 5.3c-d), a conventional PNC case in which bound and matrix polymers are chemically identical. Appendix 4-Figure A4.1 displays uniform dispersion of bare SiO_2 nanoparticles in PEO. It is observed that the composites are reinforced with the addition of fillers and soften with temperature in the absence of adsorbed layers. This is clearly different than nanocomposites containing dynamically asymmetric interphases studied in our work.

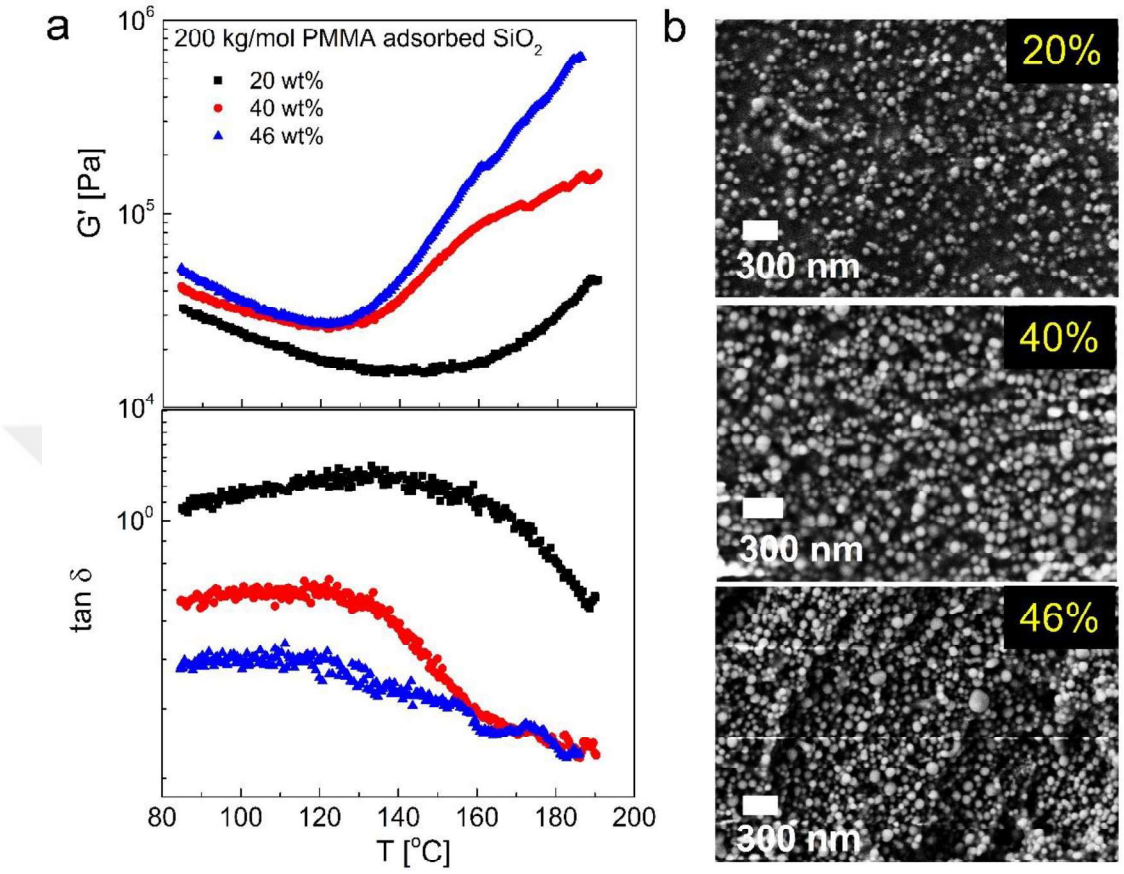

Figure 5. 4. Stiffening response from longer adsorbed chains. Elastic moduli and loss tangents of composites with 200 kg/mol PMMA (~~Đ~~: 1.17) adsorbed SiO_2 with increasing temperature. Dispersions at 20, 40 and 46 wt% are shown in SEM images.

Deformation rate has also strong effect on thermo-stiffening. Frequency sweeps of a 30 wt% composite (Figure 5.5a-b) present unusually high modulus at higher temperatures with no frequency dependence which is a typical elastic network response. Upturns at low frequencies above $T_{g,PMMA}$ suggest aging of the sample between long deformation cycle times. We applied a temperature ramp with 1, 5 and 50 rad/sec

deformation frequencies (Figure 5.5d) to evaluate the effect of deformation rate. At high temperatures, moduli become independent of frequency, while low-temperature moduli increase with frequency, that is in-line with frequency sweep results. It is noteworthy that the transition temperature shifts from 130 to 150 ^{o}C with frequency due to insufficient time for relaxation to occur at high frequencies, which in turn shifts T_g to higher temperatures. Flow and deformability of a 30 wt% composite was further tested at a constant stress of 100 Pa (creep) and subsequent recovery in cessation (Figure 5.5c). At 110 ^{o}C, the material is viscoelastic and steadily flows with time; however, at high temperature, deformability significantly decreases and strain remains constant over time.

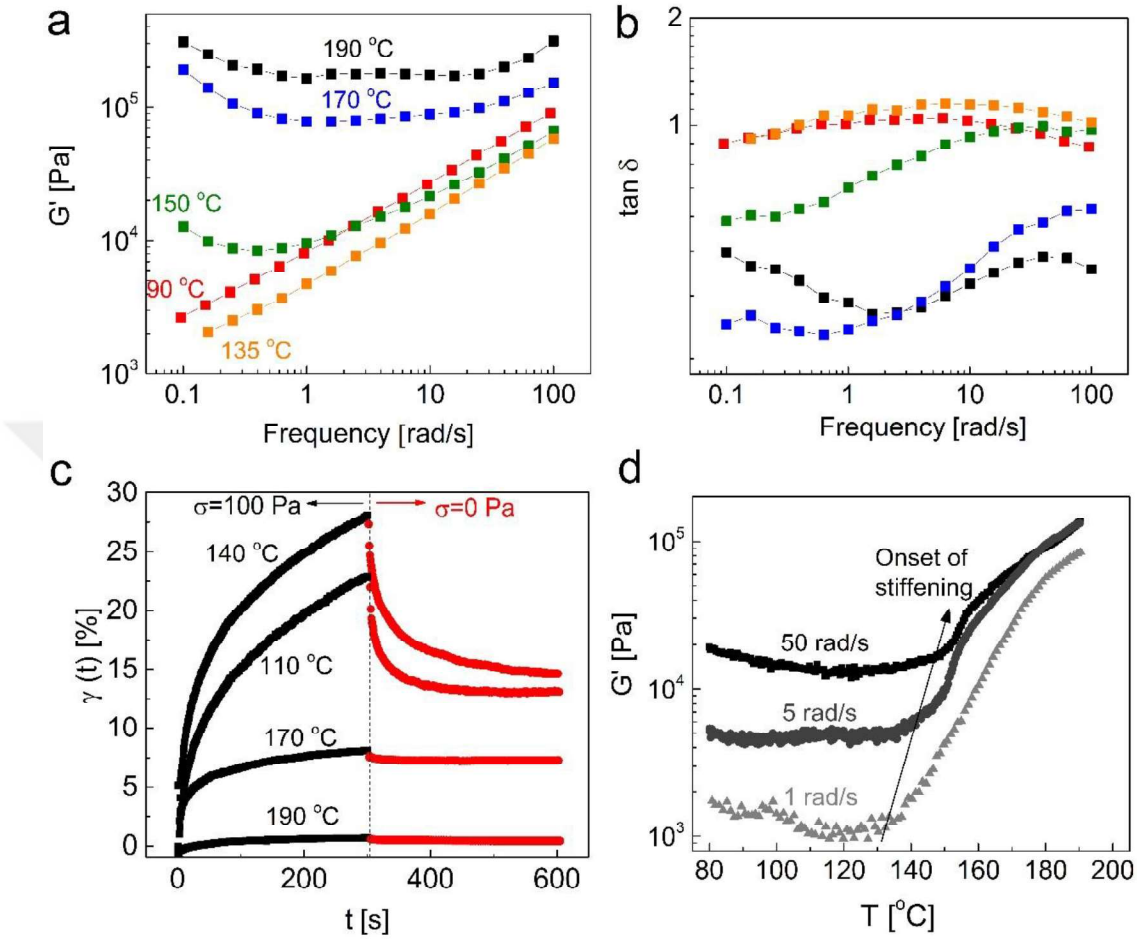

Figure 5. 5. Frequency dependence of thermo-stiffening and creep-recovery behavior. Effect of linear deformation frequency on **(a)** elastic modulus and **(b)** loss tangent at different temperatures of a 30 wt% composite displays frequency-independent moduli at low temperature while presenting unusually high elastic moduli at high temperatures. Upturns at low frequencies imply aging response between two data points. **(c)** Strain response of the same composite to a constant stress of 100 Pa (creep) and corresponding recovery upon removal of stress at different temperatures. **(d)** Temperature sweeps (5

^{o}C/min) at different linear deformation frequency shows the onset of stiffening is shifted to higher temperatures with frequency.

Periodic temperature scans (at 5 ^{o}C/min) of a 40 wt% sample between 80 and 180 ^{o}C show that stiffening/softening is achieved over many cycles through the reversibility of transition (Figure 5.6a-b). Complex viscosity presents similar increase by heating and completely reverts to its original value upon cooling, with clear thermal hysteresis centered around $T_{g,PMMA}$. It is demonstrated in Figure 5.6c that the composite and neat PEO flow at 120 ^{o}C and composite retains its bulk shape at 190 ^{o}C compared to PEO melt. Increase in elastic modulus with temperature is linear above transition temperature with a typical slope of ~ 4.8 kPa/^{o}C +/- 1.2 (Appendix 4-Figure A4.4b). Since mechanical behavior is governed by the coupling of fast PEO and slow PMMA dynamics at interphases at high temperatures, the slowing down dynamics of PEO within interphase causes stiffening mechanism that is analogous to network elasticity. Modulus of a polymer network increases linearly with temperature and can be approximated by $G = \rho RT/M$ in a small deformation regime. In our composites, slow dynamics at interphases is transmitted through bulk with entanglements of PEO; thus M becomes entanglement molecular weight which is 1730 g/mol[96]. Since bulk density of PEO is 1.06 g/cm[96], modulus of a polymer network is found to be 5 kPa/ ^{o}C, which is equal to the slope of the stiffening obtained in our experiments (Appendix 4-Figure A4.4b).

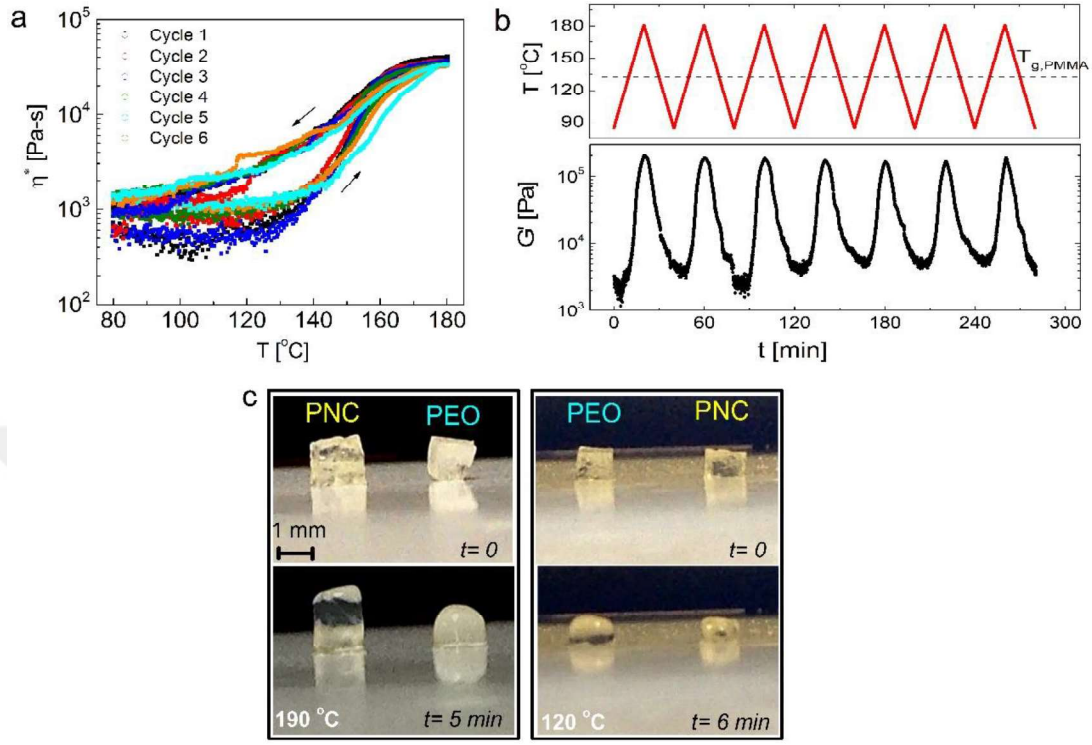

Figure 5. 6. Reversibility of complex viscosity and elastic moduli. **(a)** Complex viscosity behavior of a 40 wt% composite upon heating and cooling cycles (5 ^{o}C/min) follows the same heating and cooling paths with clear hysteresis around $T_{g,PMMA}$. **(b)** Elastic modulus of a 40 wt% composite in response to periodic temperature scans between 80 and 180 ^{o}C. **(c)** PEO and 30 wt% composite (PNC) show similar deformability after waiting for 6 min at 120 ^{o}C. After waiting at higher temperatures (190 ^{o}C) for 5 min, PEO melts and PNC retains its shape.

5.4. Discussion

Colmenero et al. recently studied the effect of cross-linking on chain dynamics by using PMMA soft nanoparticles dispersed in PEO matrix[145-147]. It was found that PEO dynamics above T_g of PMMA becomes slower than pure PEO dynamics by two orders of magnitude in its blend with 75 wt% PMMA[145]. Further, it was reported that chains deviated from Gaussian behavior in this regime and dynamics slows down with an increase in temperature. The authors speculated that this behavior may be due to locally trapped PEO chains within loops near soft nanoparticles' surfaces that are highly close-packed at 75 wt% loading. Unlike their system, we use PMMA as a thin bound layer of (~ 2 nm thick) on nanoparticles in PEO matrices. The postulated mechanism of loopings in the bound layers and slow chain dynamics has relevant consequences on mechanical properties in our nanocomposites at low particle concentrations. Slow motions of chains at the interphase, thus, give rise to a controlled stiffening in the low-T_g matrix.

Time evolution of elastic moduli demonstrate aging of composites above T_g of PMMA. We interrupted heating and cooling cycles with isothermal steps (Figure 5.7a and Appendix 4-Figure A4.5a-c) and measured the growth rates of elastic moduli for 68 kg/mol PMMA adsorbed SiO_2 (Figure 5.7b). Changes in the moduli during cooling steps show that stiffening is both temperature and time dependent. Note that stiffening rates in the composite are similar in heating and cooling steps. We applied the same protocol on neat PMMA and PEO, and observed that both polymers soften with heating; however moduli quickly reach plateaus at isothermal steps (Appendix 4-Figure A4.5d-e). This verifies that high temperature aging is not due to thermal equilibration of neat

components; rather it occurs at the interphase. All composites, independent on the nanoparticle loading, showed Arrhenius-type dependence on stiffening rates (Figure 5.7b), with the same activation energy of E_a ~108 kJ/mol. The vertical shift of the curves for composites with larger interparticle separation is because of the larger diffusion distances for interfacial effect to propagate into bulk matrix. As entanglements form in a diffusive process, one can obtain the response for equivalent diffusion distance for each composite by shifting the kinetic data vertically by a factor of $(ID/2R_g)^2$. Points then overlap on a linear line, suggesting that the mechanism for aging is independent of particle loading, yet slower for large interparticle separations.

Since the glassy-to-rubbery transition of PMMA leads to stiffening, the activation energy for the stiffening mechanism can be related to the activation energy for PMMA relaxation around its T_g. Two types of relaxations are important for polymers. (i) α-relaxation due to segmental motions which also govern the glass transition and (ii) β-relaxation due to side group motions (i.e. methyl group rotation) which is generally fast. It was shown that the secondary (β) relaxations are rather insensitive to blending or temperature[145,148] while α-relaxation is strongly altered by blending[136,145,149]. Dynamic confinement effect was also shown on PVAc-PEO blend system using quasi-elastic neutron scattering (QENS)[134]. A cross-over temperature was found ~70 ^oC higher than T_g of the blend. This cross-over region interestingly coincides with α-β merging region (typically occurs at $T_g/T > 0.85$) of the high-T_g component[134,150]. Similar crossover temperature was reported for PEO/PMMA system by Richter et al. above T_g of the blend by 65 ^oC[151]. Temperature range of our experiments also coincides with the merged

relaxation of PMMA. We obtained the activation energy from isothermal aging behavior above $T_{g.PMMA}$ and obtained 108 kJ/mol, which agrees very well with the number reported by Dionísio et al.[152] (~120 kJ/mol) and Schröter et al.[153] (~110 kJ/mol) for the α-β merging of PMMA. We compared the activation energies of 40 wt% composites with their particles adsorbed with 200 kg/mol and 10 kg/mol PMMA obtained through similar aging experiments (Appendix 4-Figure A4.6). The activation energy decreases with chain length presumably because long chains require more cooperativity to become mobile as they undergo glass-transition. Note that the activation energy of PMMA relaxation at an attractive surface can be significantly different than that in bulk form. The adsorbed PMMA has fraction of trains that are in direct contact with the surface while loops, and tails are relaxing much faster. As the number of attached monomers are $\sim N^{1/2}$ for a chain with degree of polymerization N, it is expected that the molecular weight can have strong influence on the activation energy required for α and β processes. This discussion presents that small amount of adsorbed PMMA layer on particles controls the relaxation behavior of the composite, thus the stiffening behavior is governed with the relaxation of PMMA chains as they interact with the fast PEO chains.

Finally, we demonstrate the performance of a 30 wt% thermo-stiffening composite to an arbitrary temperature change between 80 and 180 ^{o}C, subjected to different ramps at 2-20 ^{o}C/min (Figure 5.7c). While PEO softens with temperature, PNC follows the thermal trace and stiffens with increasing temperature. At slow heat ramps aging response becomes more apparent, whereas at fast ramps composites can also thermally-stiffen.

Our results demonstrate that coupling and decoupling mechanism of dynamically asymmetric polymer blends on nanoparticles provide a robust way of creating self-stiffening in solvent-free nanocomposites. The mechanism presented here is driven by large T_g disparity of polymers at interphases and controlled by mobility of the high-T_g bound polymer layer on nanoparticles. When interphase is frozen, soft matrix polymer dominates the flow behavior; on the contrary, when the interphase is mobile, its dynamics is coupled with entangled matrix chains. Consequently, an unusual and thermo-reversible liquid-to-elastic transition can be achieved in melt systems. We conjecture that similar thermo-stiffening may be achieved in polymers loaded with functional fillers such as plasmonic nanoparticles to design shape changing and stiffening materials, which can lead to their transformative applications in soft robotics and flexible electronics.

It is known that physical adsorption of polymer chains adjacent to an attractive surface leads to an increase in T_g, which also reveals the dynamic heterogeneities in polymer relaxation[154,114,155]. In conventional nanocomposite design, the bound and the matrix chains are commonly chosen to be chemically identical. Despite significant reinforcement seen in such nanocomposites, the mobility difference between bound and free chains are limited and often results in increase of T_g of the composites by a few tens of degrees[114]. It has been long assumed that the bound polymer forms a glassy layer around the nanoparticles which percolates upon decreasing temperature and reinforces the composites. In contrast, Krutyeva et al.[108] recently showed by neutron spin-echo technique that the bound polymer is not glassy at all and forms an effective interphase region by entangling with surrounding chains, which slows down the dynamics. Here by

using highly asymmetric chains with negligible enthalpy interaction within the interphase region, we switched the behavior of bound polymer layer from glassy to mobile while the matrix chains remains mobile. Our results suggest that the composites are reinforced when the bound polymer layer is mobile, rather than being glassy.

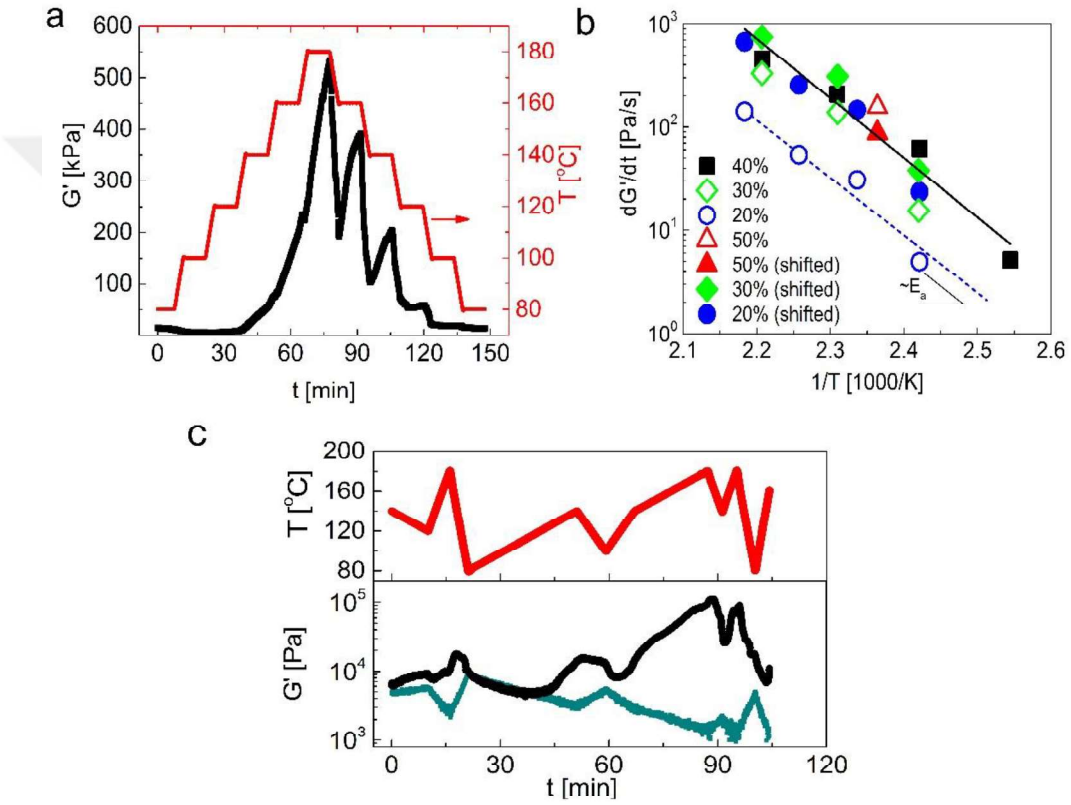

Figure 5. 7. Aging dynamics and on-demand thermal stiffening. **(a)** Step-wise temperature increment (with 5 ^{o}C/min heating rates) on a 30 wt% nanocomposite reveals that stiffening rate is temperature dependent and reversible upon cooling. **(b)** Stiffening rates for different compositions follow an Arrhenius behavior. Activation energy (slope of the fitted lines) is 108 kJ/mol at different particle concentrations. **(c)** Mechanical

response of neat PEO and 30 wt% nanocomposite to an arbitrary thermal load applied between 80-180 ^{o}C with 2-20 ^{o}C/min temperature ramps.

We note that the conventional polymer nanocomposites with identical bound and free chains constitute one extreme case in which there is negligible asymmetry in dynamics and composites soften with temperature. Our study presents another extreme situation in which the dynamic asymmetry is very large and the composites unusually thermo-stiffen. We conjecture that the liquid-to-solid transition as well as stiffening can be observed, although limited, in other systems with smaller dynamic asymmetry provided that the slow component changes its behavior from glassy to mobile in the time-scale of the relaxation of mobile chains. For the miscible bulk PEO-PMMA and PVAc-PEO systems, dynamic decoupling starts 65-70 ^{o}C above T_g of the blend upon cooling[134,151]. For systems with high enthalpy interaction, the stiffening transition may be shifted up or down depending on the nature of interaction.

5.5. Chapter Conclusions

Our results demonstrate that coupling and decoupling mechanism of dynamically asymmetric polymer blends on nanoparticles provide a robust way of creating self-stiffening in solvent-free nanocomposites. The mechanism presented here is driven by large T_g disparity of polymers at interphases and controlled by mobility of the high-T_g bound polymer layer on nanoparticles. When interphase is frozen, soft matrix polymer dominates the flow behavior; on the contrary, when the interphase is mobile, its dynamics is coupled with entangled matrix chains. Consequently, an unusual and thermo-reversible

liquid-to-elastic transition can be achieved in melt systems. We conjecture that similar thermo-stiffening may be achieved in polymers loaded with functional fillers such as plasmonic nanoparticles to design shape changing and stiffening materials, which can lead to their transformative applications in soft robotics and flexible electronics.

CHAPTER 6

ANOMALOUS PARTICLE RELAXATION IN POLYMER MELTS WITH DYNAMICALLY ASYMMETRIC INTERPHASES

Chapter Overview

We have discussed in Chapter 5 that PEO becomes mobile when it is confined within frozen PMMA chains at temperatures below $T_{g,PMMA}$. At temperatures higher than $T_{g,PMMA}$, on the other hand, bound PMMA chains become mobile and this dynamic heterogeneity of miscible PEO-PMMA blend in the interphase slows down dynamics of PEO. This Chapter discusses the X-ray photon correlation spectroscopy (XPCS) experiments that will provide insight into the dynamics of particles as the interphase regions are stiffened with heating. XPCS experiments below and above $T_{g,PMMA}$ will indicate the viscosity change within dynamic asymmetric interphases. It is hypothesized that particles' mobility shifts from diffusive to non-diffusive mode due to interfacial stiffening. It is expected that relaxation time will increase and the local viscosity gradient can be calculated from the diffusivity measured with this technique where auto-correlation functions are analyzed at varying temperatures. We showed that bare SiO_2 particles in PEO matrix follow diffusive dynamics and the relaxation time increases by lowering temperature due to slower dynamics of particles. Additionally, we found that dynamics of PMMA adsorbed particles dispersed in PEO is hyper-diffusive at low temperature with small relaxation times; and particle dynamics switches to a diffusive

mode with unusual increased relaxation times at high temperature. These dynamic results are an important supporting evidence for the origin of thermally stiffening polymer composites, where local viscosity changes within dynamic asymmetric interphases or T_g gradients around particles presumably control the macroscopic mechanical properties.

6.1. Introduction

Many complex fluids, ranging from dense emulsions and foams to colloidal gels and polymers, exhibit very slow dynamics and aging which has drawn much scientific attention[156,157,158,159,160]. XPCS has emerged as a powerful tool for investigating dynamical and rheological properties of slow dynamics experienced by these complex fluids[161]. The technique is similar to DLS where the fluctuations of scattered visible light provide dynamic information of a material[162]. X-rays with much shorter wavelengths than DLS can access the length scales down to 10 nm's. In addition to wavevector differences, DLS is limited to dilute suspensions due to possible multiple scattering at high concentration regime. Multi-speckle dynamic light scattering (MSDL) was developed before XPCS and provided anomalous dynamic aging behavior in colloidal suspensions with large particles[160,163]. XPCS expands the length scale covered by MSDL, making it possible to measure the slowed down dynamics of nanoparticles in polymers.

XPCS has been used, often with dilute marker nanoparticles, to obtain local viscosity of polymer in thin films[164] or bulk[165] to explain the origin of T_g shift reported in confined polymers, the surface composition of miscible polymer blends[166], gel-like

mechanical behavior and aging of grafted nanoparticles in polymer melts[167], effect of particle surface chemistry on particle diffusion[168].

In this study, we use nanocomposites of bare and PMMA adsorbed SiO_2 nanoparticles dispersed in PEO matrix and investigate how dynamic asymmetry between surface-bound and matrix chains influence the local viscosity around nanoparticles by probing the nanoparticle relaxation dynamics in XPCS. Dynamic confinement induced by the glassy chains on the matrix polymer is shown to decrease the bulk viscosity of the nanocomposites, while at high temperatures dynamic coupling between these chains results in dramatic increases in viscosity. We show that particle motion in a host polymer matrix can be accelerated at low temperatures, whereas their relaxation slows down at higher temperature by forming a dynamically asymmetric polymer blends within the interphase.

In an XPCS measurement, time auto-correlation function of SAXS intensity at increasing delay time t ($I(q,t)$) is calculated from $g_2(q,t)=\langle I(q,0).I(q,t)\rangle / \langle I(q,0)\rangle^2$ where $I(q,0)$ is the SAXS intensity at a reference time and $\langle .. \rangle$ refers to an ensemble average over different speckles at the same q and over t. The auto-correlation function, $g_2(q,t)$, is modeled as $g_2(q,t)=1+A[g_1(q,t)]^2$ where A is the speckle contrast and $g_1(q,t)$ is the intermediate structure factor (ISF). ISF is best described by an exponential form, $g_1(q,t)=\exp[-(t/\tau)^{\beta}]$, with characteristic relaxation time, τ, and stretching exponent, β. The auto-correlation function is then expressed as $g_2(q,t) = 1 + A[\exp[-(t/\tau)^{\beta}]]^2$ and the

fitting parameters τ and β are obtained from the experimental auto-correlation data. A is an instrument factor.

In a simple diffusive process, the ISF has a single exponential form with $\beta = 1$. Most complex fluids exhibit deviation from single exponential to stretched ($\beta < 1$) or compressed ($\beta > 1$) exponential. The compressed exponential decay mostly occurs in glassy medium, where fast relaxation modes are suppressed possibly due to dynamically heterogeneous regions in the medium and commonly observed in soft glassy materials near jamming transition[156,164,169]. Nanoparticles in polymers also present compressed exponential relaxation near T_g [169].

6.3. Experimental Section

We used the samples prepared in Chapter 5 in XPCS experiments. Bare-SiO_2 adsorbed with 68 kg/mol PMMA are dispersed (15 wt%) in PEO (100 kg/mol) matrix. Samples were molded into 1 mm diameter holes on aluminum samples holders of 0.5 mm thickness by melting at 90 ^oC and pressing in the rheometer plates. XPCS measurements were performed at the beamline 8-ID-I in Advanced Photon Source at Argonne National Laboratory. The sample areas of 20 μm x 20 μm were illuminated by coherent X-rays with photon energy of 11 keV. The normalized intensity-intensity auto-correlation function was obtained over the wave vector range 0.027 $nm^{-1} < q < 0.3$ nm^{-1}. Samples were held at 120 ^oC for 10 min for melt equilibirum. Measurements were then performed at 75, 90, 120, 140, 160 ^oC for 10 min thermal equilibration priori. The same protocol is used for each sample to match their thermal history. For each temperature, data collected

at five different locations, each 40 μm apart, to ensure uniformity and stability of the particle dispersion as well as consistency of the correlation function. XPCSGUI[170] software provided at the beamline was used to analyze the average SAXS and auto-correlation functions.

6.3. Results and Discussion

It is important that nanoparticles maintain their well dispersion when samples are heated to high temperatures. To evaluate the dispersion stability and uniformity, we look into the averaged SAXS intensity for bare-SiO_2 dispersed in PEO and PMMA (68 kg/mol) adsorbed SiO_2 dispersed in PEO at 15 wt% loading. Figure 6.1 shows the time average SAXS images at 80 ^oC and 150 ^oC for the whole detector area. Structure is isotropic and intensity drops rapidly with q; thus a rectangular region shown is chosen to obtain the auto-correlation functions covering a range of 1msec to 100 sec delay time. Figure 6.2 compares the SAXS intensity obtained at different locations for two different temperatures, showing the uniformity of particle distribution both for bare and PMMA coated nanoparticles. The intensity is fit to a one-level Baucage function (shown in the inset of Figure 6.2b), $I(q) = G\exp(-q^2 R_g{}^2/3) + B\,[\frac{(erf(qR_g/\sqrt{6}))^3}{q}]^p$, where R_g is the radius of gyration, p is the fractal dimension of the scattering objects, and G, and B are constants. The R_g determined from the fitting is 29.7 nm, which agrees with the actual size of particles (27 nm). Intensity at low-q reaches a clear plateau, with a slight interference peak appears at q ~ 0.056 nm^{-1} due to large particle loading. This

corresponds to average center-to-denter distance ($d=2\pi/q$) of 112 nm. ID (interparticle distance) obtained from SAXS is thus ~57 nm, which is in agreement with the theoretical prediction (55 nm) given in Chapter 5 for 15 wt% loading. At high q (Porod regime), the intensity scales as, $I \propto q^{-4}$, with p=4, suggesting particle dispersion with sharp surfaces. Figure 6.2b shows that SAXS patterns do not change at different temperatures. This confirms that the nanoparticles do not aggregate into clusters when heated.

Dynamic aging is usually attributed to stress dipoles created near the jamming transition, which results in a temporal evolution to a slower dynamics with more hyper-diffusive mechanism. Polymer nanocomposites have shown to exhibit significant aging at high particle loadings. In XPCS measurements, aging manifests as a shift in the correlation function at different measurement times. Figure 6.3 displays the auto-correlation functions for bare-SiO_2 and PMMA adsorbed SiO_2 in PEO at 75 and 140 ^oC, which shows same scattering profiles from different areas of samples.

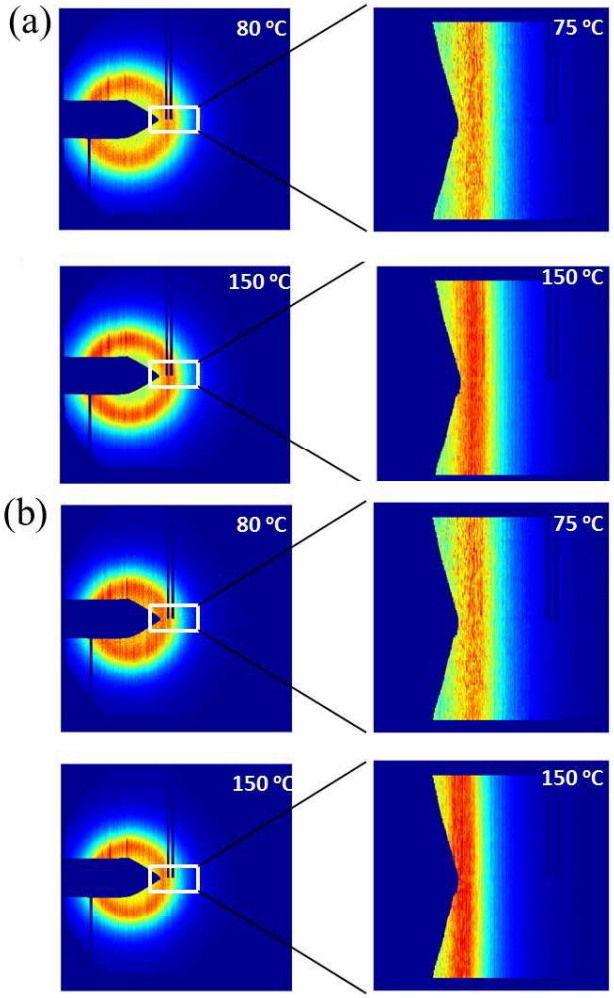

Figure 6. 1. SAXS patterns for **(a)** bare SiO_2 and **(b)** PMMA adsorbed SiO_2 at two temperatures. The rectangular area shows the region used to obtained auto-correlation functions.

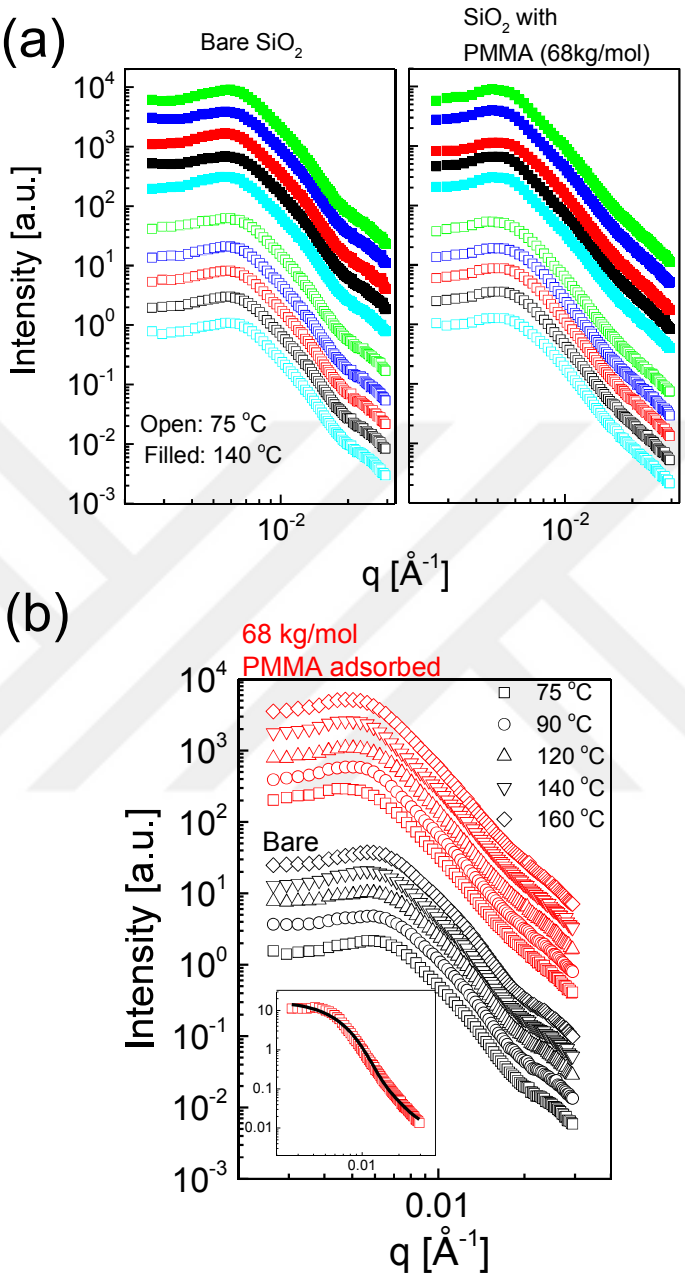

Figure 6. 2. (a) SAXS intensity curves for bare and PMMA adsorbed SiO_2 in PEO at 75 and 140 ^{o}C obtained from different areas of a sample. **(b)** Comparison of SAXS curves at

different temperatures. Inset panel shows the fit to one-level unified equation for PMMA adsorbed particles in PEO. Curves are shifted vertically for clarity.

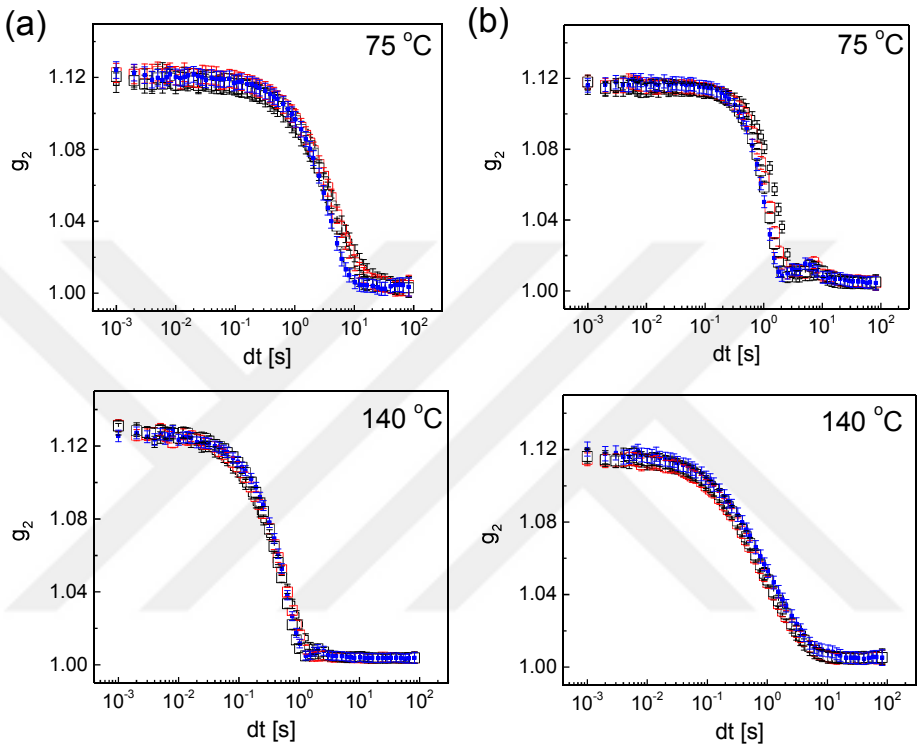

Figure 6. 3. Overlaying of auto-correlation functions of **(a)** bare SiO_2 and **(b)** PMMA adsorbed SiO_2 in PEO at 75 ^{o}C and 140 ^{o}C temperatures obtained at different sample locations presents no dynamic aging during measurement time.

Auto-correlation functions and fitting parameters for all temperatures are displayed in Appendix A5. Relaxation behavior of the bare and PMMA adsorbed particles at 75 ^{o}C ($T<T_{g,PMMA}$) and 140 ^{o}C ($T>T_{g,PMMA}$) at q = 0.004756 $Å^{-1}$ are compared

in Figure 6.4. Three qualitative differences are noticeable directly from the correlation data:

(i) At low temperature, the correlation decreases very rapidly for PMMA adsorbing particles compared to bare particles. This behavior, interestingly, reverses at high temperature where the correlation decreases at much slower rates for the PMMA adsorbing particles.

(ii) Relaxation time for PMMA adsorbing particles at low temperature is much shorter than for bare nanoparticle, whereas at high temperature bare particles relax in shorter times.

(iii) Relaxation time for bare nanoparticles decreases with temperature, while relaxation time for PMMA adsorbing particles increases with temperature. (see Appendix A5 for all temperatures).

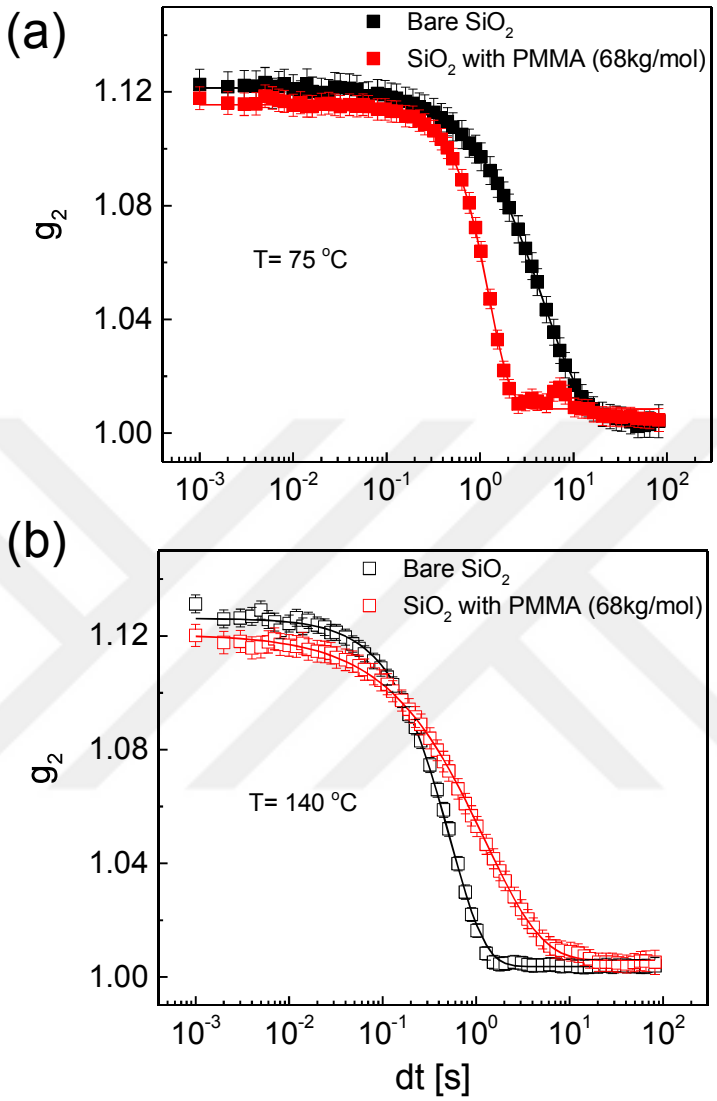

Figure 6. 4. Comparison of auto-correlation functions of particles at (a) 75 ^{o}C and (b) 140 ^{o}C at q = 0.004756 Å^{-1}. Lines are fits to the stretched/compressed exponential function.

The fitting parameters, τ, and β, obtained for 75 ^{o}C are shown in Figure 6.5 and Figure 6.6. Presence of glassy PMMA on nanoparticles changes the relaxation of

particles from diffusive ($\tau \sim q^{-2}$ and β ~ 1) to hyper-diffusive mode, where β is ~ 2. Diffusive motions of bare nanoparticles are expected since particles are large and not affected by the bound PEO layer, thus experience viscosity of PEO matrix. However, with the glassy PMMA on fillers, particle relaxation becomes hyper-diffusive (β > 1). This kind of dynamics is observed in complex fluids near their jammed state suppressing the fast relaxation modes, which leads to larger jump distances resulting in faster than exponential relaxation. In our case, the bound PMMA on nanoparticle surfaces is frozen, thus nanoparticles feel the surrounding glassy PMMA, which results in a highly compressed exponential. The rather surprising result is that how very thin (~2nm, see Chapter 4) glassy PMMA layer on 55 nm particles can affect the particle dynamics in PEO. Our results suggest that dynamics of nanoparticles in polymer melts are primarily determined by local polymer dynamics in the interphase rather than the matrix chains.

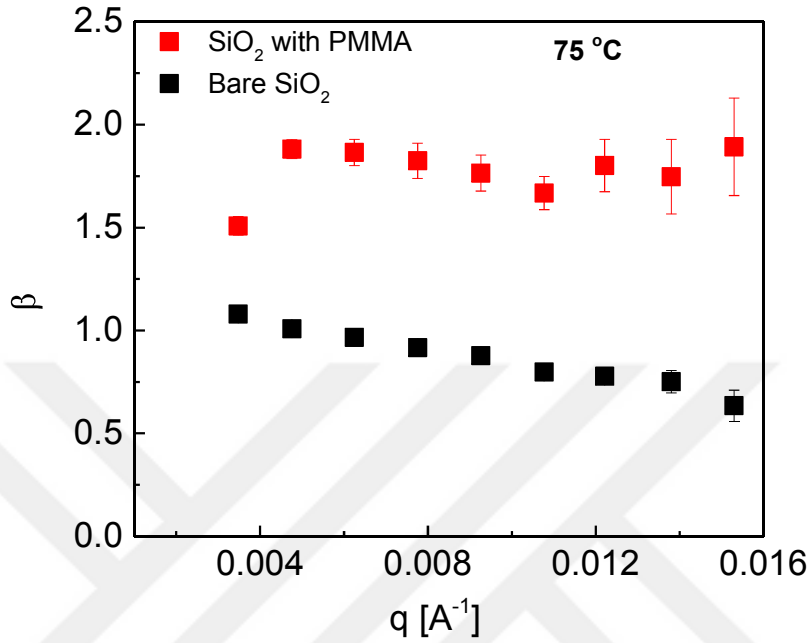

Figure 6. 5. Stretching exponent (β) at different wavevectors at 75 ^{o}C.

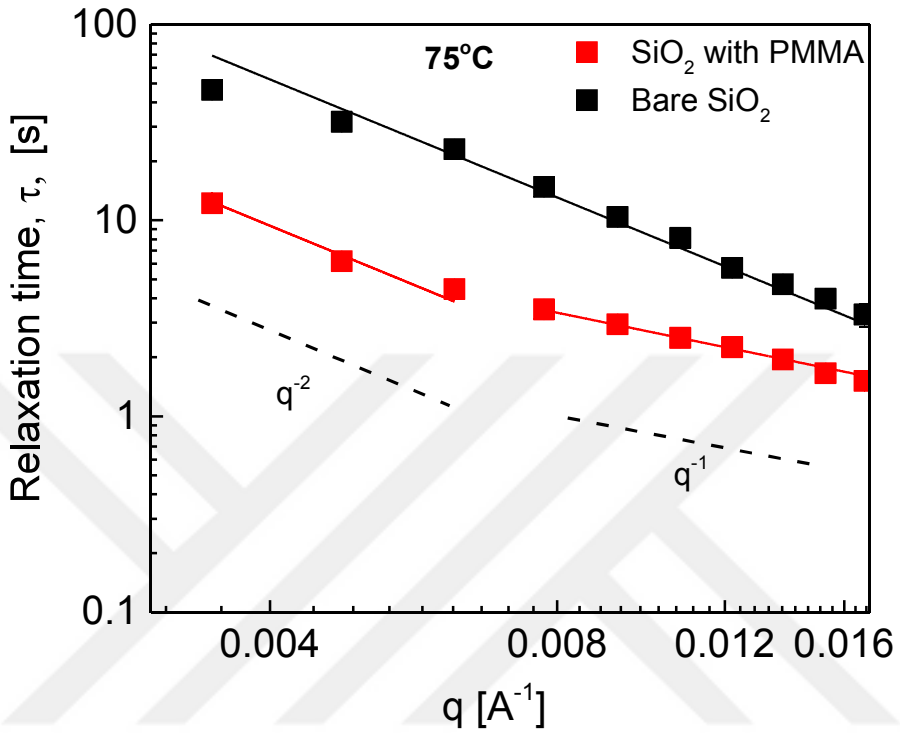

Figure 6. 6. Wavevector dependent relaxation time, τ, for different particles at 75 ^{o}C obtained from the decay of the auto-correlation function.

Figure 6.6. shows the diffusive character of bare particles in PEO at 75 ^{o}C. Particles with glassy PMMA experience slowing down in relaxations and two dynamic modes are seen in Figure 6.6. At high q, relaxations scales with ~ q^{-1}; relaxations at larger lengths (of low q) experience the viscous PEO. While the mechanism of this behavior needs further experiments on particle and polymer dynamics, it is worthy to note that relaxation time for PMMA adsorbed particles increases with temperature contrary to that seen with bare particles (Figure 6.7). The long diffusive relaxation times

for PMMA suggest a viscosity increase within the interphase region at 140 ^{o}C. This is in fact consistent with our rheology results presented in Chapter 5, where we showed that the viscosity increases at high temperatures due to dynamic coupling of PEO with adsorbed PMMA chains. The stretching exponent for bare silica fluctuates near $\beta \sim 1$ (Figure 6.8), while particles with dynamically asymmetric interphases shows a stretched exponential with $\beta \sim 0.75$-0.5. We propose that a slower relaxation in a medium allows multiple relaxation modes which may be caused by possible gradient of mobility around nanoparticles, created by the coupled dynamics between chains of very different relaxation rates. In conclusion, local viscosity gradient (changes) in the asymmetric interphases is the leading factor in controlling the macroscopic mechanical properties.

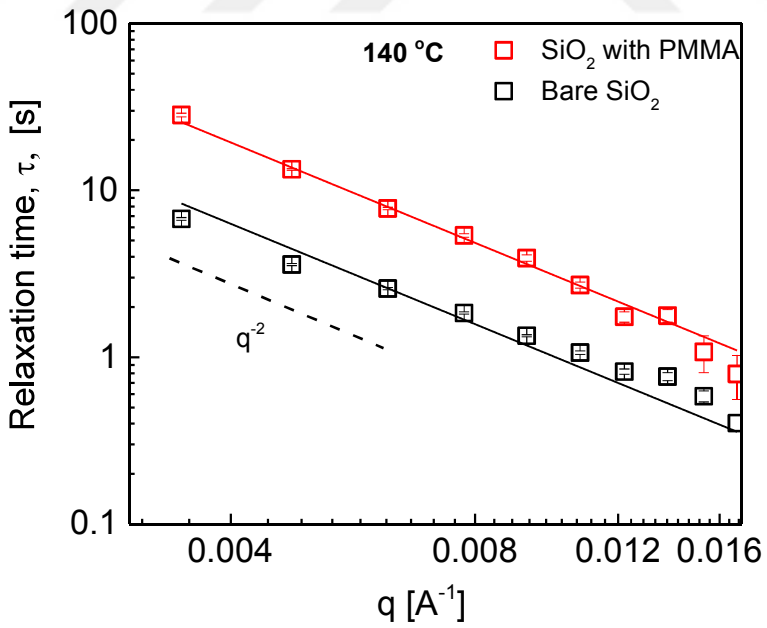

Figure 6. 7. Wavevector dependent relaxation time (τ) for bare and PMMA-adsorbed SiO_2 particles at 140 ^oC, obtained from the decay of the auto-correlation function.

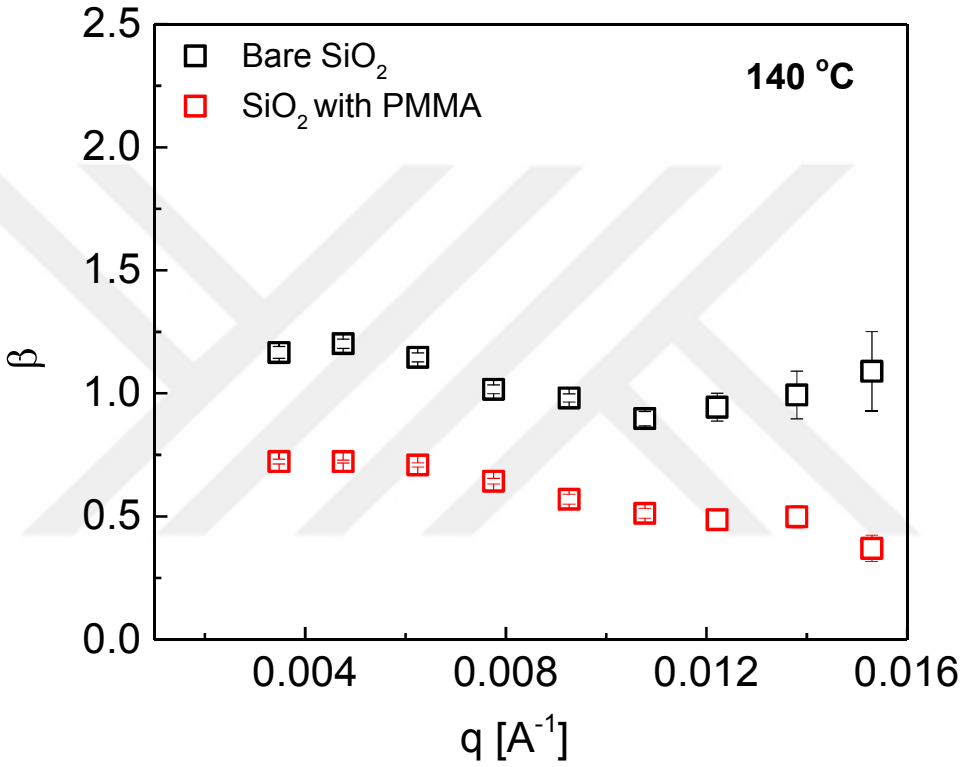

Figure 6. 8. Stretching exponent, β, at different wavevectors for the particles at 140 ^oC.

6.4. Chapter Conclusions and Future Work

In conclusion, we conducted XPCS experiments to probe nanoparticles' motion to understand the nanoscale chain and particle dynamics in a thermally stiffening composite system. By measuring the microscopic dynamics of particles at low and high temperatures, the effect of interphase dynamics on the collective bulk properties can be

probed. Bare SiO_2 nanoparticles follow diffusive dynamics, with $\tau \sim q^{-2}$ scaling and $\beta \sim 1$, and exhibit decreased viscosity with increase in temperature. The presence of glassy bound PMMA unusually results in a hyper-diffusive motion with $\beta \sim 1.5\text{-}2$ and decreased relaxation time compared to bare particles which is attributed to a reduced viscosity of PEO around nanoparticles due to dynamic decoupling of PEO chains from the frozen PMMA at the surface. This slow and stretched dynamics is explained by the dynamic coupling of PEO with slowly relaxing PMMA chains resulting in an increased local viscosity around the particles.

In the coming beamtime, the samples containing different molecular weights of adsorbed PMMA (10 kg/mol, and 200 kg/mol and their bimodal combination) will be tested at 10 ^{o}C increments between 75 ^{o}C and 150 ^{o}C. We will also prepare particles adsorbing bimodal chains of different viscosities to investigate how chain length asymmetry of the bound polymer together with the dynamic asymmetry influence nanoparticle relaxation.

CHAPTER 7

CONCLUSIONS AND OUTLOOK

7.1. Thesis summary

This dissertation uses model attractive polymer nanocomposites with uniform nanoparticle dispersion to underpin the role of interphases between the surface-bound and bulk polymer on polymer relaxation and examines interphase dependent strategies to obtain novel responsive and adaptive mechanical behavior of composites composed of non-responsive components. In particular, this work focuses on bulk rheology of nanocomposites in response to large amplitude shear and varying temperature to modulate particle-polymer interphases. Four different cases of interphases are considered; the main findings and implications from each are summarized and graphically represented below:

Repulsive composite (no interphase): We started with a repulsive nanocomposite (PS-Silica), where formation of interphase is unfavorable. By employing large amplitude oscillatory shear (LAOS) on this composite system, we distinguished polymer and particle contributions to the intra-cycle elastic stress. We found that, in the absence of interphase, particles coalesce under shear flow and re-disperse in quiescent, along with softening and recovery of the stress. Three different deformation regimes appear for the repulsive composites: an initial stress rise, yield-like softening and flow at intermediate strains and strain-stiffening at large strains. The initial stress-rise, attributed to the elasticity of the stiff-particle network, is linearly dependent on nanoparticle loading and

is absent in neat polymer. The strain-stiffening at large strain, which is due to finite extensibility of the polymer chains, is common for all composites and the neat polymer.

A mechanistic model, combining the non-linear deformation models for polymer and particle network, is proposed to explain the intra-cycle response. Deform-rest-deform cycles with varying rest times, together with the structural information and elastic properties at initial, deformed and rest states, further substantiated the distinct role of particle and polymer within an average LAOS cycle. Moreover, we compared the non-linearities obtained from our physical model to the mathematically obtained non-linear parameters, such as Chebyshev polynomial coefficients: the appearance of 5^{th} order harmonics in Fourier Transform Rheology (FTR), may be due to the stiff-particle network contribution at small strains while the 3^{rd} order harmonic is likely because of non-linear chain deformation.

Monomodal interphase: Applying similar LAOS protocol on our model attractive system, PMMA-Silica, results in an atypical self-stiffening after large shear as interphases grow in time due to enhanced topological interactions near nanoparticles. We systematically studied the effects of confinement parameter ($ID/2R_g$), resting time, strain amplitude and particle size. The extent of stiffening strongly depends on ID and resting time; however, the rate of stiffening is found similar for all loadings except for 30 wt% (corresponding to $ID<2R_g$) when ID is normalized to an equivalent diffusion distance. Unlike PS-Silica, this system does not display yield-like intra cycle behavior; thus lacking direct particle contribution. SANS results revealed that averaged chain conformation does not change and remains Gaussian after shearing and resting. FTIR

suggests enhanced loop concentration at stiffened states compared to initial undeformed states. Our results suggests that large periodic shear can be used both as a process to tune the interphases within the same particle dispersion and as a tool to obtain rheological properties while the interphases evolve. The interfacial self-stiffening mechanism has far reaching implications in designing stress-responsive and adaptive bioinspired materials from non-responsive constituents.

Bimodal interphase: The chain-length asymmetry within the bound layer allowed modulating the interfacial entanglements. Instead of using large shear, here, we tuned the interfacial entanglements by adsorbing bimodal PMMA of varying short (unable to form loops) and long (able to form loops) chains on nanoparticles and dispersing them, at same core loading, in monomodal PMMA matrix. Increasing loop forming long chain concentration on nanoparticles resulted in improved elastic moduli in the linear and non-linear properties. This approach is novel since nanocomposite mechanical properties can be tuned within orders of magnitude only by changing the relative fraction of long and short chains without changing polymer-nanoparticles interaction, nanoparticle loading or dispersion state.

*Dynamically asymmetric interphase***:** In the last set of nanocomposites, we investigated the role of relative mobility between adsorbed and matrix chains to interphase formation, hence, the stiffening. We adsorbed nanoparticles with a high-T_g polymer (PMMA) and uniformly dispersed them in a miscible low-T_g matrix (PEO). By modulating the temperature around the T_g of the PMMA, we were able to probe the cases where bound-polymer is glassy and mobile within the same system. These

nanocomposites exhibit an unusual reversible liquid-to-solid transition at temperatures above T_g 's of both polymers. Mechanical adaptivity of PEO nanocomposites to temperatures underlies the existence of dynamically asymmetric bound layers on particles, and more importantly their impact on mechanical behavior, which sets these materials apart from conventional polymer composites that soften upon heating. These results suggest that the mobility of the surface-bound polymer is essential for reinforcement contrary to commonly accepted glassy-layer hypothesis. Finally, we investigated nanoparticles' relaxations through XPCS measurements. We found that the dynamic coupling/decoupling within blend interphase significantly affects relaxation behavior of PMMA adsorbed nanoparticles. Measurements at different temperatures on composites with PMMA suggest anomalous faster particle relaxation compared to conventional bare silica-PEO composites, when dynamic confinement is effective at low temperature. Bulk mechanical properties can, therefore, be explained at the nanoscale level with the interphase dynamics reflecting on particle relaxations as measured in XPCS.

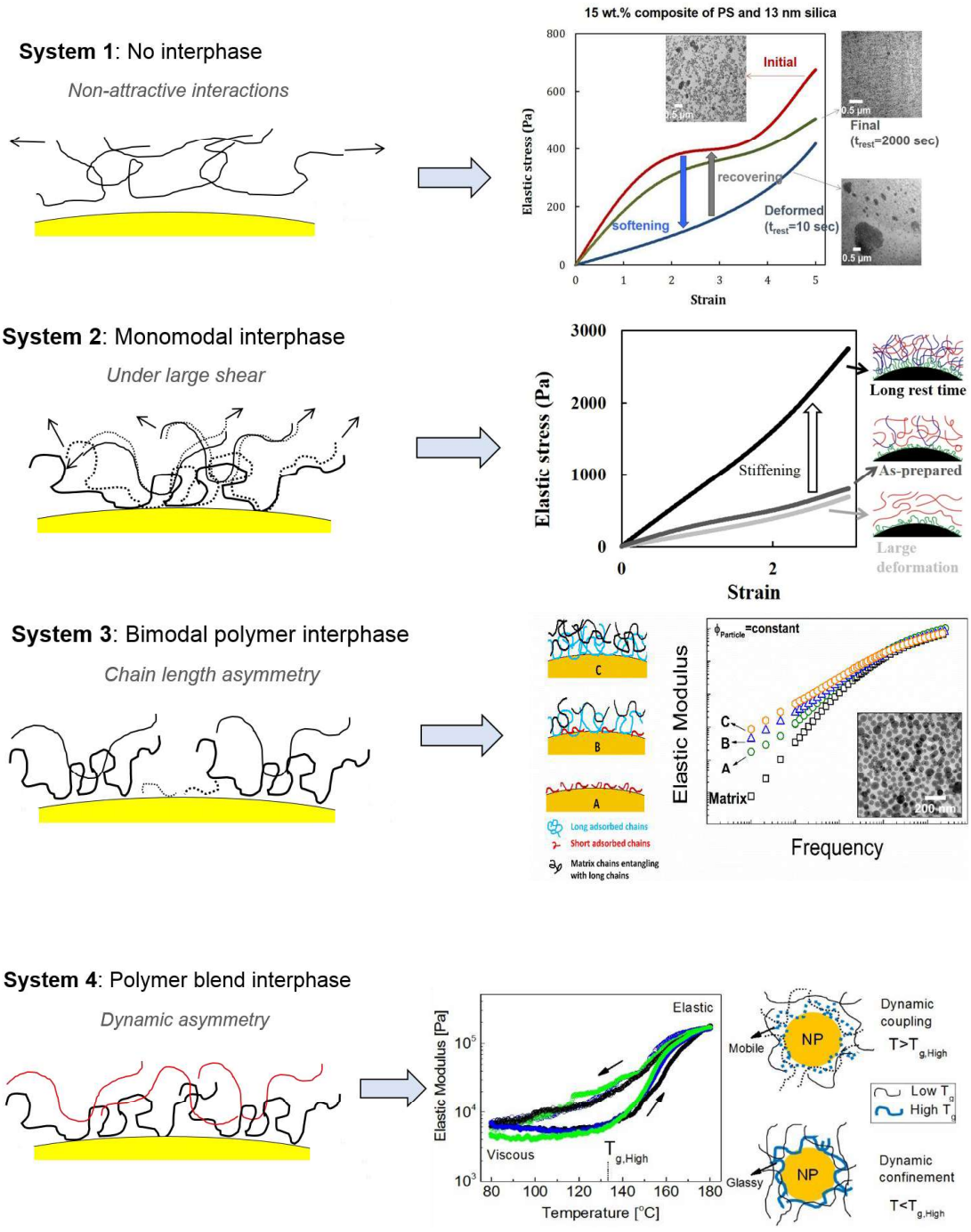

Figure 7. 1. Summary of the systems studied in this thesis and the main findings.

7.2. Suggestions for future work

Interfacial dynamics of polymers are of fundamental importance and many questions are yet to be answered. The mechanisms on the model systems presented here set the stage for further studies on polymer nanocomposites to deeply understand the governing mechanisms and discover new routes for adding more functionalities in these technologically relevant soft materials. Some exciting directions for future work are summarized below:

*Using anisotropic particles***.** We investigated the spherical nanoparticles in our studies to systematically vary the confinement parameters by avoiding direct particle-particle network in attractive system. Using percolated anisotropic nanoparticles at small volume concentrations, breaking of the particle network can result in initial softening that was not seen in well-dispersed PMMA-Silica. It would be interesting to obtain softening-recovery-stiffening within the same material system. In addition, the stress recovery with anisotropic structures would be much different than with the spherical nanoparticles. Furthermore, the anisotropic particles may be oriented under large shear flow as opposed to coalescence of isotropic particles seen in Chapter 2.

Stiffening in polymer-nanoparticle solutions. While we investigated the large shear behavior in melt form, self-stiffening concept can be applied to entangled attractive polymer-nanoparticle solutions. High adsorption/desorption rates of the bound chains may enhance the kinetics of stiffening; however, desorption of surface chains in solution would be a challenging task as viscous forces are highly dominant, causing sliding of rather than stretching. Light cross-linking of the matrix polymer can be an alternative.

Self-stiffening composite hydrogels: Stress-responsive and adaptive hydrogels can be designed to provide on-demand stiffness. For this purpose, PEG (a low M_w analog of PEO) and PVAc miscible system can serve a good model system as PVAc has $T_g \sim 40$ C and miscible with PEG. Plasmonic nanoparticles (e.g. Au) or magnetic nanoparticles, (e.g. Fe_3O_4), can be used to induce local heating via photo-thermal or magnetic heating. In previous work, we showed that temperature at particle surface can exceed 50 ^oC for 50 nm Au nanoparticles in water media.[79] This externally controlled heating can increase the PVAc mobility, thus the overall stiffness of the gel. The main difference of our system is that the stiffening does not cause significant volume change which is commonly observed in other temperature responsive systems.

Longer-time behavior: Our PMMA-Silica study employed a protocol with shear and wait cycles; hence the particle structure did not change in short deformation times. It would be interesting to study particle structuring after very long continuous deformation times as interparticle bridging can induce particle aggregations. Mechanical moduli at different strain levels, from small to large, can be monitored during deformation. TEM and SAXS can be used to evaluate structural evolution. By using various chain lengths as bound and matrix, complete, structure-property relationship can be proposed for linear and non-linear behavior of polymer nanocomposites. Furthermore, such study can reveal the life-time of bound layers of different chain lengths in melt.

Dynamics within interphases of attractive nanocomposites. The origins of mechanical properties of composites can be investigated by tuning their interphases under shear deformation. The confined chains within this transitional region influences the bulk

microscopic relaxation dynamics of polymers. Neutron Spin Echo (NSE) spectroscopy is a useful technique as it measures single chain intermediate dynamic structure factor of polymers. The mobility of the stiffened interphase layer (after applying series of cyclic oscillatory deformations) will be different than the mobility of an adsorbed (bound) layer. The coherent single chain dynamics of a polymer can be investigated using the NSE technique. These measurements yield information on the Rouse dynamics of the polymer, and, if entanglement exist, the reptation tube diameter are obtained. Previous NSE study from Krutyeva et al.[108] on polymer dynamics in confining anodized aluminum oxide (AAO) pores proposed a two-phase model to obtain the extent of the interphase layer. Our nanocomposites are similar to their system, yet the confinement effect is induced by nanoparticles. Therefore, by changing the ID and applying shear-and-rest deformation protocol, growth of the interphase layer can be observed in NSE. The contributions from the interphase and bulk can be obtained from the total scattering $S(Q,t)=f.S_{Rouse}(Q,t)^{free}+(1-f).S(Q,t)^{confined}$ where S(Q,t) is the coherent dynamic structure factor and f is the fraction of bulk chains. At different stages of stiffening, the evolution of the parameter f can be mapped and direct observation of interphase growth after shear can be realized.

Using bimodal matrix chains. Dynamics of bimodal chain lengths of polymers have been well studied in melt and solution form where tube models such as constraint-release and double-reptation successfully apply. Depending on the chain length asymmetry and volume fraction of chains, self-entangling or swelling of chains may occur. In this study, we used bimodal polymer chains only on nanoparticle surface to tune

interphases. An interesting study would be to use bimodal matrix of short and long chains and monomodal bound layer. In particular, when long-chain adsorbed particles are dispersed in bimodal matrix, the exchange of short and long chains on nanoparticle surface may occur. Effective increase of matrix molecular weight during shearing may result in dramatic increase in viscosity. However, after long time annealing, the adsorbed short chains may be replaced with long chains, and composites may soften in quiescent. Such reversible on-demand strengthening may find applications in high strength structural composites as well as biomaterials.

Thin films of dynamically asymmetric interphases. Thin films are commonly used to study the dynamics and structure in confined media. Interfacial thermal-stiffening mechanism presented in this thesis can be explored in thin films to further study the confinement and dynamic coupling effects on glass-transition and aging. Dynamically asymmetric thin polymer blend films have been recently studied in terms of surface segregation of polymer grafted nanoparticles grafted.[171] To the best of our knowledge, there is no thin film work on dynamically asymmetric interphases as in our PEO-Silica-PMMA system in Chapter 5. Thin film analog of our interphases can be created in bilayer form with thin layer of PMMA and PEO with varying thickness. Similarly, PMMA can be replaced with PVAc which has T_g close to ambient temperature; Atomic Force Microscopy (AFM) indentation studies can be employed to probe the temperature dependent elasticity and possible dimension changes, such as buckling or wrinkling.

High-temperature shape-memory. Shape memory polymers have emerged as an important class of responsive soft materials. In order to fix the deformed shape, material

needs to undergo a rapid transition from soft to hard state usually by cooling/heating. Crystallization and glass-transition are widely used to fix the deformed shape. Melting of the crystalline domains or softening above T_g allows recovery of the permanent shape if polymer is elastic at high temperature, which enables a memory. As uncross-linked polymers lose memory at higher temperatures due to viscous flow, the shape-memory remains only effective near T_g. Our thermal-stiffening mechanism can provide an interesting system by allowing on-demand elasticity at temperatures well above T_g of both surface and matrix polymers. Tunable liquid-elastic transition shown in this thesis may allow designing shape memory polymers for multiple temporary shapes.

APPENDICES

Appendix 1

Non-linear (large amplitude) deformation analysis[5]

In a typical small amplitude oscillatory shear experiment, a sinusoidal strain ($\gamma(t) = \gamma_0 \sin\omega t$) with strain amplitude (γ_0) and a frequency (ω) is applied to the sample and resulting stress response is measured. For viscoelastic materials, stress response is also sinusoidal but presents a phase shift with the imposed strain, $\sigma(t)=\sigma_0 \sin(\omega t+\delta)$. In-phase and out-of-phase components of total stress are calculated as $\sigma_{el}(t)=\sigma_0 \sin(\omega t).\cos(\delta)$ and $\sigma_{vis}(t)=\sigma_0 \cos(\omega t).\sin(\delta)$, respectively; and originates from the elastic (solid-like) and viscous (liquid-like) behavior. Correspondingly, elastic (storage) and loss (viscous) moduli are calculated as $G' = (\sigma_0/\gamma_0).\cos(\delta)$ and $G'' = (\sigma_0/\gamma_0).\sin(\delta)$. Similar to the linear viscoelastic measurements, a sinusoidal strain ($\gamma(t) = \gamma_0 \sin\omega t$) is applied in a typical large amplitude oscillatory shear test. The strain amplitude is chosen to be greater than the maximum limit of the linear viscoelasticity ($\gamma_0 > \gamma_{0,linear}$). Stress response to large strains is still periodic but not purely sinusoidal. Thus, elastic and viscous components of total stress cannot be obtained directly as in the case of small periodic deformation. Instead, stress can be decomposed into its purely elastic and viscous components by using geometric arguments.[36] This method utilized the idea that elastic stress should exhibit

---

[5] Senses, Erkan, and Pinar Akcora. "Mechanistic model for deformation of polymer nanocomposite melts under large amplitude shear." Journal of Polymer Science Part B: Polymer Physics 51.9 (2013): 764-771

odd-symmetry with respect to sin(ωt) and even symmetry with respect to cos(ωt) and that viscous stress should exhibit odd-symmetry to cos(ωt) and even symmetry to sin(ωt). Stress decomposition is performed by using MITLaos software[39] and modulus is calculated from the elastic component of the total stress.

Since sample is deformed during 20 cycles of deformation in each step, only initial few cycles contain information about structural evolution in the previous rest time; thus, we analyzed the LAOS response averaged from the stress response between the 2nd and 5th cycles as follows:

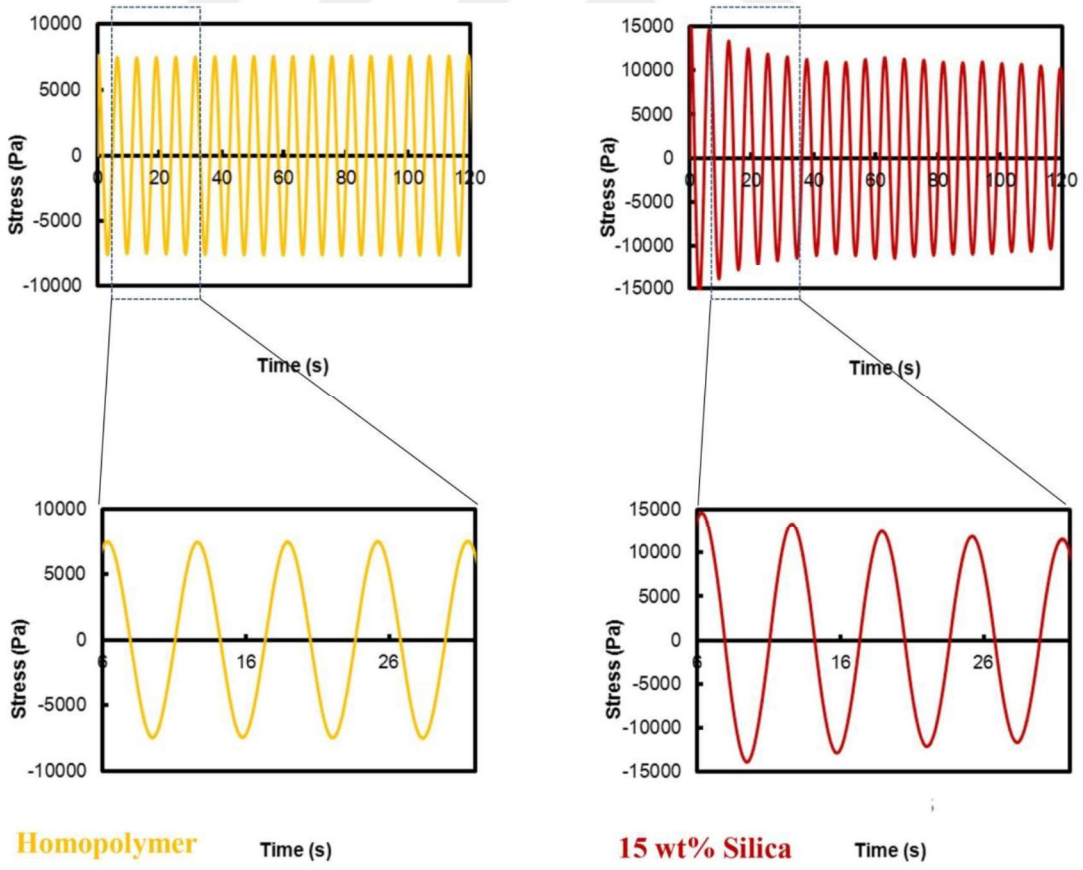

Figure A1. 1. Time evolution of stress response of homopolymer and 15 wt% composition at strain 5 and frequency 1 rad/sec for the initial stage. Enlarged area is the first four cycles used for LAOS analysis of the raw data.

Because the elasticity in particles and polymer chains has energetic and entropic origin, respectively; they contribute deformation at different strain levels. Hence, the local moduli are calculated in the limits of minimum and maximum strains from the elastic stress-strain curves for the averaged LAOS cycle as $\lim_{\gamma \to 0} d\sigma/d\gamma$ and $\sigma(\gamma_0)/\gamma_0$, respectively.

We specifically were very careful about experimental artifacts. We chose parallel-plate for our deformation geometry because cone-and-plate configuration is not suitable for large deformation experiments on polymer composites since any particle aggregates near the center of the cone may cause catastrophic normal forces. We also considered the existence of wall-slipping during the measurements. Wall-slip may occur in particle-filled systems where the particles move towards the plates and create larger shear rates. In the case of wall-slipping, the response mostly comes from the inhomogenous deformation region and total stress decreases considerably. Existence of wall-slip can be checked by measuring the stress responses at different sample thicknesses. For our samples of different thicknesses (ranging from 1.2 mm to 0.6 mm), we have not observed any systematic stress decrease due to sample thickness; on the contrary our samples get stiffen. These experiments revealed that wall-slip do not play a factor in our study. Finally, other instabilities such as shear banding, crazing, edge fracture in sample were

eliminated by employing the deformation at temperatures well above the glass-transition temperature of polymers. Such instabilities are mostly observed at glassy state of samples.

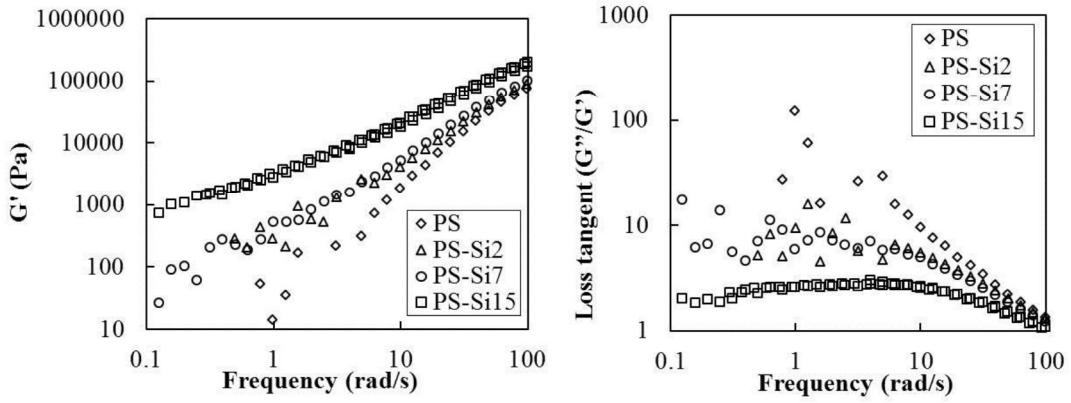

Figure A1. 2. The storage modulus and loss tangent behavior of homopolymer and nanocomposites with 2, 7 and 15 wt% fillers as a function of frequency.

The diffusion constant of non-sticky particles in liquid polymer can be estimated as 8 nm^2/sec at 443 K by using the Stoke-Einstein relation $D = k_BT / 6\pi R\eta$. It should be noted that the diffusivity of the strings would be much smaller than this value. The diffusion length for the longest waiting time (2000 sec) can be approximated by using the relation $x \sim (Dt_{res})^{0.5}$. The characteristic diffusion length is found to be ~ 120 nm. This prediction of diffusion length suggests that segregation of clusters can occur during the long resting times.

Appendix 2

Table A2. 1. Parameters of one-level Beaucage unified fits to the SAXS patterns of the undeformed composites.

Silica wt.%	R_g (nm)	p
2	8.8	4
7	10.3	4
15	7.72	4

Radius of gyration of polymer

Radius of gyration (R_g) of polymer is calculated theoretically as 5.14 nm from the reported[172] Kuhn length (b=1.7 nm) and the molecular weight of a Kuhn monomer (M_0 = 655 g/mole) by using the relationship $R_g=(Nb^2/6)^{0.5}$ for a Gaussian coil where $N = M/M_0$ refers to the number of Kuhn monomers. Thus, the size of the polymer, $2R_g$, is determined to be ~11 nm. This number was confirmed experimentally with the hydrodynamic size of a dilute PMMA solution in MEK measured by DLS and converted to the radius of gyration of a Gaussian coil with the relationship $R_g = 1.54R_h$.

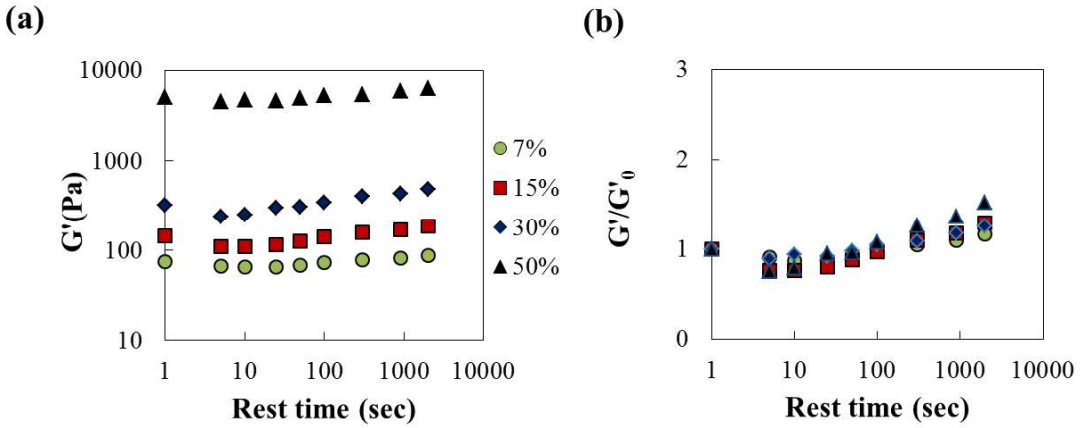

Figure A2. 1. **(a)** Elastic modulus as a function of waiting time for the PMMA-SiO_2 composites prepared with 56 nm particles. (b) Elastic moduli normalized with initial values.

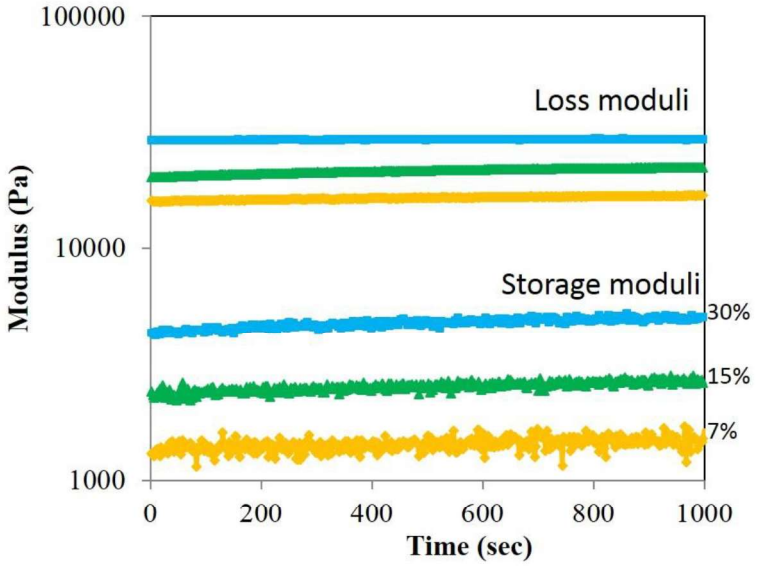

Figure A2. 2. Time-sweep experiments on PMMA-Silica composites performed at 10 rad/sec showing at 210 ^{o}C.

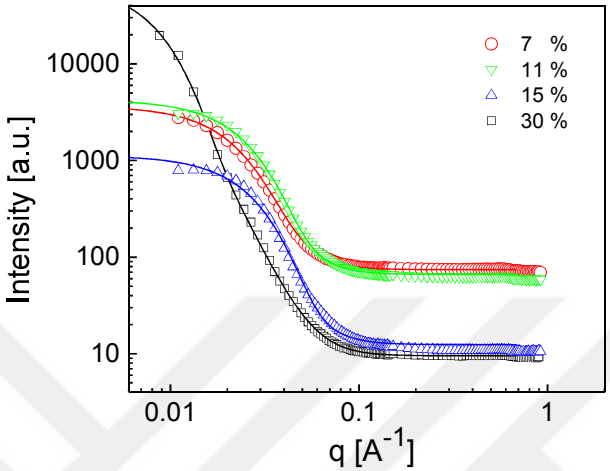

Figure A2. 3. SANS profiles from the hydrogenated composites (with 13 nm silica) after deformation provide the scattering from the silica nanoparticles. Lines represent the one-level Beaucage unified fits.

Table A2. 2. One-level Beaucage unified fits to SANS profiles for the deformed samples.

Silica wt%	R_g (nm)	p
7	7.96	4
11	7.13	4
15	6.53	4
30	21.3	4

Estimation of Reptation time and Diffusion Constant

The reptation time (τ_{rep}) and diffusion coefficient (D_{rep}) of PMMA can be estimated from linear viscoelastic data. Frequency sweep data measured at 210 ^{o}C is shown in Figure A2.3. The entanglement (plateau) modulus (G_N) is 200 kPa at this temperature. The zero shear viscosity (η) is determined to be 3800 Pa.s from the low frequency plateau of the complex viscosity (η^*) as shown in the inset. Reptation time is related to G_N and η with the relationship $\eta = (\pi^2/12)\, \tau_{rep}\, G_N$. Thus, τ_{rep} is calculated 0.02 sec at 210 ^{o}C.

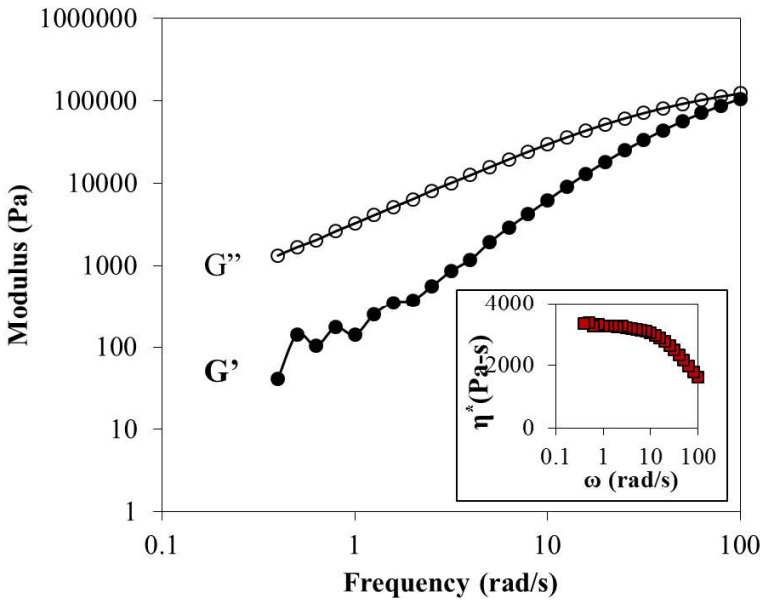

Figure A2. 4. Frequency sweep experiment for PMMA homopolymer at 210 ^{o}C. The inset shows the complex modulus.

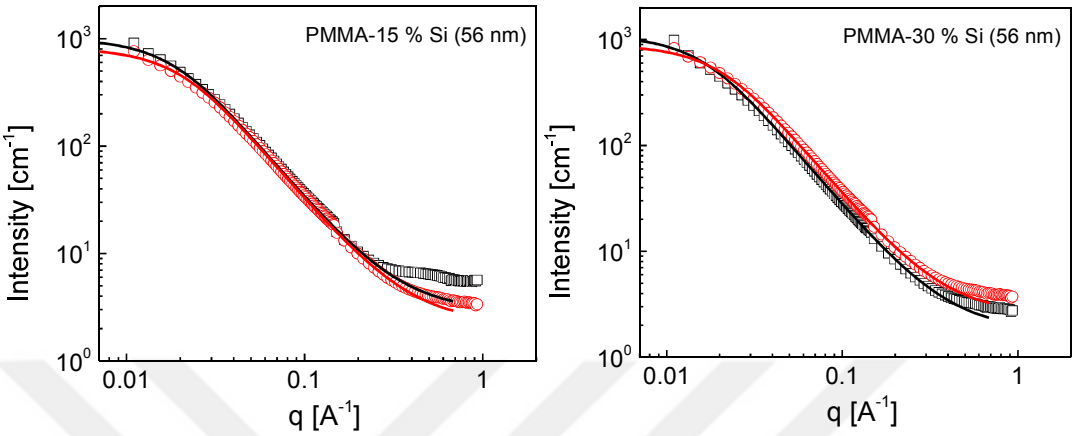

Figure A2. 5. Small-angle neutron scattering (SANS) profiles of the PMMA nanocomposites with (a) 13 nm and (b) 56 nm SiO_2 before (black symbols) and after (red symbols) deformation. The fits are the Debye functions. Error bars are smaller than the symbol sizes.

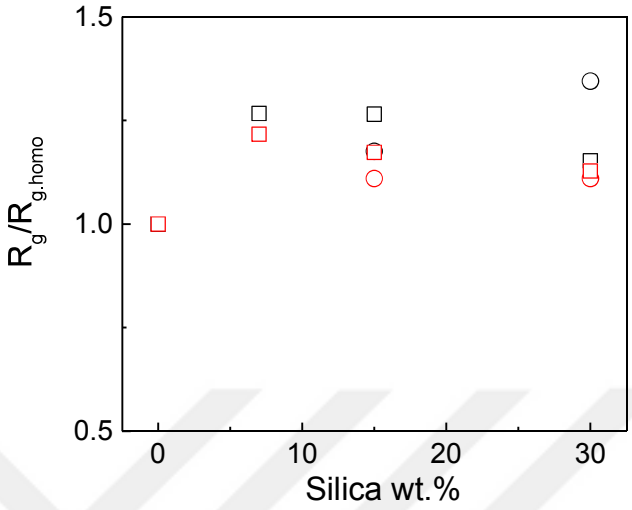

Figure A2. 6. Radius of gyration of the polymer determined from the Debye fits as a function of particle concentration. The filled and open symbols represent undeformed and deformed composites, respectively. The circles are for 13 nm and triangles are for 56 nm particles.

Further discussion on non-linear (large amplitude) deformation method

We specifically were very careful about experimental artifact due to sample deformation and rheological instabilities. We chose parallel-plate for our deformation geometry because cone-and-plate configuration is not suitable for large deformation experiments on polymer composites since any particle aggregates near the center of the cone may cause catastrophic normal forces. It was also shown that multiplying the stress in LAOS by a factor of 3/2 may account for shear inhomogenities in parallel plates [173,174]. The non-linear response from parallel plate and cone-and-plate geometries were compared by using series of non-linear deformation experiments by Ewoldt et al.[175] and it

was shown that the response is almost identical for both. This is due to the fact that the non-linear response dominates quickly for the parallel plate geometry. We also considered the existence of wall-slipping during the measurements. Wall-slip may occur in particle-filled systems where particles move towards the plates and create larger shear rates at the plates. The response mostly comes from the inhomogenous deformation region and the total stress decreases considerably. The existence of wall-slip can be checked by measuring the stress responses at different sample thicknesses. For our samples of different thicknesses (ranging from 1.2 mm to 0.6 mm), we have not observed any systematic stress decrease due to sample thickness. In fact, our samples get stiffen and the TEM images in Figure A2.2 shows no change in particle dispersion. Furthermore, we conducted the same deformation-resting protocol on another 15 wt% composition with a 25 mm parallel plate geometry with 0.8 mm thick sample and observed that the same stiffening behavior as shown in Figure A2.5. These experiments revealed that sample thickness or other surface effects such as wall-slip do not play a factor in our study. Finally, other instabilities such as shear banding, crazing, edge fracture in sample were eliminated by employing the deformation at temperatures well above the glass-transition temperature of polymers. Such instabilities are mostly observed at glassy state of samples where the elastic stress dominates.

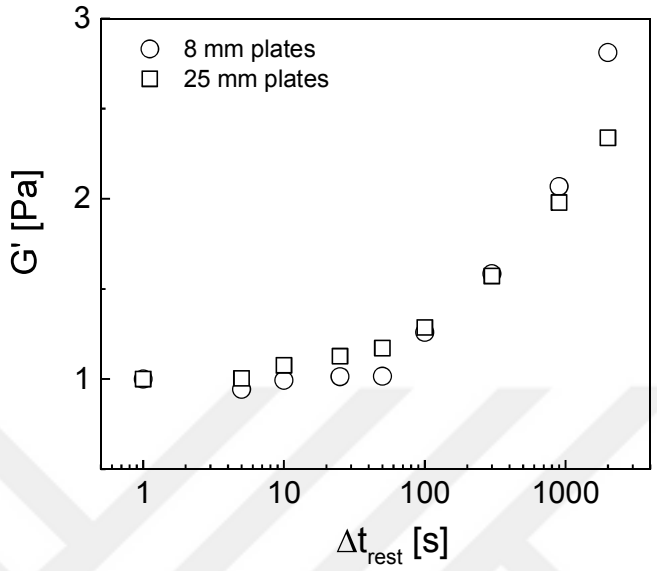

Figure A2. 7. Comparison of elastic modulus normalized to the initial modulus as a function of waiting time for PMMA-Si (15 wt%) composites with 13 nm particles deformed using 8-mm and 25-mm parallel-plate geometries.

Appendix 3

Table A3. 1. Fitting parameters for the interphase contribution to the complex viscosity.

	For Interphase		
Φ_L	η_0	K	m
1	24489.91	2.72921	0.72
0.95	38762.75	2.15014	0.72
0.85	24625.23	1.7276	0.72
0.7	30103.35	1.94921	0.72
0.3	11480.2	1.60544	0.72
0	4417.614	0.10134	0.72

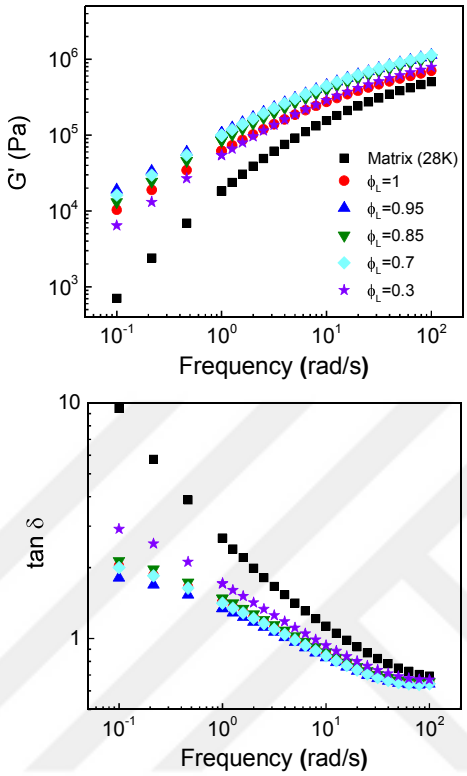

Figure A3. 1. Linear elastic modulus and loss tangent of nanocomposites with 12/2.6 kg/mol PMMA blend adsorbed on SiO_2 (55 nm) nanoparticles dispersed in 28 kg/mol PMMA (T = 210 ^oC). Particle loading is 30 wt% in all composites.

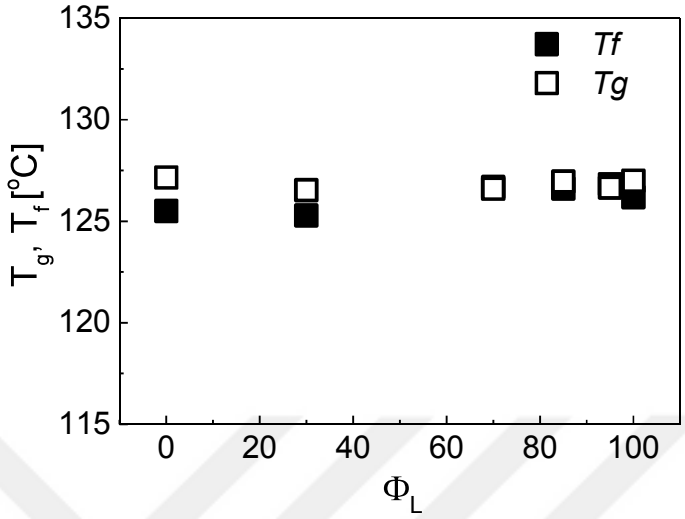

Figure A3. 2. Glass transition (T_g) and fictive (T_f) temperatures of nanocomposites with varying long chain concentration in bound layer.

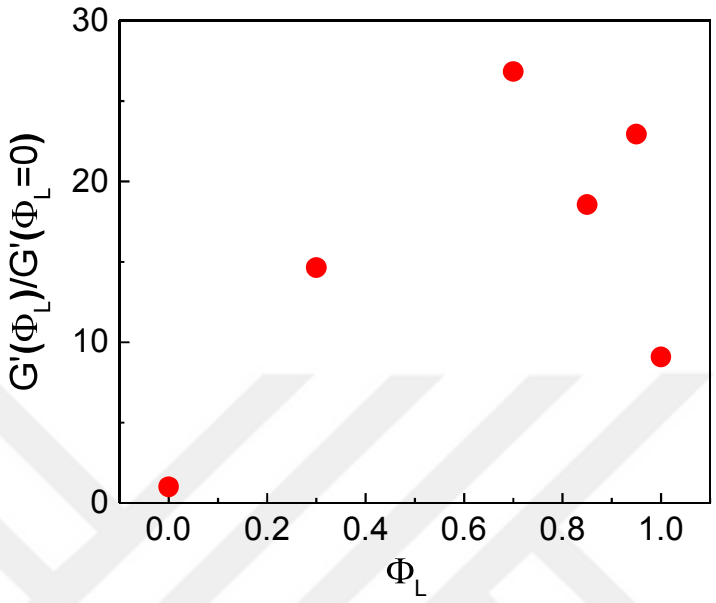

Figure A3. 3. Ratio of the storage moduli for composites with different long chain concentrations on particle surfaces relative to all-short chains adsorbed particles. The ratios are determined from the linear viscoelastic data at 0.1 rad/sec frequency.

Appendix 4

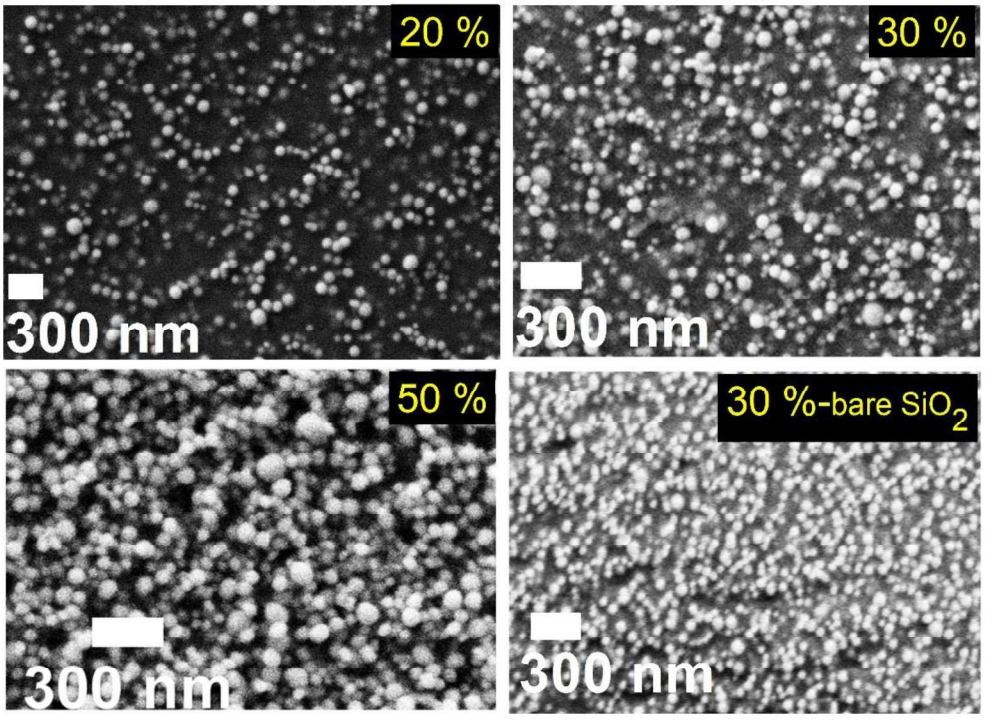

Figure A4. 1. SEM images showing well dispersion of polymer coated particles in PEO matrix. 20 wt%, 30 wt% and 50 wt% SiO_2 adsorbing 68 kg/mol PMMA and 30 wt% bare SiO_2.

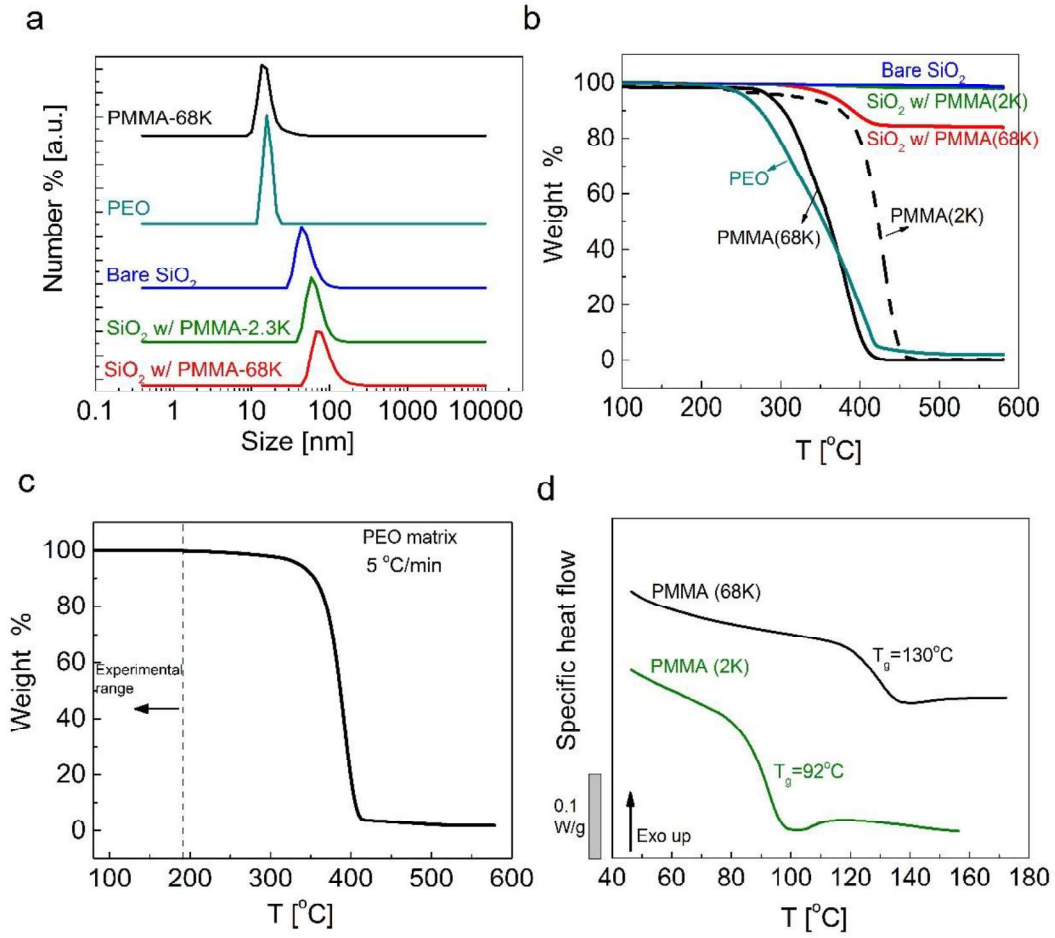

Figure A4. 2. Dynamic light scattering (DLS) and thermal characterization of pure components and polymer adsorbed particles**. (a)** Hydrodynamic sizes of PEO, PMMA, bare SiO_2 and polymer adsorbed SiO_2 in dilute solutions. (**b)** Adsorbed polymer masses on nanoparticles are measured by a thermal gravimetric analyzer (TGA). **(c)** Weight loss (degradation) profile of neat PEO with temperature at 5 ^{o}C/min. (**d)** Glass transition temperatures of 2 and 68 kg/mol PMMA homopolymers using a DSC.

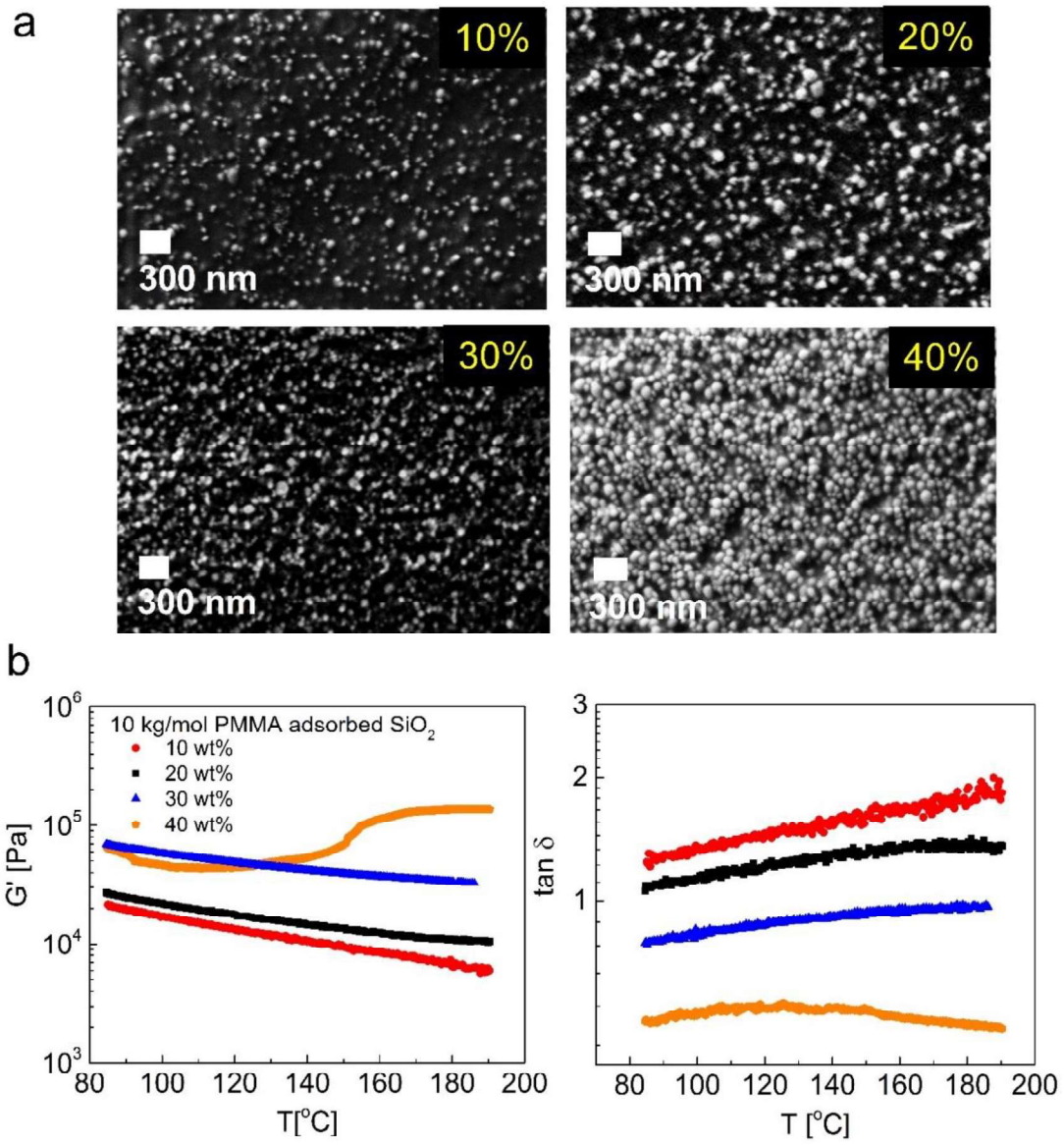

Figure A4. 3. Stiffening response from short adsorbed chains. **(a)** Dispersions in composites with 9.6 kg/mol (Đ: 1.06) PMMA adsorbed SiO_2 are shown in SEM images. **(b)** Elastic moduli and loss tangents of composites with 9.6 kg/mol PMMA adsorbed SiO_2 with increasing temperature.

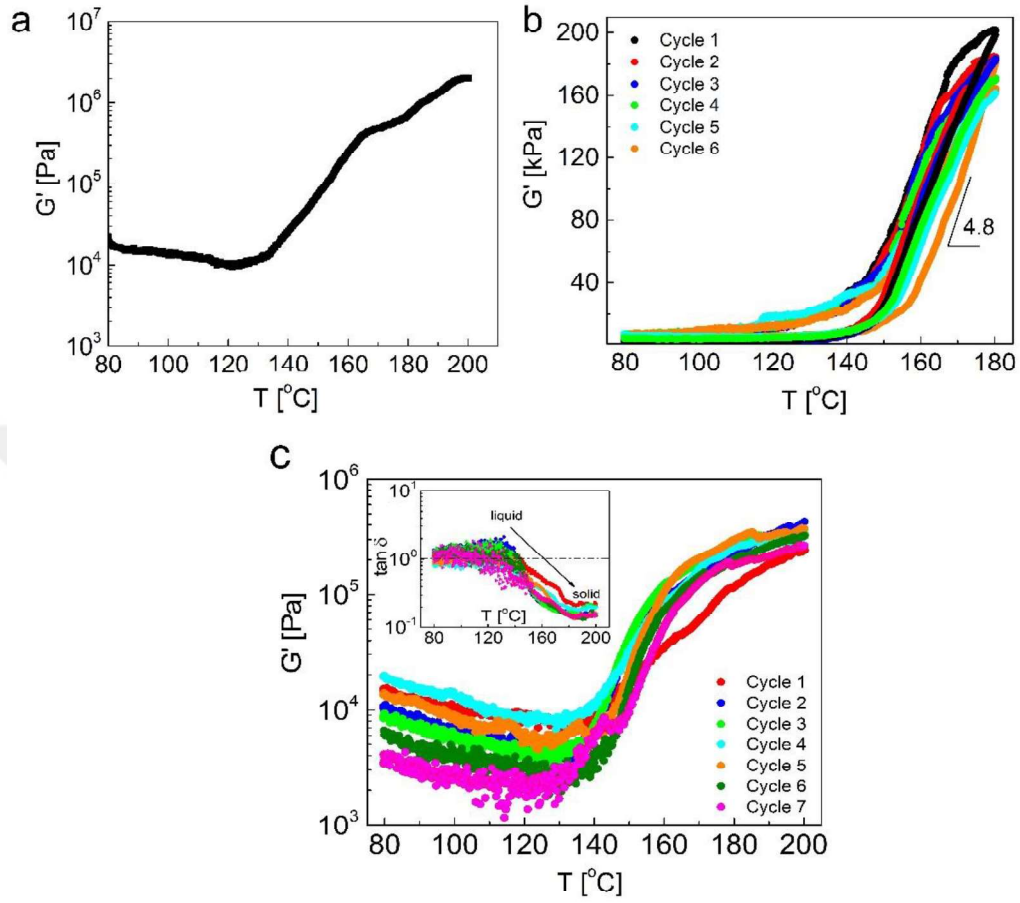

Figure A4. 4. Elastic response to thermal cycles. **(a)** Elastic modulus for 50 wt% composite in response to temperature presents stiffening behavior under particle induced confinement ($ID/2R_g<1$). **(b)** Complex viscosity behavior of 40 wt% composite upon heating and cooling cycles (5 ^{o}C/min) follows the same heating and cooling paths (reversible) with clear hysteresis around $T_{g,PMMA}$. **(c)** Elastic moduli response to temperature is similar to a rubber-like behavior.

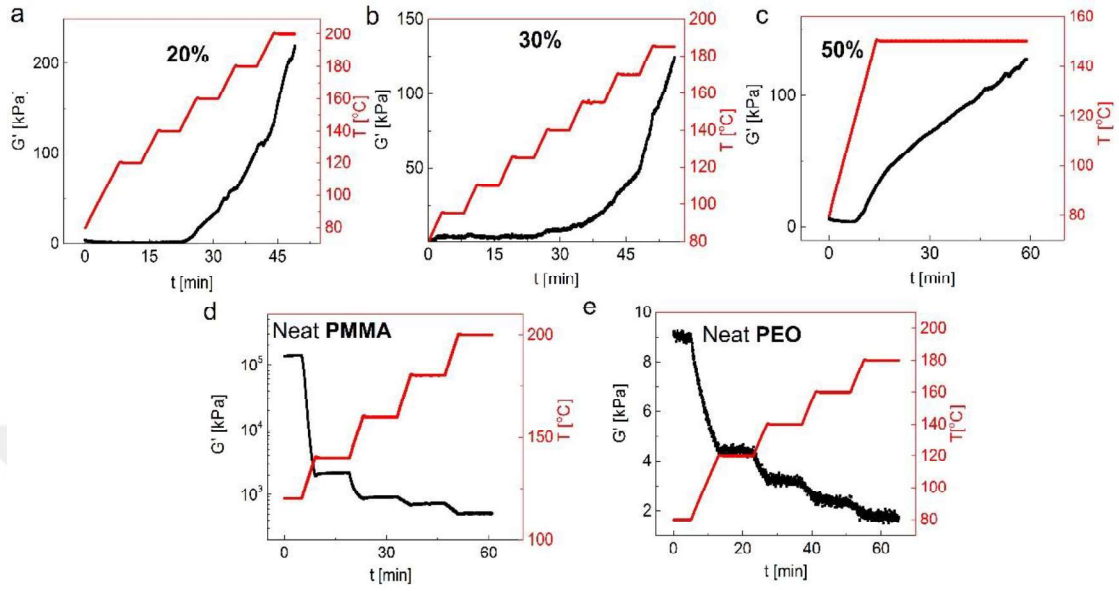

Figure A4. 5. Growth rate of elastic moduli with stepwise temperature changes. **(a)** 20 wt% and **(b)** 30 wt% composite upon heating above T_g of PMMA. (**c)** Isothermal response of a 50 wt% composite at a longer waiting time. (**d)** Step temperature response of pure PMMA at the same temperature range shows that PMMA reaches its equilibrium modulus readily at each temperature step. (**e)** Step-temperature response of pure PEO and PMMA shows a similar equilibrium modulus at isotherms.

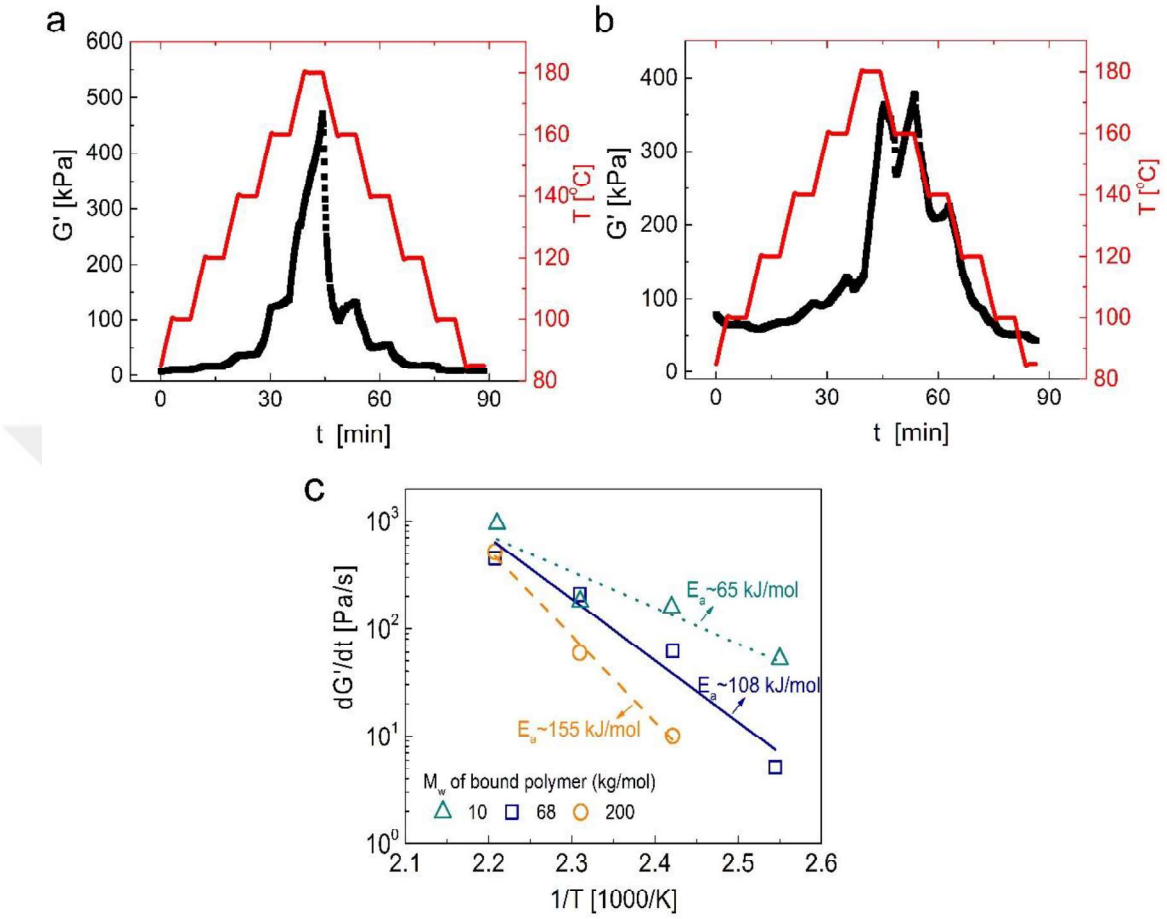

Figure A4. 6. Chain length effect on isothermal stiffening. Step-temperature response of a 40 wt% composite with **(a)** 200 kg/mol and **(b)** 10kg/mol bound PMMA on particles. **(c)** Corresponding aging rates are shown on an Arrhenius graph for a 40 wt% composite adsorbed with 10, 68 and 200 kg/mol PMMA.

A literature Review on blend miscibility and dynamics

This section reviews major experimental and theoretical works on miscible polymer blend systems, specifically for the PEO-PMMA system, in terms of their contribution to miscibility and component dynamics below and above T_g of the blend.

PEO-PMMA miscibility has been investigated by various researchers. Cimmino et al.[143,176] determined that the blend (with $M_{w,PMMA}$ = 130K and $M_{w,PEO}$ ~ 20 K) is an LCST type with the critical temperature 350 ^oC. Fernandes[144] et al. also observed the miscibility of 300K PEO and 100K PMMA up to LCST temperature of 230 ^oC by cloud point analysis and glass-transition measurements. Although early studies suggested that the blend is miscible down to room temperature, NMR[177] and PALS[178] studies later reported heterogeneous domain size of 2-50 nm in amorphous phase at room temperature. Following this, Hopkinson et al.[179] reported an UCST temperature 47-77 ^oC for blends having M_w~120K at blend ratios 0.1-0.27. The main difficulty for determining the miscibility arises from the low interaction parameter, χ. Russell[141] determined χ for this system (with $M_{w,PMMA}$ = 145K and $M_{w,PEO}$ ~ 125K) to be ~ (-1 to -5) $x10^{-3}$ and independent of temperature, suggesting that the entropic contributions dominate. This negative and negligibly small interaction parameter is also the main reason for possible concentration fluctuations, which has been used to explain the dynamic heterogeneities and unusual dynamics of PEO in the blend. Most recently, Richter[142] confirmed by SANS that the PEO-PMMA system (with M_w ~ 25 K) is an LCST type with T_{LCST} = 400 ^oC at 25% PEO concentration in the blend. They also reported that the PEO crystallizes below 57 ^oC at concentrations above 30 vol. %. Dynamic studies on PEO-PMMA blends are

mainly limited to PMMA-rich systems with PEO concentrations lower than 30%. This is mainly because PEO crystallized above 30% concentration.

Note that the early studies on miscibility of the blends relied on the presence of two glass transitions. It was generally assumed that two distinct peaks arise from immiscibility of the components; however, this rule of thumb was later shown to be unreliable by Lodge and coworkers[180,181]. Two T_g's are shown to exist in many homogenous blend systems, including homopolymer blends of different molecular weights and polymer-solvent mixtures creating significant ΔT_g. In the case of PEO-PMMA blend, $\Delta T_g \sim 180\ ^oC$, and two distinct T_g's are expected to appear at intermediate blend ratios. Each T_g corresponds to T_g of each component that is modified by blending. This is often called effective glass transition, $T_{g,eff}$, by Lodge and McLeish [139]. Briefly, the Lodge-McLeish model proposes that a segment of one-type in a blend is locally enriched by its own kind due to chain connectivity. The properties that are composition dependent, such as T_g, would thus reflect this self-concentration effect. The length scale for this is on the order of Kuhn length of the chain. This model appears to well-explain the experimentally observed two glass transitions in many other polymer blends (e.g. PS/PVME[182], PI/PVE[183]) and even in solutions (e.g. PS/toluene, PS/dibutyl, and PS/dimethyl phthalate[184]). In our system, PMMA is only adsorbed on nanoparticle surface with the ratio of its weight to silica ~ 15/85 (for 68 kg/mol PMMA on 55-nm silica). For the largest concentration of silica, which is 50 wt% in nanocomposite, the ratio of PMMA that is mixed by PEO at the interphase is less than 10%. Thus, the matrix

phase significantly suppresses the PMMA signal in DCS traces. This explains the lack of $T_{g,PMMA}$ in our composites.

Dynamic Heterogeneities and Anomalies in Miscible Polymer Blends

PEO-PMMA system has been widely investigated because of its complete miscibility (negligible interaction parameter) and large T_g difference, $\Delta T_g \sim 180\ ^oC$ (dynamic asymmetry). Despite an earlier rheological study[185], Colby[186] reported on an 80% PMMA-PEO blend that the time-temperature-superposition fails to describe the overall relaxation behavior. He attributed this unusual behavior to separate friction coefficients corresponding to each component and their dissimilar temperature dependence[187]. Following this report (~ 25 years ago), various different techniques, such as rheometry, Nuclear Magnetic Resonance, dielectric spectroscopy and Quasi-elastic Neutron Scattering, have been employed to investigate the relaxation behavior of individual components in their blends relative to their pure forms at various composition and temperature ranges.

There are mainly three hypotheses to explain the origin of dynamic heterogeneities. Those are mostly based on the local composition differences that are different than the bulk composition. In one theory, the thermally driven concentration fluctuations[138] may be the cause. This is more relevant to systems having small χ and large ΔT_g , which is the case for PEO-PMMA. The length scale is ~10nm around $T_{g,\ blend}$. The Lodge-McLeish model[139], as explained in previous section, relies on the self-concentration effect due to chain connectivity. The relevant length scale in this theory is

~1 nm, Kuhn length. Recently, a coupling theory by Ngai and Roland[140] has been used to explain the dynamic features.

Early ^{1}H-NMR work by Lartigue et al.[188] reported that the dynamics of PEO is highly affected by the presence of PMMA but locally PEO remains highly mobile at the blend T_g, revealing highly heterogenous dynamics in the blend near its T_g. Lutz et al.[136] studied, via D-NMR, the PEO local dynamics in the blend for PEO concentrations ranging from 0.5% to 30%. Remarkably, they found that PEO segmental dynamics is 12 orders of magnitude faster than that of PMMA at the blend T_g. More interestingly, the dynamics is nearly independent of blend composition even in the infinitely dilute regime, where the compositional fluctuations are ruled out. They attribute this behavior to the lack of side groups in PEO, which facilities local relaxation of PEO segments within frozen PMMA matrix. Ngai and Roland[140] later explained this observation by a coupling model which combines the effect of chemical and compositional heterogeneities, and intermolecular cooperatively. Similarly, Kumar et al.[189] further modified the Lodge-McLeish model by combining concentration fluctuations with the self-concentration and found a good agreement between the model and the available data for various miscible blends systems, such as PI/PVE, PBO/PVE and PVME/PS.

Jin et al.[190] investigated the cooperative segmental relaxation in 80-20 PMMA-PEO blend using dielectric spectroscopy and found that the glassy blend undergoes significant aging at room temperature.

Maranas and co-workers[191] compared dynamic results from linear blends and diblock copolymers with similar composition, which would result in different

intermolecular packing. While chain connectivity model nicely explained the PMMA's behavior, the PEO dynamics could not be simply explained within this framework. In QENS experiments[192], they further tested the validity of the chain-connectivity, coupling models and found that PEO dynamics may not be explained by a single length scale as suggested by Lodge-McLeish model.

Lodge et al.[133,193] used rheological approach to obtain the terminal relaxation behavior of PEO. Simply a high M_w tracer PEO is used in low M_w unentangled blend to see its effect on terminal relaxation behavior. They also found that the Lodge-McLeish model may not explain the PEO dynamics in the blend. Moreover, their results were insensitive to chain end groups.

Lorthioir and Sy [149,194] first proposed the idea of dynamic confinement based on dielectric spectroscopy results on PVDF/PVME and PVAc/PEO systems which also exhibit large asymmetry in T_g's. Dynamic confinement is induced by the high T_g component at temperatures close to or below its T_g in the blend on the low T_g components. Chains with high T_g are considered to be frozen in the timescale of low-T_g component so that the fast component is highly mobile within confined regions. The length-scale of this confinement is found to be ~1 nm [151] by QENS and molecular dynamics simulations.

Moreno et al.[195] showed via bead-spring model based simulation that the large size disparity between monomers induces anomalous dynamic decoupling and behaves similar to entangling system despite the fact that the chains were in the non-entangling

regime. The authors attributed this to memory effects. These observations were later realized in NSE experiments in PEO-PMMA blends[196].

Colmenero et al. recently studies the effect of cross-linking on the chain dynamics by using PMMA soft nanoparticles dispersed in PEO matrix. [145,197] It was found in blend with 75 wt% PMMA[145] that PEO dynamics above T_g of PMMA becomes extremely slow by two orders of magnitude slower than pure PEO. Furthermore, chains deviate from Gaussian behavior in this regime and dynamics becomes slower as the temperature is further increased. Authors attribute this behavior to local traps of PEO chains in the loops near the surface of the nanoparticles.[145]

Most PEO-PMMA blend studies focused on the confinement and anomalous dynamics in the low temperature regime. It was shown by Cohen-Addad[198] that at high temperatures, relaxation time of the PEO-PMMA blend linearly depends on temperature which suggest formation of entanglement network. Mechanical response of our bulk composites at high temperatures is also linearly dependent on temperature. We attribute this to the entanglements between the interphase chains and bulk PEO. As dynamic coupling occurs in other miscible blend systems and homopolymers, the observed thermo-stiffening mechanism in our study should apply to other dynamically asymmetric blend systems and bimodal homopolymers.

Appendix 5

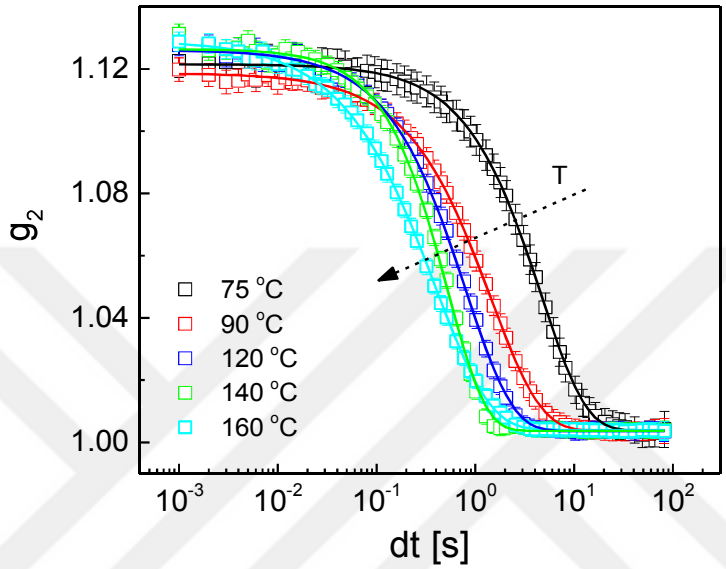

Figure A5. 1. Auto-correlation functions of bare SiO_2 in PEO at temperatures showing a monotonic dependence on temperature.

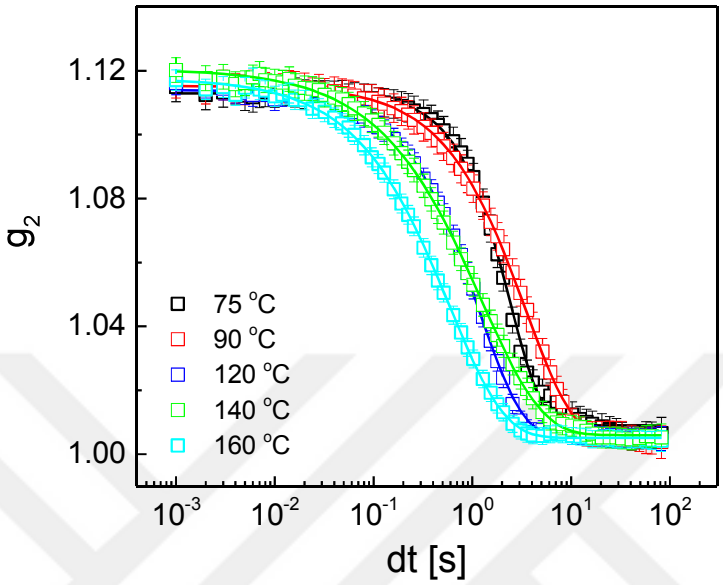

Figure A5. 2. Auto-correlation functions of PMMA (68 kg/mol) adsorbed SiO_2 in PEO display a non-monotonic dependence on temperature.

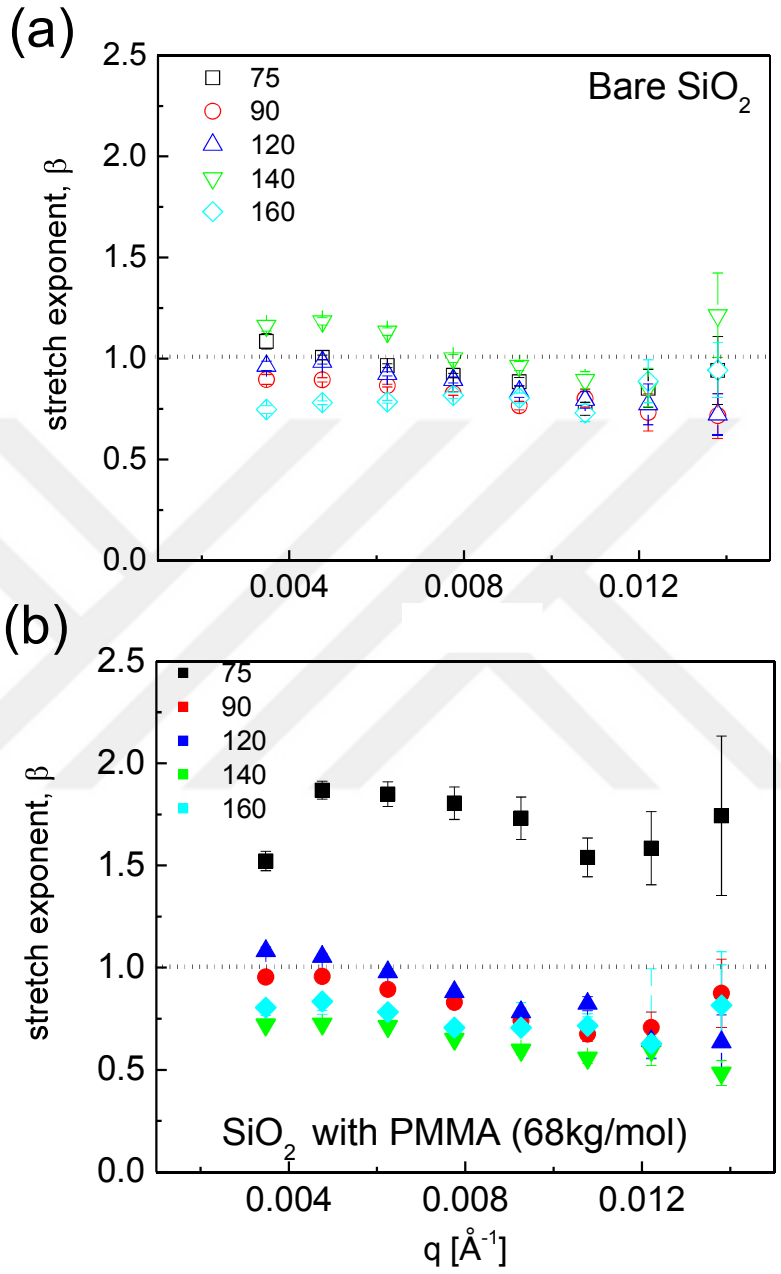

Figure A5. 3. Stretched exponent, β, at different wavevectors for **(a)** bare SiO_2 and **(b)** PMMA (68 kg/mol) adsorbed SiO_2 at different temperatures.

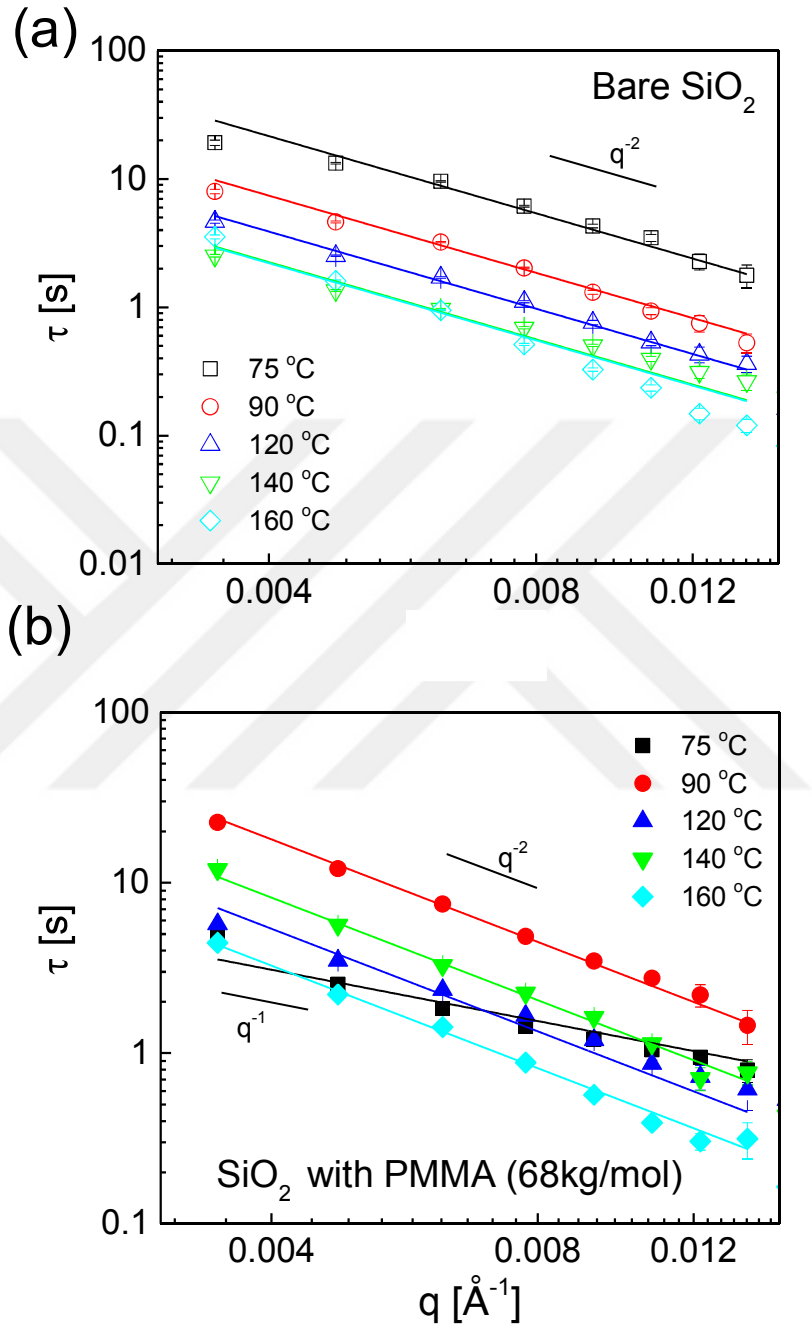

Figure A5. 4. Wavevector dependent relaxation time,τ , for **(a)** bare SiO_2 and **(b)** PMMA (68kg/mol) adsorbed SiO_2 at different temperatures.

References

1 Gusev, A. A. Micromechanical mechanism of reinforcement and losses in filled rubbers. *Macromolecules* **39**, 5960-5962 (2006).

2 Sternstein, S. & Zhu, A.-J. Reinforcement mechanism of nanofilled polymer melts as elucidated by nonlinear viscoelastic behavior. *Macromolecules* **35**, 7262-7273 (2002).

3 Winey, K. I. & Vaia, R. A. Polymer nanocomposites. *MRS bulletin* **32**, 314-322 (2007).

4 Tjong, S. Structural and mechanical properties of polymer nanocomposites. *Materials Science and Engineering: R: Reports* **53**, 73-197 (2006).

5 Li, Y., Tao, P., Viswanath, A., Benicewicz, B. C. & Schadler, L. S. Bimodal surface ligand engineering: the key to tunable nanocomposites. *Langmuir* **29**, 1211-1220 (2012).

6 Ounaies, Z., Park, C., Wise, K., Siochi, E. & Harrison, J. Electrical properties of single wall carbon nanotube reinforced polyimide composites. *Composites Science and Technology* **63**, 1637-1646 (2003).

7 Du, F., Scogna, R. C., Zhou, W., Brand, S., Fischer, J. E. & Winey, K. I. Nanotube networks in polymer nanocomposites: rheology and electrical conductivity. *Macromolecules* **37**, 9048-9055 (2004).

8 Pramanik, N., Mishra, D., Banerjee, I., Maiti, T. K., Bhargava, P. & Pramanik, P. Chemical synthesis, characterization, and biocompatibility study of hydroxyapatite/chitosan phosphate nanocomposite for bone tissue engineering applications. *International journal of biomaterials* **2009** (2009).

9 Xu, H., Cheng, L., Wang, C., Ma, X., Li, Y. & Liu, Z. Polymer encapsulated upconversion nanoparticle/iron oxide nanocomposites for multimodal imaging and magnetic targeted drug delivery. *Biomaterials* **32**, 9364-9373 (2011).

10 Croce, F., Appetecchi, G., Persi, L. & Scrosati, B. Nanocomposite polymer electrolytes for lithium batteries. *Nature* **394**, 456-458 (1998).

11 Kim, S., Jinschek, J. R., Chen, H., Sholl, D. S. & Marand, E. Scalable fabrication of carbon nanotube/polymer nanocomposite membranes for high flux gas transport. *Nano letters* **7**, 2806-2811 (2007).

12 Jouault, N., Moll, J. F., Meng, D., Windsor, K., Ramcharan, S., Kearney, C. & Kumar, S. K. Bound polymer layer in nanocomposites. *ACS Macro Letters* **2**, 371-374 (2013).

13 Harton, S. E., Kumar, S. K., Yang, H., Koga, T., Hicks, K., Lee, H., Mijovic, J., Liu, M., Vallery, R. S. & Gidley, D. W. Immobilized polymer layers on spherical nanoparticles. *Macromolecules* **43**, 3415-3421 (2010).

14 Sargsyan, A., Tonoyan, A., Davtyan, S. & Schick, C. The amount of immobilized polymer in PMMA SiO2 nanocomposites determined from calorimetric data. *European Polymer Journal* **43**, 3113-3127 (2007).

15 Ciprai, D., Jacob, K. & Tannenbaum, R. Characterization of polymer nanocomposite interphase and its impact on mechanical properties. *Macromolecules* **39**, 6565-6573 (2006).

16 Krutyeva, M., Wischnewski, A., Monkenbusch, M., Willner, L., Maiz, J., Mijangos, C., Arbe, A., Colmenero, J., Radulescu, A., Holderer, O., Ohl, M. & Richter, D. Effect of nanoconfinement on polymer dynamics: Surface layers and interphases. *Physical Review Letters* **110** (2013).

17 Rittigstein, P., Priestley, R. D., Broadbelt, L. J. & Torkelson, J. M. Model polymer nanocomposites provide an understanding of confinement effects in real nanocomposites. *Nature Materials* **6**, 278-282 (2007).

18 Papon, A., Montes, H., Hanafi, M., Lequeux, F., Guy, L. & Saalwöchter, K. Glass-transition temperature gradient in nanocomposites: Evidence from nuclear magnetic resonance and differential scanning calorimetry. *Physical Review Letters* **108** (2012).

19 Kim, S. Y. & Zukoski, C. F. Molecular weight effects on particle and polymer microstructure in concentrated polymer solutions. *Macromolecules* **46**, 6634-6643 (2013).

20 Li, Y., Kröger, M. & Liu, W. K. Dynamic structure of unentangled polymer chains in the vicinity of non-attractive nanoparticles. *Soft Matter* **10**, 1723-1737 (2014).

21 Senses, E. & Akcora, P. Mechanistic model for deformation of polymer nanocomposite melts under large amplitude shear. *Journal of Polymer Science Part B: Polymer Physics* **51**, 764-771 (2013).

22 Senses, E. & Akcora, P. An interface-driven stiffening mechanism in polymer nanocomposites. *Macromolecules* **46**, 1868-1874 (2013).

23 Senses, E. & Akcora, P. Tuning mechanical properties of nanocomposites with bimodal polymer bound layers. *RSC Advances* **4**, 49628-49634 (2014).

24 Heinrich, G. & Klüppel, M. Recent advances in the theory of filler networking in elastomers. *Advances in Polymer Science* **160**, 1-44 (2002).

25 Zhu, Z., Thompson, T., Wang, S. Q., Von Meerwall, E. D. & Halasa, A. Investigating linear and nonlinear viscoelastic behavior using model silica-particle-filled polybutadiene. *Macromolecules* **38**, 8816-8824 (2005).

26 Moll, J. F., Akcora, P., Rungta, A., Gong, S., Colby, R. H., Benicewicz, B. C. & Kumar, S. K. Mechanical reinforcement in polymer melts filled with polymer grafted nanoparticles. *Macromolecules* **44**, 7473-7477 (2011).

27 Akcora, P., Kumar, S. K., Moll, J., Lewis, S., Schadler, L. S., Li, Y., Benicewicz, B. C., Sandy, A., Narayanan, S., Ilavsky, J., Thiyagarajan, P., Colby, R. H. & Douglas, J. F. "Gel-like" mechanical reinforcement in polymer nanocomposite melts. *Macromolecules* **43**, 1003-1010 (2010).

28 Merabia, S., Sotta, P. & Long, D. R. A microscopic model for the reinforcement and the nonlinear behavior of filled elastomers and thermoplastic elastomers (Payne and Mullins Effects). *Macromolecules* **41**, 8252-8266 (2008).

29 Heinrich, G., Klüppel, M. & Vilgis, T. A. Reinforcement of elastomers. *Current Opinion in Solid State and Materials Science* **6**, 195-203 (2002).

30 Zhu, A. J. & Sternstein, S. S. Nonlinear viscoelasticity of nanofilled polymers: Interfaces, chain statistics and properties recovery kinetics. *Composites Science and Technology* **63**, 1113-1126 (2003).

31 Jouault, N., Vallat, P., Dalmas, F., Said, S., Jestin, J. & Boue, F. Well-dispersed fractal aggregates as filler in polymer-silica nanocomposites: Long-range effects in rheology. *Macromolecules* **42**, 2031-2040 (2009).

32 Papon, A., Merabia, S., Guy, L., Lequeux, F., Montes, H., Sotta, P. & Long, D. R. Unique nonlinear behavior of nano-filled elastomers: From the onset of strain softening to large amplitude shear deformations. *Macromolecules* **45**, 2891-2904 (2012).

33 Hyun, K., Nam, J., Wilhellm, M., Ahn, K. & Lee, S. Large amplitude oscillatory shear behavior of PEO-PPO-PEO triblock copolymer solutions. *Rheologica Acta* **45**, 239-249, doi:10.1007/s00397-005-0014-x (2006).

34 Ng, T. S. K., McKinley, G. H. & Ewoldt, R. H. Large amplitude oscillatory shear flow of gluten dough: A model power-law gel. *Journal of Rheology* **55**, 627-654 (2011).

35 Hyun, K. & Wilhelm, M. Establishing a new mechanical nonlinear coefficient Q from FT-rheology: First investigation of entangled linear and comb polymer model systems. *Macromolecules* **42**, 411-422 (2009).

36 Cho, K. S., Hyun, K., Ahn, K. H. & Lee, S. J. A geometrical interpretation of large amplitude oscillatory shear response. *Journal of Rheology* **49**, 747-758 (2005).

37 Hyun, K., Wilhelm, M., Klein, C. O., Cho, K. S., Nam, J. G., Ahn, K. H., Lee, S. J., Ewoldt, R. H. & McKinley, G. H. A review of nonlinear oscillatory shear tests: Analysis and application of large amplitude oscillatory shear (LAOS). *Progress in Polymer Science (Oxford)* **36**, 1697-1753 (2011).

38 Jouault, N., Vallat, P., Dalmas, F., Said, S., Jestin, J. & Boué, F. Well-Dispersed Fractal Aggregates as Filler in Polymer− Silica Nanocomposites: Long-Range Effects in Rheology. *Macromolecules* **42**, 2031-2040 (2009).

39 Ewoldt, R. H., Hosoi, A. E. & McKinley, G. H. New measures for characterizing nonlinear viscoelasticity in large amplitude oscillatory shear. *Journal of Rheology* **52**, 1427-1458 (2008).

40 Christensen, R. M. Observations on the definition of yield stress. *Acta Mechanica* **196**, 239-244 (2008).

41 Rubinstein, M. & Panyukov, S. Elasticity of Polymer Networks. *Macromolecules* **35**, 6670-6686 (2002).

42 Storm, C., Pastore, J. J., MacKintosh, F. C., Lubensky, T. C. & Janmey, P. A. Nonlinear elasticity in biological gels. *Nature* **435**, 191-194 (2005).

43 Marko, J. F. & Siggia, E. D. Stretching DNA. *Macromolecules* **28**, 8759-8770, doi:10.1021/ma00130a008 (1995).

44 Dobrynin, A. V. & Carrillo, J. M. Y. Universality in nonlinear elasticity of biological and polymeric networks and gels. *Macromolecules* **44**, 140-146 (2011).

45 Buehler, M. J. & Ackbarow, T. Fracture mechanics of protein materials. *Materials Today* **10**, 46-58 (2007).

46 Ji, B. & Gao, H. Mechanical properties of nanostructure of biological materials. *Journal of the Mechanics and Physics of Solids* **52**, 1963-1990 (2004).

47 Wang, T., Liu, D., Lian, C., Zheng, S., Liu, X. & Tong, Z. Large deformation behavior and effective network chain density of swollen poly(N-isopropylacrylamide)-Laponite nanocomposite hydrogels. *Soft Matter* **8**, 774-783 (2012).

48 Carrillo, J. M. Y. & Dobrynin, A. V. Effect of the electrostatic interactions on stretching of semiflexible and biological polyelectrolytes. *Macromolecules* **43**, 2589-2604 (2010).

49 Cai, L. H., Panyukov, S. & Rubinstein, M. Mobility of nonsticky nanoparticles in polymer liquids. *Macromolecules* **44**, 7853-7863 (2011).

50 Wilhelm, M. Fourier‐Transform Rheology. *Macromolecular materials and engineering* **287**, 83-105 (2002).

51 Senses, E. & Akcora, P. Mechanistic model for deformation of polymer nanocomposite melts under large amplitude shear. *Journal of Polymer Science, Part B: Polymer Physics* **51**, 764-771 (2013).

52 Solomon, M. J., Almusallam, A. S., Seefeldt, K. F., Somwangthanaroj, A. & Varadan, P. Rheology of polypropylene/clay hybrid materials. *Macromolecules* **34**, 1864-1872 (2001).

53 Krishnamoorti, R. & Yurekli, K. Rheology of polymer layered silicate nanocomposites. *Current Opinion in Colloid & Interface Science* **6**, 464-470 (2001).

54 Letwimolnun, W., Vergnes, B., Ausias, G. & Carreau, P. J. Stress overshoots of organoclay nanocomposites in transient shear flow. *Journal of non-newtonian fluid mechanics* **141**, 167-179 (2007).

55 Hyun, K., Ahn, K. H., Lee, S. J., Sugimoto, M. & Koyama, K. Degree of branching of polypropylene measured from Fourier-transform rheology. *Rheologica Acta* **46**, 123-129 (2006).

56 Reinheimer, K., Grosso, M., Hetzel, F., Kübel, J. & Wilhelm, M. Fourier Transform Rheology as an innovative morphological characterization technique for the emulsion volume average radius and its distribution. *Journal of colloid and interface science* (2012).

57 Reinheimer, K., Grosso, M. & Wilhelm, M. Fourier Transform Rheology as a universal non-linear mechanical characterization of droplet size and interfacial tension of dilute monodisperse emulsions. *Journal of colloid and interface science* **360**, 818-825 (2011).

58 Langela, M., Wiesner, U., Spiess, H. & Wilhelm, M. Microphase reorientation in block copolymer melts as detected via FT rheology and 2D SAXS. *Macromolecules* **35**, 3198-3204 (2002).

59 Hyun, K. & Wilhelm, M. Establishing a new mechanical nonlinear coefficient Q from FT-rheology: first investigation of entangled linear and comb polymer model systems. *Macromolecules* **42**, 411-422 (2008).

60 Cho, K. S., Hyun, K., Ahn, K. H. & Lee, S. J. A geometrical interpretation of large amplitude oscillatory shear response. *Journal of Rheology* **49**, 747 (2005).

61 Ewoldt, R. H., Hosoi, A. & McKinley, G. H. New measures for characterizing nonlinear viscoelasticity in large amplitude oscillatory shear. *Journal of Rheology* **52**, 1427 (2008).

62 Rogers, S. A., Erwin, B. M., Vlassopoulos, D. & Cloitre, M. A sequence of physical processes determined and quantified in LAOS: Application to a yield stress fluid. *Journal of Rheology* **55**, 435-458 (2011).

63 Rogers, S., Kohlbrecher, J. & Lettinga, M. The molecular origin of stress generation in worm-like micelles, using a rheo-SANS LAOS approach. *Soft Matter* **8**, 7831-7839 (2012).

64 Dobrynin, A. V. & Carrillo, J.-M. Y. Universality in Nonlinear Elasticity of Biological and Polymeric Networks and Gels. *Macromolecules* **44**, 140-146, doi:10.1021/ma102154u (2010).

65 Fetters, L. J., Lohse, D. J., Milner, S. T. & Graessley, W. W. Packing length influence in linear polymer melts on the entanglement, critical, and reptation molecular weights. *Macromolecules* **32**, 6847-6851 (1999).

66 Stuart, M. A. C., Huck, W. T. S., Genzer, J., Müller, M., Ober, C., Stamm, M., Sukhorukov, G. B., Szleifer, I., Tsukruk, V. V., Urban, M., Winnik, F., Zauscher, S., Luzinov, I. & Minko, S. Emerging applications of stimuli-responsive polymer materials. *Nature Materials* **9**, 101-113 (2010).

67 Hsu, L., Weder, C. & Rowan, S. J. Stimuli-responsive, mechanically-adaptive polymer nanocomposites. *Journal of Materials Chemistry* **21**, 2812-2822 (2011).

68 Kushner, A. M., Vossler, J. D., Williams, G. A. & Guan, Z. A biomimetic modular polymer with tough and adaptive properties. *Journal of the American Chemical Society* **131**, 8766-8768 (2009).

69 Shanmuganathan, K., Capadona, J. R., Rowan, S. J. & Weder, C. Stimuli-responsive mechanically adaptive polymer nanocomposites. *ACS Applied Materials and Interfaces* **2**, 165-174 (2010).

70 Mendes, P. M. Stimuli-responsive surfaces for bio-applications. *Chemical Society Reviews* **37**, 2512-2529 (2008).

71 Capadona, J. R., Shanmuganathan, K., Tyler, D. J., Rowan, S. J. & Weder, C. Stimuli-responsive polymer nanocomposites inspired by the sea cucumber dermis. *Science* **319**, 1370-1374 (2008).

72 Bonderer, L. J., Studart, A. R. & Gauckler, L. J. Bioinspired design and assembly of platelet reinforced polymer films. *Science* **319**, 1069-1073 (2008).

73 Wang, E., Lee, S. H. & Lee, S. W. Elastin-like polypeptide based hydroxyapatite bionanocomposites. *Biomacromolecules* **12**, 672-680 (2011).

74 Mickiewicz, R. A., Mayes, A. M. & Knaack, D. Polymer-calcium phosphate cement composites for bone substitutes. *Journal of Biomedical Materials Research* **61**, 581-592 (2002).

75 Fantner, G. E., Adams, J., Turner, P., Thurner, P. J., Fisher, L. W. & Hansma, P. K. Nanoscale ion mediated networks in bone: Osteopontin can repeatedly dissipate large amounts of energy. *Nano Letters* **7**, 2491-2498 (2007).

76 Fantner, G. E., Hassenkam, T., Kindt, J. H., Weaver, J. C., Birkedal, H., Pechenik, L., Cutroni, J. A., Cidade, G. A. G., Stucky, G. D., Morse, D. E. & Hansma, P. K. Sacrificial bonds and hidden length dissipate energy as mineralized fibrils separate during bone fracture. *Nature Materials* **4**, 612-616 (2005).

77 Crowe, J. A. & Genzer, J. Creating responsive surfaces with tailored wettability switching kinetics and reconstruction reversibility. *Journal of the American Chemical Society* **127**, 17610-17611 (2005).

78 Koerner, H., White, T. J., Tabiryan, N. V., Bunning, T. J. & Vaia, R. A. Photogenerating work from polymers. *Materials Today* **11**, 34-42 (2008).

79 Zhu, Z., Senses, E., Akcora, P. & Sukhishvili, S. A. Programmable light-controlled shape changes in layered polymer nanocomposites. *ACS nano* **6**, 3152-3162 (2012).

80 Black, A. L., Lenhardt, J. M. & Craig, S. L. From molecular mechanochemistry to stress-responsive materials. *Journal of Materials Chemistry* **21**, 1655-1663 (2011).

81 Zheng, X., Sauer, B. B., Van Alsten, J. G., Schwarz, S. A., Rafailovich, M. H., Sokolov, J. & Rubinstein, M. Reptation Dynamics of a Polymer Melt near an Attractive Solid Interface. *Physical Review Letters* **74**, 407-410 (1995).

82 Lin, E. K., Kolb, R., Satija, S. K. & Wu, W.-l. Reduced Polymer Mobility near the Polymer/Solid Interface as Measured by Neutron Reflectivity. *Macromolecules* **32**, 3753-3757, doi:10.1021/ma9814604 (1999).

83 Källrot, N., Dahlqvist, M. & Linse, P. Dynamics of polymer adsorption from bulk solution onto planar surfaces. *Macromolecules* **42**, 3641-3649 (2009).

84 Smith, G. D., Bedrov, D. & Borodin, O. Structural relaxation and dynamic heterogeneity in a polymer melt at attractive surfaces. *Physical Review Letters* **90**, 2261031-2261034 (2003).

85 Kim, S. Y., Schweizer, K. S. & Zukoski, C. F. Multiscale structure, interfacial cohesion, adsorbed layers, and thermodynamics in dense polymer-nanoparticle mixtures. *Physical Review Letters* **107** (2011).

86 Riggleman, R. A., Toepperwein, G., Papakonstantopoulos, G. J., Barrat, J. L. & De Pablo, J. J. Entanglement network in nanoparticle reinforced polymers. *Journal of Chemical Physics* **130** (2009).

87 Erk, K. A., Henderson, K. J. & Shull, K. R. Strain stiffening in synthetic and biopolymer networks. *Biomacromolecules* **11**, 1358-1363 (2010).

88 Carey, B. J., Patra, P. K., Ci, L., Silva, G. G. & Ajayan, P. M. Observation of dynamic strain hardening in polymer nanocomposites. *ACS Nano* **5**, 2715-2722 (2011).

89 Hong, R. Y., Fu, H. P., Zhang, Y. J., Liu, L., Wang, J., Li, H. Z. & Zheng, Y. Surface-modified silica nanoparticles for reinforcement of PMMA. *Journal of Applied Polymer Science* **105**, 2176-2184 (2007).

90 Gam, S., Meth, J. S., Zane, S. G., Chi, C., Wood, B. A., Winey, K. I., Clarke, N. & Composto, R. J. Polymer diffusion in a polymer nanocomposite: Effect of nanoparticle size and polydispersity. *Soft Matter* **8**, 2512-2520 (2012).

91 Chen, J., Zheng, G., Xu, L., Zhang, J., Lu, Y., Xue, G. & Yang, Y. Spectroscopic study of ordered structures of atactic poly(methyl methacrylate) freeze-extracted from poly(ethylene glycol) solution. *Polymer* **42**, 4459-4462 (2001).

92 González-Benito, J. & González-Gaitano, G. Interfacial conformations and molecular structure of PMMA in PMMA/silica nanocomposites. Effect of high-energy ball milling. *Macromolecules* **41**, 4777-4785 (2008).

93 Natarajan, B., Neely, T., Rungta, A., Benicewicz, B. C. & Schadler, L. S. Thermomechanical properties of bimodal brush modified nanoparticle composites. *Macromolecules* **46**, 4909-4918 (2013).

94 Guan, L.-Z., Wan, Y.-J., Gong, L.-X., Yan, D., Tang, L.-C., Wu, L.-B., Jiang, J.-X. & Lai, G.-Q. Toward effective and tunable interphases in graphene oxide/epoxy composites by grafting different chain lengths of polyetheramine onto graphene oxide. *Journal of Materials Chemistry A* **2**, 15058-15069 (2014).

95 Jouault, N., Lee, D., Zhao, D. & Kumar, S. K. Block-copolymer-mediated nanoparticle dispersion and assembly in polymer nanocomposites. *Advanced Materials* **26**, 4031 (2014).

96 Fetters, L., Lohse, D. & Colby, R. in *Physical properties of polymers handbook* 447-454 (Springer, 2007).

97 Ewoldt, R. H., Hosoi, A. & McKinley, G. H. New measures for characterizing nonlinear viscoelasticity in large amplitude oscillatory shear. *Journal of Rheology (1978-present)* **52**, 1427-1458 (2008).

98 Wang, L.-M., Velikov, V. & Angell, C. Direct determination of kinetic fragility indices of glassforming liquids by differential scanning calorimetry: Kinetic versus thermodynamic fragilities. *The Journal of chemical physics* **117**, 10184-10192 (2002).

99 Rubinstein, M. & Colby, R. H. *Polymer physics*. (OUP Oxford, 2003).

100 Guinier, A. *X-ray diffraction: in crystals, imperfect crystals, and amorphous bodies*. (Courier Dover Publications, 2013).

101 Dijt, J. C., Stuart, M. A. C. & Fleer, G. J. Competitive adsorption kinetics of polymers differing in length only. *Macromolecules* **27**, 3219-3228 (1994).

102 Fu, Z. & Santore, M. M. Kinetics of competitive adsorption of PEO chains with different molecular weights. *Macromolecules* **31**, 7014-7022 (1998).

103 Santore, M. M. Dynamics in adsorbed homopolymer layers: Understanding complexity from simple starting points. *Current opinion in colloid & interface science* **10**, 176-183 (2005).

104 Johnson, H. E. & Granick, S. New mechanism of nonequilibrium polymer adsorption. *SCIENCE.* **255**, 966-968 (1992).

105 Guiselin, O. Irreversible adsorption of a concentrated polymer solution. *EPL (Europhysics Letters)* **17**, 225 (1992).

106 De Virgiliis, A., Milchev, A., Rostiashvili, V. & Vilgis, T. Structure and dynamics of a polymer melt at an attractive surface. *The European Physical Journal E: Soft Matter and Biological Physics* **35**, 1-11 (2012).

107 Scheutjens, J. & Fleer, G. Statistical theory of the adsorption of interacting chain molecules. 1. Partition function, segment density distribution, and adsorption isotherms. *Journal of Physical Chemistry* **83**, 1619-1635 (1979).

108 Krutyeva, M., Wischnewski, A., Monkenbusch, M., Willner, L., Maiz, J., Mijangos, C., Arbe, A., Colmenero, J., Radulescu, A. & Holderer, O. Effect of nanoconfinement on polymer dynamics: Surface layers and interphases. *Physical review letters* **110**, 108303 (2013).

109 Kim, S. Y., Meyer, H. W., Saalwächter, K. & Zukoski, C. F. Polymer dynamics in PEG-silica nanocomposites: Effects of polymer molecular weight, temperature and solvent dilution. *Macromolecules* **45**, 4225-4237 (2012).

110 Papon, A., Montes, H., Hanafi, M., Lequeux, F., Guy, L. & Saalwächter, K. Glass-transition temperature gradient in nanocomposites: evidence from nuclear

magnetic resonance and differential scanning calorimetry. *Physical review letters* **108**, 065702 (2012).

111 Crawford, M., Smalley, R., Cohen, G., Hogan, B., Wood, B., Kumar, S., Melnichenko, Y. B., He, L., Guise, W. & Hammouda, B. Chain Conformation in Polymer Nanocomposites with Uniformly Dispersed Nanoparticles. *Physical review letters* **110**, 196001 (2013).

112 Zhang, Q. & Archer, L. A. Poly (ethylene oxide)/silica nanocomposites: structure and rheology. *Langmuir* **18**, 10435-10442 (2002).

113 Mooney, M. The viscosity of a concentrated suspension of spherical particles. *Journal of colloid science* **6**, 162-170 (1951).

114 Moll, J. & Kumar, S. K. Glass Transitions in Highly Attractive Highly Filled Polymer Nanocomposites. *Macromolecules* **45**, 1131-1135 (2012).

115 Srivastava, S. & Basu, J. K. Experimental evidence for a new parameter to control the glass transition of confined polymers. *Physical Review Letters* **98** (2007).

116 Starr, F. W. & Douglas, J. F. Modifying Fragility and Collective Motion in Polymer Melts with Nanoparticles. *Physical review letters* **106**, 115702 (2011).

117 Adam, G. & Gibbs, J. H. On the temperature dependence of cooperative relaxation properties in glass‐forming liquids. *The journal of chemical physics* **43**, 139-146 (1965).

118 Park, S. J. & Larson, R. G. Tube dilation and reptation in binary blends of monodisperse linear polymers. *Macromolecules* **37**, 597-604 (2004).

119 Hu, Z. & Xia, X. Hydrogel nanoparticle dispersions with inverse thermoreversible gelation. *Advanced Materials* **16**, 305-309 (2004).

120 McKee, J. R., Hietala, S., Seitsonen, J., Laine, J., Kontturi, E. & Ikkala, O. Thermoresponsive Nanocellulose Hydrogels with Tunable Mechanical Properties. *ACS Macro Letters* **3**, 266-270 (2014).

121 Ding, F., Tang, Z., Ding, B., Xiong, Y., Cai, J., Deng, H., Du, Y. & Shi, X. Tunable thermosensitive behavior of multiple responsive chitin. *Journal of Materials Chemistry B* **2**, 3050-3056 (2014).

122 Chen, Y., Kushner, A. M., Williams, G. A. & Guan, Z. Multiphase design of autonomic self-healing thermoplastic elastomers. *Nature chemistry* **4**, 467-472 (2012).

123 Montarnal, D., Tournilhac, F., Hidalgo, M., Couturier, J.-L. & Leibler, L. Versatile one-pot synthesis of supramolecular plastics and self-healing rubbers. *Journal of the American Chemical Society* **131**, 7966-7967 (2009).

124 Chen, X., Wudl, F., Mal, A. K., Shen, H. & Nutt, S. R. New thermally remendable highly cross-linked polymeric materials. *Macromolecules* **36**, 1802-1807 (2003).

125 Zhang, Y., Broekhuis, A. A. & Picchioni, F. Thermally self-healing polymeric materials: the next step to recycling thermoset polymers? *Macromolecules* **42**, 1906-1912 (2009).

126 Lott, J. R., McAllister, J. W., Arvidson, S. A., Bates, F. S. & Lodge, T. P. Fibrillar Structure of Methylcellulose Hydrogels. *Biomacromolecules* **14**, 2484-2488 (2013).

127 Ramirez, A. L. B., Kean, Z. S., Orlicki, J. A., Champhekar, M., Elsakr, S. M., Krause, W. E. & Craig, S. L. Mechanochemical strengthening of a synthetic polymer in response to typically destructive shear forces. *Nature chemistry* **5**, 757-761 (2013).

128 Agrawal, A., Chipara, A. C., Shamoo, Y., Patra, P. K., Carey, B. J., Ajayan, P. M., Chapman, W. G. & Verduzco, R. Dynamic self-stiffening in liquid crystal elastomers. *Nature communications* **4**, 1739 (2013).

129 Bréchet, Y., Cavaille, J.-Y., Chabert, E., Chazeau, L., Dendievel, R., Flandin, L. & Gauthier, C. Polymer based nanocomposites: Effect of filler-filler and filler-matrix interactions. *Advanced engineering materials* **3**, 571 (2001).

130 Chevigny, C., Dalmas, F., Di Cola, E., Gigmes, D., Bertin, D., Boué, F. o. & Jestin, J. Polymer-grafted-nanoparticles nanocomposites: dispersion, grafted chain conformation, and rheological behavior. *Macromolecules* **44**, 122-133 (2010).

131 Akcora, P., Kumar, S. K., García Sakai, V., Li, Y., Benicewicz, B. C. & Schadler, L. S. Segmental dynamics in PMMA-grafted nanoparticle composites. *Macromolecules* **43**, 8275-8281 (2010).

132 Scheutjens, J. & Fleer, G. Statistical theory of the adsorption of interacting chain molecules. 2. Train, loop, and tail size distribution. *The Journal of Physical Chemistry* **84**, 178-190 (1980).

133 Haley, J. C. & Lodge, T. P. Dynamics of a poly (ethylene oxide) tracer in a poly (methyl methacrylate) matrix: Remarkable decoupling of local and global motions. *The Journal of chemical physics* **122**, 234914 (2005).

134 Tyagi, M., Arbe, A., Alegria, A., Colmenero, J. & Frick, B. Dynamic confinement effects in polymer blends. A quasielastic neutron scattering study of the slow component in the blend poly (vinyl acetate)/poly (ethylene oxide). *Macromolecules* **40**, 4568-4577 (2007).

135 Tyagi, M., Arbe, A., Colmenero, J., Frick, B. & Stewart, J. Dynamic confinement effects in polymer blends. A quasielastic neutron scattering study of the dynamics of poly (ethylene oxide) in a blend with poly (vinyl acetate). *Macromolecules* **39**, 3007-3018 (2006).

136 Lutz, T., He, Y., Ediger, M., Cao, H., Lin, G. & Jones, A. A. Rapid poly (ethylene oxide) segmental dynamics in blends with poly (methyl methacrylate). *Macromolecules* **36**, 1724-1730 (2003).

137 Niedzwiedz, K., Wischnewski, A., Monkenbusch, M., Richter, D., Genix, A.-C., Arbe, A., Colmenero, J., Strauch, M. & Straube, E. Polymer chain dynamics in a random environment: heterogeneous mobilities. *Physical review letters* **98**, 168301 (2007).

138 Kamath, S., Colby, R. H., Kumar, S. K., Karatasos, K., Floudas, G., Fytas, G. & Roovers, J. E. Segmental dynamics of miscible polymer blends: Comparison of the predictions of a concentration fluctuation model to experiment. *The Journal of chemical physics* **111**, 6121-6128 (1999).

139 Lodge, T. P. & McLeish, T. C. Self-concentrations and effective glass transition temperatures in polymer blends. *Macromolecules* **33**, 5278-5284 (2000).

140 Ngai, K. & Roland, C. Unusual component dynamics in poly (ethylene oxide)/poly (methyl methacrylate) blends as probed by deuterium NMR. *Macromolecules* **37**, 2817-2822 (2004).

141 Ito, H., Russell, T. & Wignall, G. Interactions in mixtures of poly (ethylene oxide) and poly (methyl methacrylate). *Macromolecules* **20**, 2213-2220 (1987).

142 Schwahn, D., Pipich, V. & Richter, D. Composition and Long-Range Density Fluctuations in PEO/PMMA Polymer Blends: A Result of Asymmetric Component Mobility. *Macromolecules* **45**, 2035-2049 (2012).

143 Pedemonte, E., Polleri, V., Turturro, A., Cimmino, S., Silvestre, C. & Martuscelli, E. Thermodynamics of poly (ethylene oxide)-poly (methyl methacrylate) blends: prediction of miscibility based on the corresponding-states theory. *Polymer* **35**, 3278-3281 (1994).

144 Fernandes, A., Barlow, J. & Paul, D. Blends containing polymers of epichlorohydrin and ethylene oxide. Part I: Polymethacrylates. *Journal of applied polymer science* **32**, 5481-5508 (1986).

145 Bhowmik, D., Pomposo, J., Juranyi, F., García Sakai, V., Zamponi, M., Arbe, A. & Colmenero, J. Investigation of a Nanocomposite of 75 wt% Poly (methyl methacrylate) Nanoparticles with 25 wt% Poly (ethylene oxide) Linear Chains: A Quasielatic Neutron Scattering, Calorimetric, and WAXS Study. *Macromolecules* (2014).

146 Bhowmik, D., Pomposo, J., Juranyi, F., García-Sakai, V., Zamponi, M., Su, Y., Arbe, A. & Colmenero, J. Microscopic Dynamics in Nanocomposites of Poly (ethylene oxide) and Poly (methyl methacrylate) Soft Nanoparticles: A Quasi-Elastic Neutron Scattering Study. *Macromolecules* (2013).

147 Colmenero, J. A Generalized Rouse Incoherent Scattering Function for Chain Dynamics of Unentangled Polymers in Dynamically Asymmetric Blends. *Macromolecules* **46**, 5363-5370 (2013).

148 Mukhopadhyay, R., Alegria, A., Colmenero, J. & Frick, B. Methyl group dynamics in poly (vinyl acetate): a neutron scattering study. *Macromolecules* **31**, 3985-3993 (1998).

149 Lorthioir, C., Alegría, A. & Colmenero, J. Out of equilibrium dynamics of poly (vinyl methyl ether) segments in miscible poly (styrene)-poly (vinyl methyl ether) blends. *Physical Review E* **68**, 031805 (2003).

150 Gotze, W. & Sjogren, L. Relaxation processes in supercooled liquids. *Reports on Progress in Physics* **55**, 241 (1992).

151 Genix, A.-C., Arbe, A., Alvarez, F., Colmenero, J., Willner, L. & Richter, D. Dynamics of poly (ethylene oxide) in a blend with poly (methyl methacrylate): A quasielastic neutron scattering and molecular dynamics simulations study. *Physical Review E* **72**, 031808 (2005).

152 Dionísio, M., Fernandes, A. C., Mano, J. F., Correia, N. T. & Sousa, R. C. Relaxation studies in PEO/PMMA blends. *Macromolecules* **33**, 1002-1011 (2000).

153 Schröter, K., Unger, R., Reissig, S., Garwe, F., Kahle, S., Beiner, M. & Donth, E. Dielectric spectroscopy in the αβ splitting region of glass transition in poly (ethyl methacrylate) and poly (n-butyl methacrylate): Different evaluation methods and experimental conditions. *Macromolecules* **31**, 8966-8972 (1998).

154 Smith, G. D., Bedrov, D. & Borodin, O. Structural relaxation and dynamic heterogeneity in a polymer melt at attractive surfaces. *Physical review letters* **90**, 226103 (2003).

155 Betancourt, B. A. P., Douglas, J. F. & Starr, F. W. Fragility and cooperative motion in a glass-forming polymer–nanoparticle composite. *Soft Matter* **9**, 241-254 (2013).

156 Cipelletti, L. & Ramos, L. Slow dynamics in glassy soft matter. *Journal of Physics: Condensed Matter* **17**, R253 (2005).

157 Fluerasu, A., Moussaïd, A., Madsen, A. & Schofield, A. Slow dynamics and aging in colloidal gels studied by x-ray photon correlation spectroscopy. *Physical Review E* **76**, 010401 (2007).

158 Del Gado, E., Fierro, A., de Arcangelis, L. & Coniglio, A. Slow dynamics in gelation phenomena: From chemical gels to colloidal glasses. *Physical Review E* **69**, 051103 (2004).

159 Fukao, K. & Miyamoto, Y. Slow dynamics near glass transitions in thin polymer films. *Physical Review E* **64**, 011803 (2001).

160 Bouchaud, J.-P. & Pitard, E. Anomalous dynamical light scattering in soft glassy gels. *The European Physical Journal E* **6**, 231-236 (2001).

161 Leheny, R. L. XPCS: Nanoscale motion and rheology. *Current Opinion in Colloid & Interface Science* **17**, 3-12 (2012).

162 Martinez, V., Thijssen, J., Zontone, F., van Megen, W. & Bryant, G. Dynamics of hard sphere suspensions using dynamic light scattering and X-ray photon correlation spectroscopy: Dynamics and scaling of the intermediate scattering function. *The Journal of chemical physics* **134**, 054505 (2011).

163 Ramos, L. & Cipelletti, L. Ultraslow dynamics and stress relaxation in the aging of a soft glassy system. *Physical review letters* **87**, 245503 (2001).

164 Narayanan, S., Lee, D. R., Hagman, A., Li, X. & Wang, J. Particle dynamics in polymer-metal nanocomposite thin films on nanometer-length scales. *Physical review letters* **98**, 185506 (2007).

165 Narayanan, R. A., Thiyagarajan, P., Lewis, S., Bansal, A., Schadler, L. & Lurio, L. Dynamics and internal stress at the nanoscale related to unique thermomechanical behavior in polymer nanocomposites. *Physical review letters* **97**, 075505 (2006).

166 Frieberg, B., Kim, J., Narayanan, S. & Green, P. F. Surface layer dynamics in miscible polymer blends. *ACS Macro Letters* **2**, 388-392 (2013).

167 Akcora, P., Kumar, S. K., Moll, J., Lewis, S., Schadler, L. S., Li, Y., Benicewicz, B. C., Sandy, A., Narayanan, S. & Ilavsky, J. “Gel-like” mechanical

reinforcement in polymer nanocomposite melts. *Macromolecules* **43**, 1003-1010 (2009).

168 Ranka, M., Varkey, N., Ramakrishnan, S. & Zukoski, C. F. Impact of small changes in particle surface chemistry for unentangled polymer nanocomposites. *Soft matter* (2015).

169 Guo, H., Bourret, G., Corbierre, M. K., Rucareanu, S., Lennox, R. B., Laaziri, K., Piche, L., Sutton, M., Harden, J. L. & Leheny, R. L. Nanoparticle motion within glassy polymer melts. *Physical review letters* **102**, 075702 (2009).

170 Sikorski, M., Jiang, Z., Sprung, M., Narayanan, S., Sandy, A. & Tieman, B. A graphical user interface for real-time analysis of XPCS using HPC. *Nuclear Instruments and Methods in Physics Research Section A: Accelerators, Spectrometers, Detectors and Associated Equipment* **649**, 234-236 (2011).

171 Frieberg, B., Kim, J., Narayanan, S. & Green, P. F. Surface Dynamics of Miscible Polymer Blend Nanocomposites. *ACS nano* **8**, 607-613 (2014).

172 Rubinstein, M. & Colby, R. C. Polymer Physics. *Oxford University Press* (2003).

173 Giacomin, A. J., Gilbert, P. H., Merger, D. & Wilhelm, M. Large-amplitude oscillatory shear: comparing parallel-disk with cone-plate flow. *Rheologica Acta*, 1-23 (2014).

174 Bharadwaj, N. A. & Ewoldt, R. H. Single-point parallel disk correction for asymptotically nonlinear oscillatory shear. *Rheologica Acta*, 1-11 (2015).

175 Ewoldt, R., Winter, P., Maxey, J. & McKinley, G. Large amplitude oscillatory shear of pseudoplastic and elastoviscoplastic materials. *Rheologica Acta* **49**, 191-212, doi:10.1007/s00397-009-0403-7 (2010).

176 Cimmino, S., Martuscelli, E. & Silvestre, C. Miscibility prediction based on the corresponding states theory: poly (ethylene oxide)/atactic poly (methyl methacrylate) system. *Polymer* **30**, 393-398 (1989).

177 Schantz, S. & Veeman, W. Nanoheterogeneity in PEO/PMMA blends probed by 129Xe - NMR. *Journal of Polymer Science Part B: Polymer Physics* **35**, 2681-2688 (1997).

178 Wästlund, C. & Maurer, F. H. Positron lifetime distributions and free volume parameters of PEO/PMMA blends determined with the maximum entropy method. *Macromolecules* **30**, 5870-5876 (1997).

179 Hopkinson, I., Kiff, F., Richards, R., King, S. & Farren, T. Isotopic labelling and composition dependence of interaction parameters in polyethylene oxide/polymethyl methacrylate blends. *Polymer* **36**, 3523-3531 (1995).

180 Gaikwad, A. N., Wood, E. R., Ngai, T. & Lodge, T. P. Two calorimetric glass transitions in miscible blends containing poly (ethylene oxide). *Macromolecules* **41**, 2502-2508 (2008).

181 Lodge, T. P., Wood, E. R. & Haley, J. C. Two calorimetric glass transitions do not necessarily indicate immiscibility: the case of PEO/PMMA. *Journal of Polymer Science Part B: Polymer Physics* **44**, 756-763 (2006).

182 Leroy, E., Alegría, A. & Colmenero, J. Quantitative study of chain connectivity inducing effective glass transition temperatures in miscible polymer blends. *Macromolecules* **35**, 5587-5590 (2002).

183 Sakaguchi, T., Taniguchi, N., Urakawa, O. & Adachi, K. Calorimetric study of dynamical heterogeneity in blends of polyisoprene and poly (vinylethylene). *Macromolecules* **38**, 422-428 (2005).

184 Savin, D. A., Larson, A. M. & Lodge, T. P. Effect of composition on the width of the calorimetric glass transition in polymer–solvent and solvent–solvent mixtures. *Journal of Polymer Science Part B: Polymer Physics* **42**, 1155-1163 (2004).

185 Wu, S. Entanglement, friction, and free volume between dissimilar chains in compatible polymer blends. *Journal of Polymer Science Part B: Polymer Physics* **25**, 2511-2529 (1987).

186 Colby, R. H. Breakdown of time-temperature superposition in miscible polymer blends. *Polymer* **30**, 1275-1278 (1989).

187 Zawada, J. A., Ylitalo, C. M., Fuller, G. G., Colby, R. H. & Long, T. E. Component relaxation dynamics in a miscible polymer blend: poly (ethylene oxide)/poly (methyl methacrylate). *Macromolecules* **25**, 2896-2902 (1992).

188 Lartigue, C., Guillermo, A. & Cohen–Addad, J. Proton NMR investigation of the local dynamics of PEO in PEO/PMMA blends. *Journal of Polymer Science Part B: Polymer Physics* **35**, 1095-1105 (1997).

189 Shenogin, S., Kant, R., Colby, R. H. & Kumar, S. K. Dynamics of miscible polymer blends: predicting the dielectric response. *Macromolecules* **40**, 5767-5775 (2007).

190 Jin, X., Zhang, S. & Runt, J. Broadband dielectric investigation of amorphous poly (methyl methacrylate)/poly (ethylene oxide) blends. *Macromolecules* **37**, 8110-8115 (2004).

191 Sacristan, J., Chen, C. & Maranas, J. K. Role of Effective Composition on Dynamics of PEO− PMMA Blends. *Macromolecules* **41**, 5466-5476 (2008).

192 García Sakai, V., Maranas, J. K., Peral, I. & Copley, J. R. Dynamics of PEO in blends with PMMA: Study of the effects of blend composition via quasi-elastic neutron scattering. *Macromolecules* **41**, 3701-3710 (2008).

193 Zeroni, I., Ozair, S. & Lodge, T. P. Component terminal dynamics in poly (ethylene oxide)/poly (methyl methacrylate) blends. *Macromolecules* **41**, 5033-5041 (2008).

194 Sy, J. W. & Mijovic, J. Reorientational dynamics of poly (vinylidene fluoride)/poly (methyl methacrylate) blends by broad-band dielectric relaxation spectroscopy. *Macromolecules* **33**, 933-946 (2000).

195 Moreno, A. J. & Colmenero, J. Is there a higher-order mode coupling transition in polymer blends? *The Journal of chemical physics* **124**, 184906 (2006).

196 Moreno, A. J. & Colmenero, J. Entangledlike chain dynamics in nonentangled polymer blends with large dynamic asymmetry. *Physical review letters* **100**, 126001 (2008).

197 Bhowmik, D., Pomposo, J., Juranyi, F., García-Sakai, V., Zamponi, M., Su, Y., Arbe, A. & Colmenero, J. Microscopic Dynamics in Nanocomposites of Poly (ethylene oxide) and Poly (methyl methacrylate) Soft Nanoparticles: A Quasi-Elastic Neutron Scattering Study. *Macromolecules* **47**, 304-315 (2013).

198 Guillermo, A., Lartigue, C. & Cohen Addad, J. PEO temporary network in PEO/PMMA blends: NMR approach. *Macromolecules* **31**, 769-775 (1998).

VITA

ERKAN SENSES

PERSONAL INFORMATION

Date of Birth: November 19, 1984

Place of Birth: Kocaeli, Turkey

EDUCATION

PhD in Materials Engineering (05/2015)

Stevens Institute of technology, Hoboken, NJ, USA

Thesis title: Interphase and Partcile Dispersion Correlations in Polymer Nanocomposites

MS in Materials Science and Engineering (06/2009)

Stanford University, Stanford, CA, USA

Thesis title: Nanometer size effect on hydrogen storage properties of thin film metal hydride

BS in Mechanical Engineering (06/2007)

Bogazici University, Istanbul, Turkey

RESEARCH EXPERIENCE

Research Assistant, Stevens Institute of Technology

Prof. Pinar Akcora's Soft Materials Laboratory: Research aims to understand, at the fundamental level, the relationship between interphase and bulk properties in polymer nanocomposites; and explore novel strategies to develop adaptive mechanical behavior of soft materials to large (nonlinear) deformation and high temperature environments.

- Fabricated polymer-inorganic nanohybrids with controlled nanoparticle dispersion.
- Extensive 2D and 3D structural and morphological characterization via TEM, SEM and SAXS.
- Dynamics of polymers and nanoparticles studied via rheometry, XPCS and DLS.
- Extensive use of rheological and analytical tools to characterize bulk mechanical response of nanocomposite polymers and gels at medium and large deformation regimes.
- Developed an interfacial self-strengthening mechanism of polymers in response to large shear.
- Discovered a novel strategy to for designing temperature adaptive nanocomposites.
- Demonstrated an evaporation-driven, polymer-mediated and template-free strategy for colloidal particles to self-pattern on solid surfaces.

Research Assistant at Stanford University

Prof. Bruce M. Clemens' Lab: Thesis title: Nanometer size effects on hydrogen storage properties in thin-film metal hydrides.

- Studied Mg-MgH_2 system as a model hydrogen storage medium via interfacial reactions in their thin films.
- Physical vapor deposition of thin films, sample preparation and structural characterization via XRD analysis.

- Adsorption-desorption kinetics studied using Quartz Crystal Microbalance (QCM) system.

TEACHING EXPERIENCE

Stevens Institute of Technology

Teaching assistant (08/13-12/14): Interdisciplinary Thermodynamics and graduate level Thermodynamics in Materials Science courses. Responsibilities include conducting weekly recitations and office hours, preparation of weekly quizzes in addition to exam and homework grading.

Undergraduate student mentor: 2+ year experience on mentoring undergraduate students in research laboratory. The role involved training students with analytical and synthetic techniques to achieve their project goals. Research conducted with undergraduate students published in a peer reviewed journal.

SKILLS

Research:

Sample preparation**:** PVD of metal thin films, spin coating of polymers, solution casting of nanocomposites with controlled nanoparticle dispersion, Free-radical polymerization.

Characterization techniques**:**

-Mechanical (*ARES-G2 Rheometer, Instron DMA*)

-Electron microscopy (*TEM, SEM*), Confocal Florescent Microscope

-X-rays (*XRD, SAXS user at Brookhaven National Lab; XPCS User at Argonne National Lab*)

-Neutrons (*SANS user at Oak Ridge National Lab, Spin-echo user at NIST*)

-Static/Dynamic Light Scattering (*DLS*), FTIR

-Thermal (*TGA, DSC*)

-Gel Permeation Chromatography (*GPC*)

Computer: *Languages*: C, C#.NET *Software packages*: MATLAB, IGOR, LabView, Catia, SolidWorks.

Leadership: Founding President of Stevens Materials Research Society (Official University Chapter of MRS).

ACHIEVEMENTS, AWARDS and DEGREES

Outreach Program Award for the NIST-NCNR, *University of Maryland* 10/14

Graduate Student Conference Funds, *Stevens Inst. Of Tech.* 03/13-03/14

Materials Research Society Travel Award, *MRS* 10/12

FULBRIGHT Scholarship, *US Department of State* 09/07-06/09

Graduate Student Scholarship, *TEV* 09/07-06/09

Rice and Cullimore Fellowship. *ASME* 10/07-06/08

High Honor Graduation Certificate, *Bogazici Uni.* 06/07

1st Prize in Hidromobi'07, *National Sci. Foundation of Turkey-TUBITAK* 08/07

8th (1st national) in European Shell Eco-Marathon Race, *Toulouse, France* 05/07

National winner in CEFIC (Europ. Chem. Industry Council) Project, *Finland* 05/02

MEMBERSHIPS

Materials Research Society, American Physical Society, Society of Rheology, Society of Plastics Engineers

PUBLICATIONS

- E. Senses, A. Isherwood, P. Akcora, "*Reversible thermal-stiffening in polymer nanocomposites*", submitted to ACS Applied Materials and Interfaces, 2015

- E. Senses, P. Akcora, "*Tuning mechanical properties of nanocomposites with bimodal polymer bound layers*", RSC Advances, 4(91), 2014.

- E. Senses, Y. Jiao, P. Akcora, "*Modulating interfacial attractions of polymer-grafted nanoparticles in melts under shear"*, Soft Matter, 10(25), 4464, 2014.

- E. Senses, P. Akcora, *"Mechanistic model for deformation of polymer nanocomposite melts under large amplitude shear"*, J. Polymer Science Part B: Polymer Physics, 51(9), 764, 2013.

- E. Senses, P. Akcora, *"An interface driven stiffening in polymer nanocomposites"*, Macromolecules, 46(5), 1868, 2013.

- E. Senses, M. Black, T. Cunnignham, S. A. Sukhishvili, P. Akcora, *"Spatial ordering of colloids in a drying aqueous polymer droplet"*, Langmuir, 29(8), 2588, 2013.

- Z. Zhu, E. Senses, P. Akcora, S. A. Sukhishvili, *"Programmable light-controlled shape changes in layered polymer nanocomposites"*, ACS Nano, 6(4), 3152, 2012.

PRESENTATIONS

- E. Senses, P. Akcora, *"Reversible thermal-stiffening in polymer nanocomposites",* American Physical Society March Meeting, 2015.

- E. Senses, P. Akcora, *"Effect of interfacial entanglement density on the melt and glassy properties of attractive polymer nanocomposites",*American Physical Society, March Meeting, 2014.

- Y. Jiao, E. Senses, P. Akcora, *"Mechanical behavior of polymer-grafted iron oxide nanoparticles under large shear deformation",*American Physical Society, March Meeting, 2014.

- E. Senses, P. Akcora, *"Physical origin of non-linearities in homopolymers and polymer nanocomposites",* Society of Rhelogy Annual Meeting, 2013.

- E. Senses, P. Akcora, *"An interface controlled dynamic stiffening in polymer nanocomposites",* American Physical Society, March Meeting, 2013.

- E. Senses, P. Akcora, *"Evaporation induced ordering in polymer-colloid suspensions",* American Physical Society, March Meeting, 2013.

- S. A. Sukhishvili, Z. Zhu, E. Senses, P. Akcora, *"Layered, light-responsive polymer nanocomposites."* American Chemical Society, National Meeting, 2013.

- E. Senses, P. Akcora, *"Mechanical Properties of Polymer Nanocomposites under Large Amplitude Deformation",* American Physical Society, March Meeting, 2013.

- E. Senses, P. Akcora, *"Shear induced strengthening in polymer nanocomposites",* Materials Research Society, Fall Meeting, 2012.

- E. Senses, P. Akcora, *"Structure-property relationships in polymer nanocomposites at large amplitude deformation" (Poster Display),* New York Academy of Sciences, Gotham-Metro Cond. Matter Meeting, 2011.

- C. J. Chung, S. T. Kelly, E. Senses, B. M. Clemens, *'Elastic strain energy, thermodynamics, and kinetics of hydride formation in Mg-based thin films'*, American Chemical Society, National Meeting, 2010.

- E. Senses, S. T. Kelly and B. M. Clemens, *'Quantitative Quartz Crystal Microbalance Studies of Equilibrium Pressures in Thin Film Metal Hydrides' (Poster Display)*, Materials Research Society, Spring Meeting, 2009.

- S. T. Kelly, E. Senses and B. M. Clemens, *'Using Multilayer Thin Films to Quantitatively Characterize Interfacial Reactions in Metal Hydride Material Systems at Sub-nanometer Length Scales',* Materials Research Society, Spring Meeting, 2009